High Charge-to-Spin and Spin-to-Charge Conversion Enhanced by Quantum Confinement Effect in Sputtered Topological Insulator Thin Films

A DISSERTATION

SUBMITTED TO THE FACULTY OF

UNIVERSITY OF MINNESOTA

BY

Mahendra DC

IN PARTIAL FULFILLMENT OF THE REQUIREMENTS

FOR THE DEGREE OF

Doctor of Philosophy

Advised by Jian-Ping Wang

January 2019

© Mahendra DC 2019.

All rights Reserved.

Acknowledgements

I would like to thank my advisor Prof. Jian-Ping Wang who patiently supported and guided me for the past six years. I learned how to become an outstanding researcher and great person from him. Countless insightful discussions with him leading to solving problems, encouragement, and inspiration that I received from Prof. Wang are invaluable for me.

I would like to thank my fellow groupmates; without your support it would not have been possible for me to learn experimental techniques. I would like to thank Zhengyang Zhao and Dr. Angeline K. Smith who taught me device fabrication. I would also like to thank Hongshi Li and Zhengyang Zhao for helping me to do the electrical measurements. I also really appreciate the help that I received from Prof. Wang group members especially Dr. Patrick Quarterman, Dr. Yang Lv, Dr. Yinglong Feng, Thomas Peterson, and Protyush Sahu.

I would like to thank postdoctoral associates of Prof. Wang's group Dr. Mahdi Jamali, Dr. Junyang Chen and Dr. Delin Zhang for mentoring me and preparing numerous samples for my projects.

Some portion of my thesis was accomplished in collaboration with Prof. Andre Mkhoyan and Prof. Tony Low's groups at the University of Minnesota and Prof. Mingzhong Wu's group at Colorado State University. The wonderful cross-section TEM images carried out by Dr. Danielle R. Hickey from Prof. Andre Mkhoyan's group helped us to understand unexpected results in sputtered bismuth selenide thin films. I would like to thank Dr. Roberto Grassi and Prof. Low for performing quantum transport numerical simulations. I would also like to thank Prof. Aurelien Manchon at King Saud University in Saudi Arabia who helped us in understanding results of the quantum transport numerical simulation results. I am grateful to Prof. Mingzhong Wu and Dr. Tao Liu for providing us the YIG films.

I would like to thank Timothy Peterson, Zheng Jiang and Gordon Steicklein from Prof. Paul Crowell's group on preparing physical property measurement system for my measurements.

The support from my classmates (too many to name here) was vital during my time in graduate school. Camping trips, intramural events, and happy hours with you all made my graduate school life more enjoyable. In addition, Coffee and happy hours with Dr. Prabesh Dulal and Dr. Mandip Shibakoti was a lot of fun.

I also thank financial support from the C-SPIN center of STARnet program (www.cspin.umn) and ASCENT center from JUMP program. My experience with C-SPIN PIs, students, and industry leaders from C-SPIN sponsors was wonderful and special.

Finally, I would like to thank my parents and all other family members for their continuous love and support. Without their unconditional love and support, I would not have been able to complete my study.

Dedication

To my parents, family members, and all the gurus.

Abstract

The spin-orbit torque (SOT) arising from materials with large spin-orbit coupling promises a path for ultra-low power and fast magnetic-based storage and computational devices. The SOT switching of magnetization can be used in the SOT-memory and computational devices whereas the spin-to-charge conversion can be utilized for reading of magnetization state in computational devices. Recent reports on topological insulators show high SOT but the industry compatible growth process is still lacking. Furthermore, SOT switching of perpendicular magnetization from topological insulators is demonstrated but still with large current density and large external field. We investigated the SOT from magnetron-sputtered bismuth selenide thin films in $Bi_xSe_{(1-x)}/Co_{20}Fe_{60}B_{20}$ heterostructures by using dc planar Hall and spin-torque ferromagnetic resonance (ST-FMR) methods. Remarkably, the spin torque efficiency (θ_S) was determined to be as large as 18.62 ± 0.13 and 8.67 ± 1.08, using the dc planar Hall and ST-FMR methods, respectively. Moreover, switching of perpendicular CoFeB multilayers using SOT from the $Bi_xSe_{(1-x)}$ has been observed at room temperature (RT) with low critical magnetization switching current density (J_{sw}) 4.3×10^5 A/cm^2. Quantum transport simulations using realistic sp^3 tight binding model suggests that the high SOT in sputtered $Bi_xSe_{(1-x)}$ is due to a quantum confinement effect, whose charge-to-spin conversion efficiency enhances with reduced size and dimensionality. The demonstrated θ_S , ease of growth of the films on a silicon substrate, and successful growth and switching of perpendicular CoFeB multilayers on $Bi_xSe_{(1-x)}$ film provide an avenue for the use of bismuth selenide thin films as a spin-density generator in SOT-based memory and logic devices.

In addition to charge-to-spin conversion, we also performed spin-to-charge conversion by sputtered bismuth selenide thin films. For the spin-to-charge conversion experiment, we prepared $Sub/Si/SiO_2/Bi_{43}Se_{57}/Co_{20}Fe_{60}B_{20}$ heterostructures with in-plane magnetization. High spin-to-charge conversion voltage signals have been observed at room temperature. The spin-pumping voltage decreases with an increase in the size of the grains. The figure-of-merit of spin-to-charge

conversion inverse Edelstein effect length (λ_{IEE}) is estimated to be as large as 0.32 nm. The large λ_{IEE} is due to the spin-momentum locking and is further enhanced by quantum confinement in the nano sized grains of the sputtered bismuth selenide films. We also investigated the effect on spin-pumping voltage due to the insertion of layers MgO and Ag. The MgO insertion layer has almost completely suppressed the spin-pumping voltage whereas Ag insertion layer has enhanced the spin-pumping voltage as large as 40%. The suppression of spin-pumping voltage due to the insertion of insulating layer indicates that the thermal effects are negligible in the spin-pumping signal. The enhancement of spin-to-charge conversion voltage by insertion Ag layer is due to the Rashba-Edelstein effect.

Moreover, the conducting ferromagnetic layer can influence both SOT and spin-to-charge conversion voltage. We investigated spin-to-charge conversion in sputtered $Y_3Fe_5O_{12}$(YIG)/BS bi-layers at room temperature. The spin current is pumped to the BS layer by the precession of magnetization at ferromagnetic resonance in the YIG layer. λ_{IEE} is estimated to be as large as (0.11 ± 0.03) nm in YIG/BS (4 nm). Moreover, λ_{IEE} also shows a dependence on the bismuth selenide film thickness in YIG/BS structure, which is consistent with the spin-to-charge conversion in conducting ferromagnet and also in case of charge-to-spin conversion.

Contents

Acknowledgements i

Dedication iii

Abstract iv

Contents vi

List of Tables ix

Table of Figures x

Index Table xv

Chapter 1. Introduction 1

1.1 Motivation 1

1.2 Introduction to the fundamental spintronic device 2

1.3 Spin-current generation via the spin Hall effect 4

1.4 Non-equilibrium spin-accumulation via spin-orbit interaction originated from broken symmetry 5

1.5 Non-equilibrium spin-accumulation via spin-momentum locking in topological insulators 7

1.6 Torques on the ferromagnet via spin-accumulation generated by spin-orbit coupling 9

1.7 Spin-orbit torque switching of magnetization 13

1.8 Spin-to-charge conversion via spin-orbit coupling 15

Chapter 2. Experimental methods 20

2.1 Thin film growth and characterization techniques 20

2.1.1 Sputtering 20

2.1.2 Atomic force microscopy (AFM) 21

2.2 Transmission electron microscopy (TEM) 22

2.2.1 X-ray photo-electron spectroscopy (XPS) 23

2.2.2 Raman spectroscopy 23

2.3 Device fabrication 24

2.3.1 Optical lithography 24

2.3.2 Ion mill 24

2.3.3 CHA e-beam evaporator 24

2.4 Process flow for fabrication of Hall bar and ST-FMR devices 25

2.5 Process flow for spin-pumping device fabrication 26

2.6 SOT measurement set up for different types of measurement techniques 27
2.6.1 DC planar Hall measurement set up 27
2.6.2 Second harmonic Hall measurement set up 28
2.6.3 ST-FMR measurement set up 29
2.6.4 Spin-pumping measurement setup 30
Chapter 3. Room temperature high spin-orbit torque due to quantum confinement in sputtered $Bi_xSe_{(1-x)}$ films 31
3.1 Growth and characterization of bismuth selenide thin films 31
3.2 SOT characterization using dc planar Hall 36
3.3 Estimation of J_{BS} 42
3.4 SOT characterization of reference sample Ta by dc planar Hall 42
3.5 Spin-torque characterization using ferromagnetic resonance (ST-FMR) 44
3.6 Estimation of spin-pumping contribution to the symmetric voltage 48
3.7 Current induced perpendicular CoFeB multilayer switching 49
3.8 Effect of thin Ta insertion layer on SOT from BS in switching sample 54
Chapter 4. Enhancement of the spin-accumulation due to quantum confinement 58
4.1 Introduction 58
4.2 Discussion and results 60
Chapter 5. Spin-to-charge conversion by sputtered bismuth selenide thin films at room temperature 66
5.1 Introduction 66
5.2 Raman, XPS, and TEM characterization 67
5.3 Spin-pumping into BS from CoFeB 69
5.4 Spin-pumping on a control CoFeB sample 76
5.5 Spin-pumping on a reference Pt sample 77
5.6 Effect on spin-to-charge conversion due to insertion layers 78
5.7 Discussion 80
Chapter 6. Spin-to-charge conversion by sputtered bismuth selenide thin films via spin pumping from yttrium iron garnet 82
6.1 Introduction 82
6.2 Film preparation and device fabrication 82
6.3 Spin-pumping from YIG to BS 83
6.4 Absence of proximity-induced magnetism in YIG/BS 90
6.5 Discussion 91
Chapter 7. Conclusions and outlook 94

References..97
Appendix: VITA 111

List of Tables

Table 1 A summary of the θ_S , σ_S , J_{sw}, σ_c , and switching power dissipation of the TIs and HMs in this work and the best previous reports at room temperature. Note that the switching current density is the current density only through the NM layer. 53

Table of Figures

Figure 1.2.1 (a) Shows schematic stack structure of GMR spin-valve with Cu as spacer and (b) Shows MTJ spin-valve stack structure with tunnel barrier MgO. The blue arrows indicate magnetization direction. 3

Figure 1.3.1 Shows a schematic diagram of the spin Hall effect in Pt. The electrons with opposite spin directions are deflected in opposite direction due to the spin-orbit field. The spheres represent the electron and the arrows in the spheres represent spin-magnetic moment. 5

Figure 1.4.1 (a) Schematic diagram showing the Rashba SOC split spin-polarized bands at the Fermi level, electron spin is represented by red and blue arrows. (b) The electric field applied along the x-axis in the Rashba potential shifts the spin-polarized Fermi contours resulting in a non-equilibrium spin accumulation along the y-direction. Reprinted from Ref. [33] with permission from the American Physical Society. 7

Figure 1.5.1 (a) Band structure of Bi_2Se_3 obtained by angle resolved photoemission spectroscopy (ARPES). (b) Band structure calculation of Bi_2Se_3 where shaded regions are projection of bulk bands. Reprinted from Ref. [38] with permission from the Nature Publishing Group. 8

Figure 1.6.1 (a) Shows the representation of the various torques on a FM. SOTs change direction if direction of current flow or magnetization is changed (b) Shows a typical stack structure for the characterization of SOT. In this case, the spin source is a HM, which generates spin-current along the vertical direction via the spin Hall effect. For in-plane magnetization the ADLT is along the in-plane direction whereas the FLT is along the out-of-plane direction. 10

Figure 1.7.1 At the top panel: (a), (b), and (c) Schematic diagrams showing the magnetization direction along the z, y, and x, respectively. The charge current is converted into the spin-density via the spin Hall effect from Ta. At the bottom panel of (a), (b), and (c) magnetization dynamics simulations using the macro-spin model due to SOT is provided. Reprinted from Ref. [74] with permission from the Nature Publishing Group. 14

Figure 1.8.1 Schematic diagram of spin-pumping. RF field precesses the magnetization of the FM at an excitation frequency in the GHz range. In order to meet the FMR condition, H_{ext} is swept along the y-axis. At FMR, the FM pumps spins into the spin sink in the vertical direction. The spins injected into the spin sink get converted into a measurable open circuit voltage due to a mixture of ISHE, IEE, and IREE effects. 16

Figure 1.8.2 (a) Schematic diagram the showing spin-polarized band structure of a TI at the Fermi level (b) Spin-pumping into TI surface states shift the Fermi contour, which results in more electrons on one side of the Fermi contour than on another side. Reprinted from Ref. [9] with permission from Nature Publishing Group. 18

Figure 2.1.1 (a) Schematic diagram showing dc magnetron sputtering technique adapted from Ref. [105]. (b) A photograph of Shamrock sputtering system in Prof. Jian-Ping Wang's lab. 21

Figure 2.1.2 Schematic diagram of AFM adapted from Ref. [106] doi:10.1016/j.trac.2016.03.014. 22

Figure 2.6.1 Schematic block diagram of showing dc planar Hall measurement for the characterization of SOT. 27

Figure 2.6.2 Shows schematic block-diagram of the SHH measurement set up. 28

Figure 2.6.3 Schematic block diagram of ST-FMR measurement and optical image of the ST-FMR device. G and S stands for ground and signal, respectively. 29

Figure 2.6.4 Spin-pumping measurement setup block diagram and optical image of the spin-pumping device. G and S stands for ground and signal, respectively. 30

Figure 3.1.1 The electrical conductivity, Hall measurement, temperature dependent σ of bismuth selenide films. (a) The thickness-dependent electrical σ_c of the BS films. (b) The Hall measurement of 4, 16, and 40 nm BS films at room temperature to determine carrier concentration. (c) Temperature dependent σ_c of 16 and 40 nm BS films. 32

Figure 3.1.2 STEM characterization. (a) and (b) Composites of simultaneously acquired BF- and HAADF-STEM images of samples BS4 and BS8, respectively. The selected region of the HAADF-STEM image indicated by a black line is magnified at right to show the BS atomic detail. 33

Figure 3.1.3 EDX maps and Bi:Se composition line scans for samples BS4 and BS8. (a) HAADF-STEM image and individual-element EDX maps for sample BS8 (Ta+Si map indicates the combined Ta and Si signal due to peak overlap). EDX maps in (a) are normalized for visibility. (b) and (c) EDX composite maps for samples BS4 and BS8, respectively, scaled for atomic percent of each element. Arrows represent direction of composition line scans plotted in (d) and (e). (d) and (e) EDX line scan data for Bi:Se composition for samples BS4 and BS8, respectively (line scan data corresponds to white arrows in (b) and (c)). The line scans show that at the top surface of the BS layer, the stoichiometric ratio is Bi_2Se_3, but that the layers become Bi rich below the top surface, with the Bi concentration peaking several nm into the layer and then decreasing toward the layer's bottom edge (consistent for both the BS4 and BS8 samples). 34

Figure 3.1.4 The AFM images of the (a) 4 nm BS film and (b) BS4 sample, respectively. 35

Figure 3.2.1 Schematic diagram, experimental set up, angle-dependent Hall resistance measurements, and characterization of SOT. (a) A three-dimensional schematic diagram demonstrating the SOT in a BS/CoFeB heterostructure. H_{ext} and M represent an in-plane externally applied magnetic field and the in-plane magnetization, respectively. H_T and H_{OOP} are the current-induced transverse and out-of-plane magnetic fields, respectively. The red arrows represent the direction of spin-magnetic moment. (b) An optical micrograph of the fabricated Hall-cross bar with schematic drawings of the Hall measurement set up. (c) The $R_H(I,\alpha)$ of sample BS4 at ± 8.5 mA input current on the left axis and $R_{DH}(I,\alpha)$ on the right axis at RT under a constant 5000 Oe in-plane magnetic field. (d) The $R_{DH}(I,\alpha)$ at different input currents for the BS4 sample. (e) The variation of H_{OOP} with the current density. (f) The variation of H_{OOP} (left axis) and H_T (right axis) as a function of BS thickness. 37

Figure 3.2.2 Estimation of $\frac{dR_{AHE}}{dH}$ of sample BS4 (a) R_{AHE} as a function of rotation angle (γ) in the xz plane. (b) R_{AHE} as a function of external field when the magnetization is close to in-plane. 40

Figure 3.2.3 The characterization of FLT in sample BS4 (a) R_H and R_{DH} as a function of the field angle under a 200 Oe in-plane field. (b) The H_T is plotted against current density. 41

Figure 3.4.1 The angle-dependent Hall measurement for SOT characterization from the control sample. (a) The angle-dependent Hall resistance of the Ta sample at an input current of ± 8.5 mA on the left axis and difference in the Hall resistance on the right axis at room temperature under a

constant 5000 Oe in-plane magnetic field. (b) The angle-dependent difference in the Hall resistances at different bias currents for sample Ta. (c) The current-induced out-of-plane field as a function of the input current density for Ta sample. 43

Figure 3.5.1 ST-FMR measurement for the characterization of SOT (a) Schematic diagram showing the stack structure and co-ordinate system. (b), (e), and (f) ST-FMR resonance line shape of samples BS 4 and 16 nm, and Ta, respectively. The red and green solid lines are the symmetric and anti-symmetric components separated from the mixing voltage using Lorentzians. (c) The θ_S variation with excitation frequency of sample BS (4 nm). The error bars are from the uncertainties in the S and A values. (d) The plot of frequency versus resonance field of sample BS (4 nm); the red line is fit to Kittel's formula. Inset: linewidth versus frequency of sample BS (4 nm). 47

Figure 3.7.1 (a) The VSM measurement of the BS switching sample shows that the easy axis is in the out-of-plane direction and the anisotropy field is approximately 6000 Oe. (b) Schematic diagram of BS switching sample. 50

Figure 3.7.2 Current-induced magnetization switching in the BS (4 nm)/Ta (0.5 nm)/CoFeB(0.6 nm)/Gd (1.2 nm)/CoFeB (1.1 nm) heterostructure. (a) A schematic drawing of the switching sample stack structure. (b) The R_{AHE} measured in the BS switching sample using a current of 50 μA. (c) and (d) Current-induced switching of the magnetization due to the SOT arising from the BS underlayer in the presence of a constant 80 Oe in-plane bias field. The Hall-cross bar with dimensions of 15 μm × 70 μm is used for the switching experiment. 51

Figure 3.7.3 Current-induced magnetization switching in the Ta (5 nm)/CoFeB (0.6 nm)/Gd (1.2 nm)/CoFeB (1.1 nm) heterostructure. (a) Schematic drawing of the stack structure with thicknesses in nm and SOT where numbers represent thickness of the layers in nm. (b) The anomalous Hall resistance measured in the Ta switching sample using a 50 μA current. (c) and (d) Current-induced switching of the magnetization due to the SOT arising from the Ta underlayer in the presence of a constant 80 Oe in-plane bias field, measured using a Hall-cross bar with dimensions of 15 μm × 70 μm. 52

Figure 3.8.1 Characterization of SOT in BS (4 nm)/Ta (0.5 nm) layer. (a) The first and second harmonic resistances as a function of the field angle. The red solid line is fit to Eqn. *(3.8.1)*. (b) The current induced effective fields as a function of input bias current density. (c) The ST-FMR resonance line shape of the BS(4 nm)/Ta (0.5 nm)/CoFeB (5nm) sample at an excitation frequency of 7 GHz. Inset: θ_S is plotted against excitation frequency. 56

Figure 3.8.2 Characterization of SOT in Ta (5 nm)/CoFeB (0.6 nm)/Gd (1.2 nm)/CoFeB (0.6 nm). (a) The first and second harmonic resistances as a function of the field angle. The red solid line is fit to Eqn. *(3.8.1)* (b) The current induced effective fields as a function of input bias current density. 57

Figure 4.2.1 Effect of quantum confinement on spin accumulation. (a) Band structure of a slab (grey shaded region) and a square wire (lines) with a thickness of 4QLs. The color represents the projected spin density (y-component) on the top surface of forward propagating states. (b) Density-of-states vs energy for the slab, wire, and a cubic dot with the same thickness of 4QLs. Inset of (b), cross section view of the wire atomic structure. (c) Total projected spin density on the top surface of forward propagating states vs energy. (d) Carrier density vs Fermi energy at 300 K. 61

Figure 4.2.2 . (a) Two degenerate and orthogonal wave-functions of the wire corresponding to the energy and k-vector indicated by the dashed lines in Figure 4.2.1 (a). (b) Charge-to-spin conversion

efficiency, i.e. the ratio between spin accumulation at the top surface and charge current, as a function of carrier concentration, calculated in the linear response with or without an applied electric field F. Inset of (b), conversion efficiency of the dot geometry, averaged over the range of carrier densities (n) $1\times10^{21} - 3\times10^{21}$ cm^{-3} and plotted as a function of confinement size, for dots with cubic shape (blue symbols) and for dots with the same thickness of 4QLs in the z direction and different size in the xy-plane (red symbols). 63

Figure 4.2.3 Effect of orientation on charge-to-spin conversion efficiency: Black and purple lines are efficiency ratio for slab and dot at zero electric field obtained by projected the spin density y component on the top surface. The orange line represents the spin density z component of the dot projected to the side surface. Size of the dot is 4x4x4 nm. 65

Figure 5.2.1 Raman spectrum of 16 nm thick BS thin film. 67

Figure 5.2.2 (a) XPS spectra of BS sample (b) High resolution 4f bands of Bi and (c) 3d bands of Se, respectively. 68

Figure 5.2.3 (a) Temeperature dependent resistivity of 4 nm thick BS film. (b) Hall measurement of 4 nm thick BS film at room temperature. 69

Figure 5.3.1 Spin-pumping into $Bi_{0.43}Se_{0.57}$ and structural characterization. (a) Schematics of the experimental set up for the spin-to-charge conversion (b) TEM image of the BS8 sample. 70

Figure 5.3.2 Conversion of spin-to-charge current by spin-pumping in to sputtered $Bi_{43}Se_{57}$ thin films (a) The spin-pumping voltage measured in BS2 sample at 9 GHz excitation frequency. (b) The spin-pumping voltage in BS2 sample as a function of the excitation frequency. (c) The spin-pumping voltage as a function of the BS film thickness at 9 GHz excitation frequency and 2.0 V excitation amplitude. (d) The spin-pumping voltage as a function of the excitation amplitude for different samples at 9 GHz excitation frequency. 73

Figure 5.3.3 Characterization of spin-injection efficiency and inverse Edelstein effect length (a) Excitation frequency as a function of resonance field (b) The line-width as a function of the excitation frequency (c) Spin-mixing conductance (right axis) and damping constant (left axis) versus BS film thickness (d) Inverse Edelstein effect length as a function of the BS film thickness. 75

Figure 5.4.1 Characterization of α and M_s of control CoFeB sample. (a) The spin-pumping voltage measured in CoFeB sample at 9 GHz excitation frequency. (b) Line-width as a function of the excitation frequency. (c) Excitation frequency as a function of resonance field. 76

Figure 5.5.1 Spin-pumping in Sub/Pt (10 nm)/CoFeB (5 nm)/MgO (2 nm)/Ta (2 nm) (a) The spin-pumping voltage measured in Pt/CoFeB sample at 9 GHz excitation frequency. (b) Line-width as a function of the excitation frequency. (c) Excitation frequency as a function of resonance field.(d) ISHE voltage as a function of excitation voltage. 78

Figure 5.6.1 Influence of interfacial layers on spin-to-charge current conversion (a) The output dc voltage due to spin-to-charge current conversion in the BS4 sample (b), (c) Influence on the spin-pumping voltage due to the insertion layers MgO (0.5 nm) and Ag (2 nm), respectively. (d) The spin-pumping voltage as a function of the excitation amplitude in BS-Ag sample. (e) The linewidth as a function of the excitation frequency. 79

Figure 6.3.1 Characterization of YIG and BS films. (a) and (c) AFM surface images of GGG/YIG (20 nm) and Si/SiO2/MgO (2 nm)/ BS (8 nm) samples, respectively. (b) FMR profile of the GGG/YIG (20 nm) sample. (d) TEM cross-section image of a YIG/BS sample.......................... 84

Figure 6.3.2 Spin-to-charge conversion by sputtered BS thin films. (a) Schematic of spin-to-charge conversion (b) and (c) The spin-pumping voltage measured in YBS4 and reference YPt samples at 6 GHz excitation frequency, respectively (d) The line-width as a function of excitation frequency is presented. The red solid line is linear fit to extract α 85

Figure 6.3.3 Characterization of inverse Edelstein effect length (a) Excitation frequency as a function of resonance field fits according to the Kittel formula (b) Spin-mixing conductance of BS samples as a function of BS film thickness. (c) Spin-to-charge conversion voltage as a function of the input excitation amplitude. (d) Spin-pumping voltage as a function of excitation frequency. (e) IEE length as a function of the BS film thickness, which shows thickness dependence. 88

Figure 6.4.1 (a) Hall resistance of YIG/BS at room temperature. (b) Out-of-plane AMR of Si/SiO2/BS (4 nm). (c) Out-of-plane AMR of YIG/BS (4 nm). 90

Index Table

Terminology	Symbol	Terminology	Symbol
Si/SiO_2/MgO (2 nm)/$Bi_xSe_{(1-x)}$ (4-40)/CoFeB (5 nm)/MgO (2 nm)/Ta (5 nm)	BS4-BS40	Charge current density in $Bi_xSe_{(1-x)}$	J_{BS}
Hall resistance	$R_H(I,\alpha)$	Spin-density	J_S
Difference in Hall resistance	$R_{DH}(I,\alpha)$	Magnetization switching critical current density	J_{SW}
Angle between external field and current flow	α	Spin conductivity	σ_S
Angle between magnetization and current flow	β	Charge conductivity	σ_c
Anomalous Hall resistance	R_{AHE}	Spin torque efficiency	θ_S
Planar Hall resistance	R_{PHE}	Spin-diffusion length	λ
Out-of-plane current induced spin-orbit field	H_{OOP}	Saturation magnetization	M_s
In-plane current induced spin-orbit field	H_T	Spin Hall angle	θ
Out-of-plane anisotropy field	H_K	Spin-mixing conductance	$g_{\uparrow\downarrow}$
Externally applied magnetic field	H_{ext}	YIG/BS	YBS
Resonance field	H_0	Gyromagnetic ratio	γ
Line-width	ΔH	Anti-symmetric component of voltage	A
Symmetric component of voltage	S	Inverse Edelstein effect length	λ_{IEE}

Chapter 1. Introduction

1.1 Motivation

Currently, the scaling of conventional complementary metal oxide semiconductor (CMOS) devices fulfill the growing demand of a faster and more powerful microprocessor [1–4]. However, CMOS devices are limited by factors including device reliability and power consumption due to an increase in density and static leakage current. In CMOS devices charge current is used to transfer and store data in a capacitor, consequently energy is dissipated due to Joule heating during operation. Spintronic devices use spin-based transport effects that couple the intrinsic spin of electrons and their associated magnetic moments, in addition to electronic phenomena that comes from the fundamental electronic charge of electrons. Magnetic materials are used in spintronic devices including memory and computational devices. One immediate advantage of using the magnetic material in spintronics devices is non-volatility. In addition, in the case of spin-based devices, there is no motion of the charges the flipping of spin is required for device operation, which prevents Joule heating related energy dissipation. In the past decade, there has been an intense study of ultra-low power and faster spin-based devices in memory and logic applications.

In a conventional spintronic device, the spin-density is generated by a ferromagnet (FM) that can exert torque on non-collinear magnetization of another FM layer by transferring its spin-angular momentum. The resulting torque, which can rotate the magnetization direction is known as the spin-transfer torque (STT) [5,6]. Recently, charge-to-spin conversion has been observed via spin-orbit coupling (SOC). SOC generated spin-density can exert torque on the FM known as spin-orbit torque (SOT). SOT-based memory and logic devices are superior to STT-based devices because they do not require a separate polarizer layer for the generation of spin-density and can generate spin-density much more efficiently [2,3,7,8]. Materials with high atomic number, Rashba interfaces, and topological insulators (TIs) are prime candidates for an efficient spin-density generator [9]. The use of TIs as a spin-density generator in SOT-based spintronic devices could

lead to a lower writing current density and, thus, significantly improved energy efficiency and much better device reliability.

1.2 Introduction to the fundamental spintronic device

The fundamental spintronic device used for memory and computation is a spin-valve. A typical stack structure of the spin-valve device consists of two FMs separated by a non-magnetic spacer layer as shown in Figure 1.2.1. The spacer layer can be a light metal or an insulating layer. The spin-valve device, which has a conducting spacer is called giant magnetoresistance (GMR) spin-valve and with an insulating barrier is called magnetic tunneling junction (MTJ) spin-valve. Spin-valve devices are currently being used as read sensors in hard disk drives (HDD) and memory devices [10]. Charge current injected in to the FM can produce spin-density due to the number of available spin up states and spin down states being different at the Fermi level. The spin-density generated by FM is utilized to switch magnetization in spin-based magnetoresistive random access memory (MRAM) devices, which is commonly known as STT-MRAM. In STT-MRAM the writing of the data bits is done by the STT and the reading of the data bits is done by measuring the magnetization dependent resistance. In GMR spin-valves, when the FMs are parallel only one type of spin direction, either up or down, gets scattered providing a low resistance state ; whereas for the case of antiparallel FMs both spin-up and spin-down states get scattered, which results in a high resistance state. In case of MTJ spin-valves, when the FMs are parallel the number of available initial and final states at the Fermi level is large as a result coherent tunneling of large number of spin-polarized electrons is possible, which results in low resistance state [11]. When the FMs are anti-parallel, the number of available initial and final states at the Fermi level is small so less spin-polarized electrons tunnel resulting in a higher resistance.

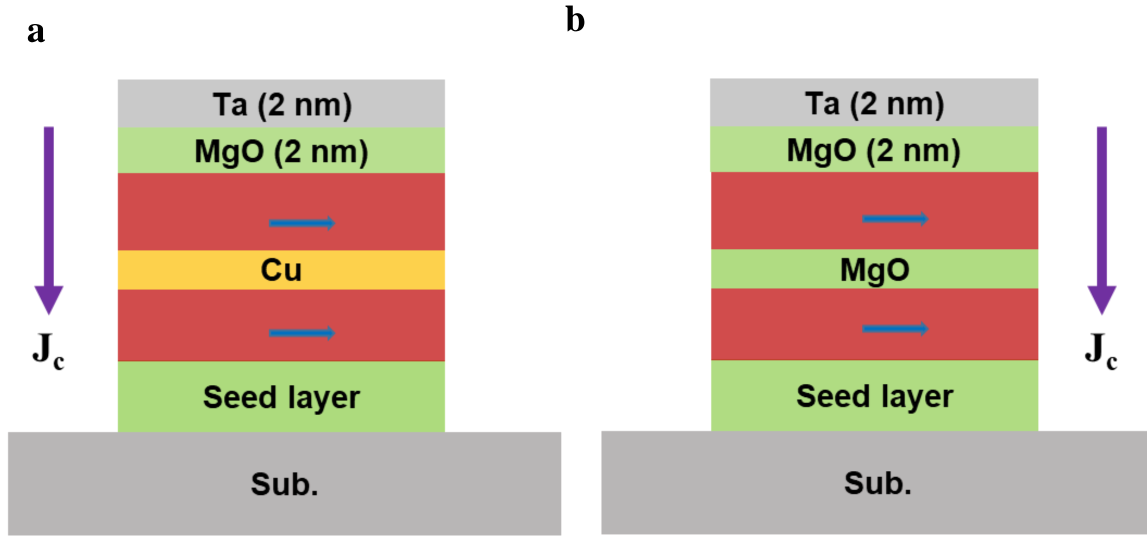

Figure 1.2.1 (a) Shows schematic stack structure of GMR spin-valve with Cu as spacer and (b) Shows MTJ spin-valve stack structure with tunnel barrier MgO. The blue arrows indicate magnetization direction.

The critical switching current density of the perpendicular ferromagnetic layer via STT is given by following relation [12]:

$$J_{sw} = \frac{\alpha e M_s H_K V}{\hbar P} \tag{1.2.1}$$

where α is the damping constant, P is spin-polarization of the FM, e is the electronic charge, M_s is the saturation magnetization, H_K is the anisotropy field, V is the volume of the switched magnetic layer. Perpendicular FMs offer high thermal stability, high-density, and can be switched with low J_{sw} compared to the in-plane FM. However, a large current density is still required for data writing , which can break down the tunneling barrier, as well the large α of perpendicular FMs with large H_K is a limiting factor for reducing the J_c and scaling.

1.3 Spin-current generation via the spin Hall effect

The limiting factors present in STT-MRAM devices can be reduced by using the spin-density generated by SOC [7]. Elements with high atomic number such as Pt, Ta, W, Bi etc have large SOC. Charge current injected into high SOC materials along the longitudinal direction is scattered in the transverse direction depending upon the electron's spin-polarization direction due to the spin-orbit field as shown in Figure 1.3.1. The generation of spin-current due to the SOC in HMs is named the spin Hall effect by Hirsch [13], although, theoretically it was first predicted by Dyakonov and Perel [14]. *ab initio* calculations performed by Guo et al., revealed that the spin-orbit splitting of double degenerated d-bands close to the Fermi level is the reason for intrinsic spin Hall effect in Pt [15]. Experimental detection of spin-current generation due to the spin Hall effect was first observed using an optical method in unstrained semiconductor GaAs and in strained InGaAs [16]. First inverse spin Hall effect (ISHE) was detected electrically in Al [17]. Kimura et al., detected the ISHE using non-local lateral spin-valve devices from the heavy metal Pt [18]. In addition to the band structure originated intrinsic spin Hall effect, defects as well as dopants can also generate spin-current, which is referred as extrinsic spin Hall effect [19–21].

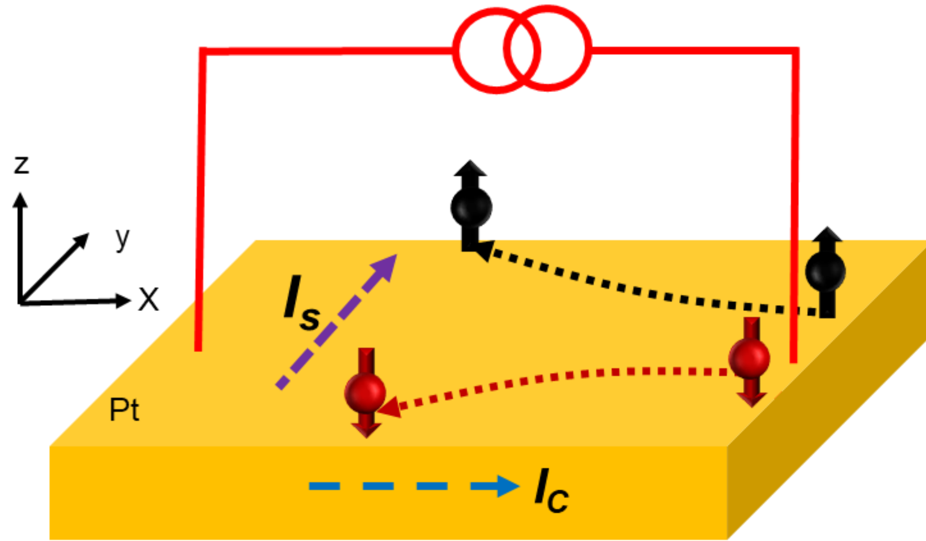

Figure 1.3.1 Shows a schematic diagram of the spin Hall effect in Pt. The electrons with opposite spin directions are deflected in opposite direction due to the spin-orbit field. The spheres represent the electron and the arrows in the spheres represent spin-magnetic moment.

The spin-density (J_s) generated by spin Hall effect is given by,

$$\vec{J}_s = \theta(\vec{J}_c \times \hat{\sigma}) \qquad (1.3.1)$$

Where θ, $\hat{\sigma}$ and J_c are spin Hall angle, spin-polarization unit vector, and charge-current density in the HM, respectively.

1.4 Non-equilibrium spin-accumulation via spin-orbit interaction originated from broken symmetry

Semiconductors, such as in GaAs or InSb have Dresselhaus and Rashba spin-orbit coupling originating from the bulk inversion asymmetry [22–25]. Additionally, heterostructures lacking structural inversion symmetry, Bi/Ag [26], Pt/Co/AlOx [27], and MoS_2/CoFeB [28], have Rashba

spin-orbit coupling. The Hamiltonian that describes the Rashba spin-orbit interaction is given by [24],

$$H_R = \alpha_R (\vec{\sigma} \times \vec{p}).\hat{z} \tag{1.4.1}$$

where σ is the Pauli matrix, p is the electron momentum and $\hat{z}$ is the unit vector along the symmetry broken direction. The Rashba and Dresselhaus spin-orbit interaction split the energy bands as shown in Figure 1.4.1 (a) and orthogonally locks the spin of the charge carrier with its momentum. At the Fermi surface spin-texture of the split bands have opposite chirality. Experimentally, using angle-resolved photoemission spectroscopy (ARPES) spin-split sub-bands were observed in Bi (111) [29], Bi/Ag and Pb/Ag [30], and Pb [31]. The charge current injected in the materials with the Rashba spin-orbit interaction are deflected by the Rashba magnetic field given by,

$$B_R = \frac{\alpha_R}{g\mu_B} (\vec{p} \times \hat{z}) \tag{1.4.2}$$

where g and μ_B are the Lande's g-factor and the Bohr magneton, respectively. The Rashba magnetic field preceses the spin of carriers, which are not aligned along the Rashba field, eventually aligning towards the Rashba field and generate a spin-polarization. In k-space, externally applied electric field shifts both Fermi contours originated by Rashba field along the electric field direction as shown in Figure 1.4.1 (b). The magnitude of the opposite spins present in the inner and outer Fermi contours are not the same, as a result there is net spin-density accumulation [25,32]. The net spin-density accumulation by the Rashba-Edelstein effect is given by [32],

$$S = \frac{\alpha_R m}{e\hbar} (\hat{z} \times \vec{J}_c) \tag{1.4.3}$$

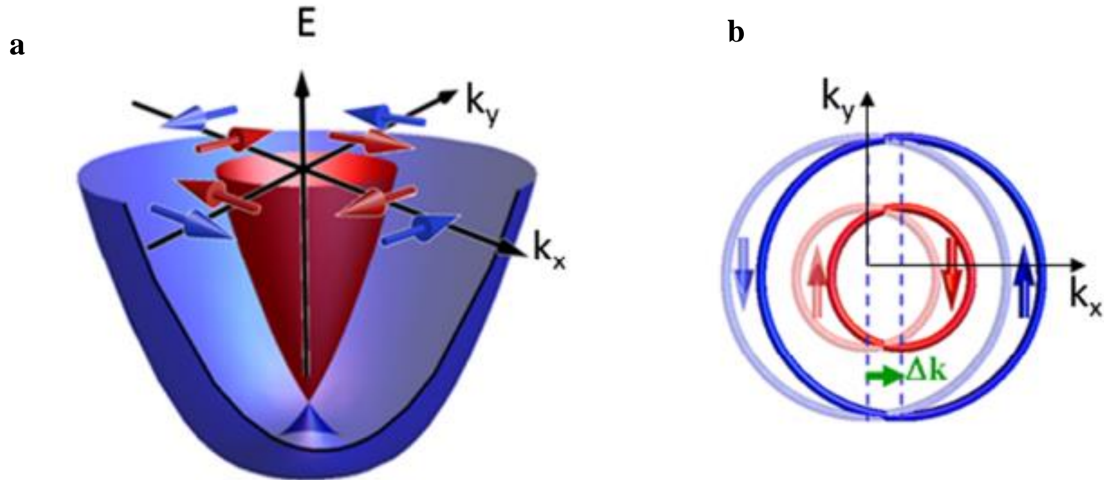

Figure 1.4.1 (a) Schematic diagram showing the Rashba SOC split spin-polarized bands at the Fermi level, electron spin is represented by red and blue arrows. (b) The electric field applied along the x-axis in the Rashba potential shifts the spin-polarized Fermi contours resulting in a non-equilibrium spin accumulation along the y-direction. Reprinted from Ref. [33] *with permission from the American Physical Society.*

1.5 Non-equilibrium spin-accumulation via spin-momentum locking in topological insulators

According to the band theory of solids, a trivial insulator consists of an occupied valence and empty conduction bands separated by an energy gap. In materials having high spin-orbit coupling the conduction and valence bands are inverted [34,35]. The inversion of the bands allow for conduction through only the surface states of the material resulting in an insulating bulk. These surface sates are gapless, similar to the edge states in the conventional quantum Hall effect [36]. Materials with such a property are known as topological insulators (TIs). Materials having high atomic number and semiconductors with a small band gap equivalent to spin-orbit coupling are the main candidates for TIs. Zhang et al., showed analytically for Bi_2Se_3 at the Γ point, inversion of p_z bands of Bi and Se occurred due to the spin-orbit coupling present in the Bi and Se atoms [37].

TI surface states can be described by the Dirac Hamiltonian: $H_D \propto (\vec{\sigma} \times \vec{p}).\hat{z}$, which leads to linear dispersion.

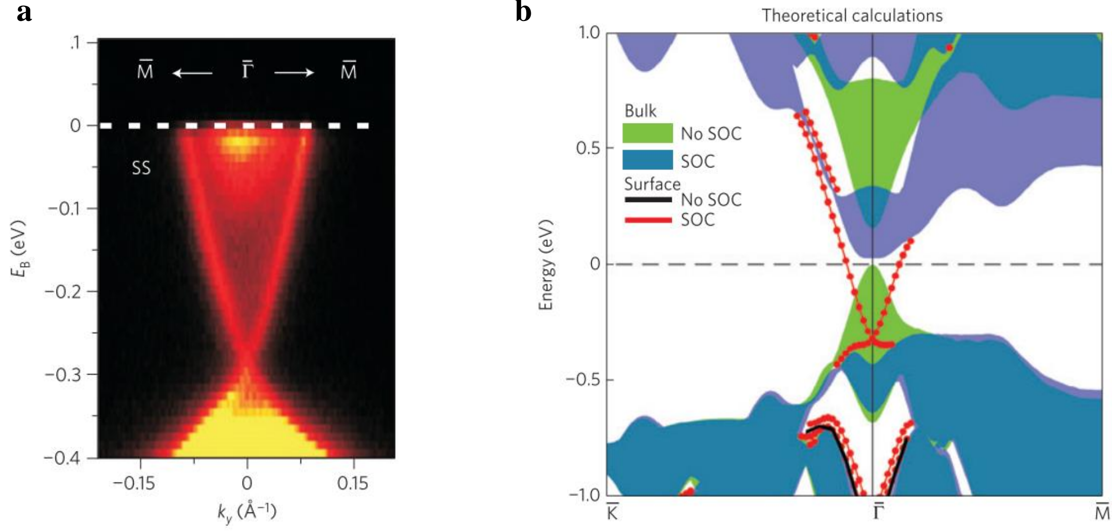

Figure 1.5.1 (a) Band structure of Bi_2Se_3 *obtained by angle resolved photoemission spectroscopy (ARPES). (b) Band structure calculation of* Bi_2Se_3 *where shaded regions are projection of bulk bands. Reprinted from Ref.* [38] *with permission from the Nature Publishing Group.*

The surface states are robust against backscattering due to the protection from time-reversal symmetry [34,35]. Roushan et al., studied the robustness of surface states using scanning tunneling spectroscopy in $Bi_{(1-x)}Sb_x$, and found that, despite disorder present due to random alloying, backscattering is absent [39]. Xia et al., observed large single Dirac cone in Bi_2Se_3 by using ARPES as shown in Figure 1.5.1. The surface states of TIs are spin-polarized and the motion of the charged particles is dictated by the spin-direction. At k-space, electric field shifts the fermi-contour as a result non-equilibrium spin-accumulation occurs, which is given by,

$$\delta S = \frac{\hbar k_f \delta k_x}{2} = \frac{e k_f E_x \tau}{2} \tag{1.5.1}$$

where k_f, E_x, and τ are the Fermi vector, electric field and spin-relaxation time, respectively.

1.6 Torques on the ferromagnet via spin-accumulation generated by spin-orbit coupling

In order to take advantage of the efficient charge-to-spin conversion by spin-orbit interaction, a heterostructure of a spin-source with a FM is formed. A. Manchon and S. Zhang studied the transfer of spin-angular momentum to a FM due to the non-equilibrium spin-accumulation generated from the Rashba spin-orbit coupling [40]. The non-equilibrium spin-accumulation transfers spin-angular momentum to the magnetization through the exchange interaction. The magnetization dynamics due to the current induced SOT is given by the Landau Lifshitz and Gilbert (LLG) equation,

$$\frac{d\hat{m}}{dt} = -\gamma \hat{m} \times \vec{H}_{eff} + \alpha \hat{m} \times \frac{d\hat{m}}{dt} + \beta_J (\hat{\sigma} \times \hat{m}) + \frac{\hbar J_s}{2eM_s t_{FM}} \hat{m} \times (\hat{\sigma} \times \hat{m}) \tag{1.6.1}$$

where H_{eff} , α , $\hat{\sigma}$, β_J , J_s , and t_{FM} are the effective magnetic field exerting on the magnetization, damping constant, spin-polarization unit vector, field-like torque (FLT) co-efficient, spin-density, and thickness of the FM, respectively. $H_{eff} = H_m + H_{ext}$, where H_m includes the demagnetization field, magneto-crystalline anisotropy field, and H_{ext} is static external field. The first term in the right hand side of Eqn. (1.6.1) precesses magnetization around the H_{eff} direction whereas the second term is the damping term, which aligns magnetization towards the external field direction. Moreover, the third term is the torque via current induced SOT, which also precesses magnetization like H_{eff} so it is named as the FLT. The fourth term is also the current induced SOT, which has same form as the damping torque towards H_{eff} so it is named anti-damping like torque (ADLT). The ADLT can also behave like the damping like torque depending upon the current flow and magnetization directions. The transfer of spin-angular momentum by the spin-accumulation can be studied by using the drift-diffusion model [41] and the semi-classical Boltzmann equation [42]. Haney et al., performed analytical calculations based on the drift-diffusion model and Boltzmann

equation and found that both approaches agree in most regimes [43]. However, the Boltzmann equation failed to explain thickness dependence of the torques.

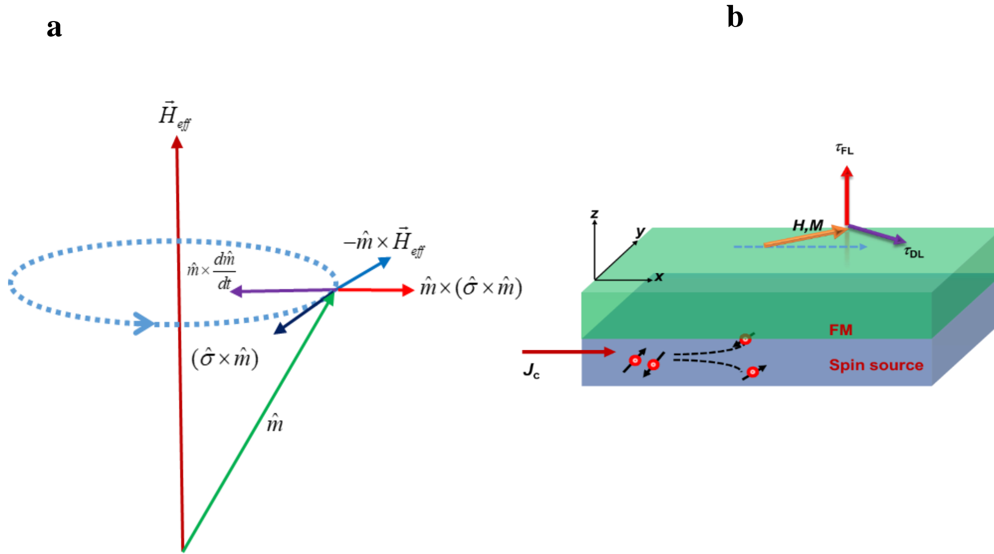

Figure 1.6.1 (a) Shows the representation of the various torques on a FM. SOTs change direction if direction of current flow or magnetization is changed (b) Shows a typical stack structure for the characterization of SOT. In this case, the spin source is a HM, which generates spin-current along the vertical direction via the spin Hall effect. For in-plane magnetization the ADLT is along the in-plane direction whereas the FLT is along the out-of-plane direction.

The SOTs in the heterostructures of HM/FM were reported in Pt/NiFe [27,44–46], Ta/CoFeB [2,47–50], W/CoFeB [8,51], Hf/CoFeB [52], Pd/Co [53]. The main techniques used to extract SOTs are spin torque ferromagnetic resonance (ST-FMR) [44–46], anomalous Hall [2,51], dc planar Hall [54,55], and second harmonic Hall [21,47,56]. The figure-of-merit of the charge-to-spin conversion is known as the spin-torque efficiency, $\theta_S = \frac{\sigma_s}{\sigma_c}$, where σ_c is the charge conductivity and σ_s is the spin-conductivity, which measures the strength of the ADLT. The θ_S of Pt, Ta, and W are calculated using ST-FMR to be 0.056 [45], -0.15 [2], and -0.3 [8], respectively.

Experimentally reported value of σ_s for Pt is 2.8 × $10^5 \frac{\hbar}{2e}$ $\Omega^{-1}m^{-1}$, which is comparable to the theoretically predicted values [15,45]. The sign of the θ_S in HMs depends upon the filling of the d-band [15]. If the d-band, is more than half-filled θ_S is positive whereas θ_S is negative if the band is less than half-filled. The crystal structure of the HM affects θ_S, for example α-Ta has smaller value of θ_S compared to β-Ta [2].

In HMs, the main source of ADLT is the intrinsic spin Hall effect whereas the origin of FLT is still controversial, but its main origin is believed to be the interfacial symmetry breaking. The ADLT switches sign in Ta and Hf as the thickness of the films decreased to ~ 0.4 nm and ~ 2 nm, respectively. In general, the ADLT in HMs increases with increasing thickness and it saturates after certain thickness, which can be explained by the drift-diffusion model. The FLT in Ta also switches sign in the thickness range 0.3-0.4 nm and at lower temperatures [47,57]. The sign change of the torques in thinner films is believed to be due to the competition between the spin Hall and Rashba-Edelstein effect generated torques. The ADLT remains almost constant with the temperature if the origin is intrinsic spin Hall effect where as its value increases if it is originated from the extrinsic spin Hall effect [21,58,59]. Furthermore, the ADLT remains almost constant with FM layer thickness whereas the FLT shows FM layer thickness dependence [47]. The reported values of the ADLT (FLT) in as deposited perpendicular Ta/CoFeB/MgO [50], in-plane Pt/Fe/MgO [54], and in-plane Ta/Fe/MgO [54] stacks are -3.2 (-2.1), 2.9 (3.9) and -6.8 (-8.8) Oe per 10^6A/cm^2, respectively.

Chernyshov et al. reported SOT in the ferromagnetic p-type seminconductor Ga(Mn)As Semiconductors [60]. The SOT was determined to be 5.3 Oe per 10^6 A/cm^2 in Ga(Mn)As at 40 K. Kurebayashi et al., reported the ADLT is originated from the Berry curvature in Ga(Mn)As [22]. Chen et al., observed the ADLT and the FLT in GaAs (100 nm)/Fe (5 nm) comparable to HM/FM stacks at room temperature [61]. The θ_S in two dimensional electron gas (2DEG) STO/LAO/CoFeB is determined to be 6.3 at room temperature [62]. Shao et al., reported the Rashba-Edelstein effect

in the transition metal dichalcogenides MoS_2/CoFeB and WSe_2/CoFeB. The ADLT is negligible in both MoS_2/CoFeB and WSe_2/CoFeB whereas the FLT is sizeable with a spin-conductivity of 2.88 and $5.52 \times 10^3 \frac{\hbar}{2e}$ $\Omega^{-1}m^{-1}$, respectively [28]. However, Zhang et al. reported that in MoS_2/Py the ADLT is much stronger compared to the FLT [63]. In $NbSe_2$/Py the ADLT is size-able with a σ_s of the order of $10^3 \frac{\hbar}{2e}$ $\Omega^{-1}m^{-1}$ [64].

Mellnik et al. first demonstrated torque on Py due to the charge-to-spin conversion by a TI, Bi_2Se_3 at room temperature by using the ST-FMR technique [65]. The room temperature θ_S is reported for Bi_2Se_3/Py and is as large as 3.5, which is an order of magnitude larger than the values reported in HMs, even though the Bi_2Se_3 film is not an ideal TI at room temperature as the Fermi level touched bulk bands [65]. The FLT torque is larger than the ADLT in Bi_2Se_3/Py by a factor of 1.37. Fan et al. reported the θ_S in $(Bi_{0.5}Sb_{0.5})_2Te_3/(Cr_{0.08}Bi_{0.54}Sb_{0.38})_2Te_3$ to be large as 425 at 1.9 K using the SHH technique [66]. These two reports gained attention of the spintronics community for the use of TIs as a spin-generator. Wang et al. performed temperature dependent SOT measurements in Bi_2Se_3/CoFeB via the ST-FMR technique. The θ_S gradually increases with a decrease in temperature and its values at 300 and 50 K are 0.047 and 0.42, respectively. The FLT and ADLT are comparable in Bi_2Se_3/CoFeB. Furthermore, Kondou et al. reported Fermi level dependent charge-to-spin conversion in tri-layers of $(Bi_{1-x}Sb_x)_2Te_3$ (8 nm)/Cu (8 nm)/$Ni_{80}Fe_{20}$ at room temperature by tuning the concentration of Sb [67]. The insertion of a Cu layer is used to avoid any proximity induced effects between FM and TI layers. The charge-to-spin conversion in $(Bi_{1-x}Sb_x)_2Te_3$ (8 nm) is measured using the ST-FMR method and is at a maximum when the Fermi level is at the bulk bands and a minimum when it is at the Dirac point. In ideal TI, the topological protection is robust at the Dirac point. The FLT in $(Bi_{1-x}Sb_x)_2Te_3$ (8 nm)/Cu (8 nm)/$Ni_{80}Fe_{20}$ is negligible. Recently, Khang et al. reported the θ_S in BiSb/MnGa to be as large 52 with a remarkably large σ_c value of 2.5×10^5 $\Omega^{-1}m^{-1}$.

1.7 Spin-orbit torque switching of magnetization

Chernyshov et al., demonstrated SOT switching of the magnetization in Ga(Mn)As at 40 K under the presence of a 60 Oe external field along the current flow direction [60]. Miron et al., demonstrated the first SOT switching of a perpendicular FM in a Pt/Co/AlOx stack in which the spin-density is generated via the Rashba-Edelstein effect [68]. Liu et al., performed switching of perpendicular Co in the Pt/Co/AlOx stack structure but argued that the origin of the SOT is the spin Hall effect [69]. Liu et al., demonstrated switching of both in and out-of-plane CoFeB via the SOT from Ta [2]. The perpendicular CoFeB switching was monitored via the anomalous Hall effect, whereas the in-plane switching was monitored by another CoFeB layer separated by a thin MgO layer. The in and out-of-plane CoFeB switching via the SOT from W was demonstrated by Pai et al., and Hao et al. [8,70]. The SOT switching of magnetization in HM/FM bilayer systems is achieved with a J_{sw} on the order of 10^6-10^8 A/cm^2 at room temperature [2,68,69]. Recently, switching of the perpendicular ferromagnetic bulk semiconductor (Ge,Mn)Te is achieved by the Rashba-Edelstein effect [71]. The SOT switching of perpendicular magnetic insulators is also achieved in thulium iron garnet (TIG)/Pt [72] and barium ferrite (BaM)/Pt [73]. Fukami et al. studied SOT switching in three different geometries as shown in Ta/CoFeB/MgO as shown in Figure 1.7.1 [74]. In type z geometry current flow, magnetization, and applied external field are along x, z, and x directions, respectively. In type y geometry current flow and magnetization are along x and y, respectively. In type x geometry current flow, magnetization, and applied external field are along x, x, and z directions, respectively.

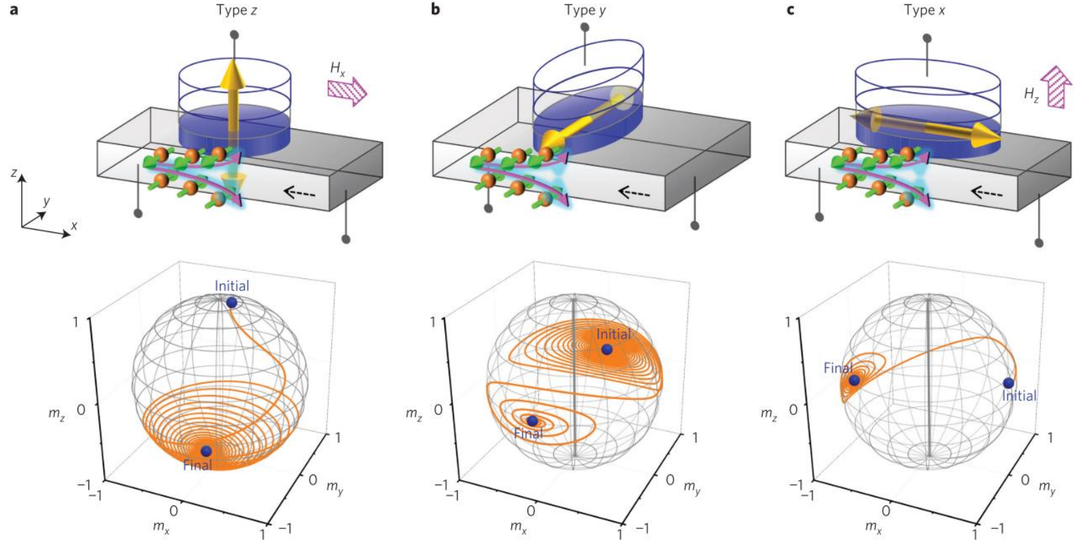

Figure 1.7.1 At the top panel: (a), (b), and (c) Schematic diagrams showing the magnetization direction along the z, y, and x, respectively. The charge current is converted into the spin-density via the spin Hall effect from Ta. At the bottom panel of (a), (b), and (c) magnetization dynamics simulations using the macro-spin model due to SOT is provided. Reprinted from Ref. [74] *with permission from the Nature Publishing Group.*

The magnetization switching current density for the type z structure is given by,

$$J_{sw} = \frac{2eM_s t_{FM}}{\hbar\theta_S}\left(\frac{H_K}{2} - \frac{H_{ext}}{\sqrt{2}}\right) \tag{1.7.1}$$

where H_K and H_{ext} are anisotropy and externally applied fields, respectively.

For the type y structure, the switching current density is given by,

$$J_{sw} = \frac{2e\alpha M_s t_{FM}}{\hbar\theta_S}\left(H_{K,in} + \frac{H_{k,out}}{\sqrt{2}}\right) \tag{1.7.2}$$

where $H_{K,in}$ and $H_{k,out}$ are in-plane and out-of-plane effective anisotropy fields, respectively. In

the type z and x, the switching of the magnetization occurs in a short time as soon as SOT is applied, where as in the type y it takes many precessions before the switching occurs. The J_{sw} in y and x geometries is 1.0 and 4.3 × 10^7 A/cm^2, respectively. The magnetic structure is same but the switching behavior and J_{sw} are different, which means the SOTs are not the same for these two geometries.

For the practical applications, efficient charge-to-spin conversion by TIs can also be demonstrated by switching perpendicular magnetization. The switching of a magnetically doped TI $(Cr_{0.08}Bi_{0.54}Sb_{0.38})_2Te_3$ layer at 1.9 K has been observed via the SOT from the TI, but with a much lower J_{sw} (8.9 × 10^4 A/cm^2) compared to HM/FM [66]. Room temperature switching of perpendicularly magnetized CoTb [75] and in-plane NiFe [76] layers have been reported via the SOT from Bi_2Se_3 with a J_{sw} of 3.0 × 10^6 and 5 × 10^5 A/cm^2, respectively. Khang et al., reported the switching of perpendicularly magnetized MnGa at room temperature with a J_{sw} of ~1.5 × 10^6 A/cm^2 via SOT from highly conductive $Bi_{0.9}Sb_{0.1}$ [77].

1.8 Spin-to-charge conversion via spin-orbit coupling

The detection of spin-current is important for spintronic device applications since it can be used for the detection of the state of the magnetization. According to the Onsager reciprocity principle charge-to-spin conversion should also yield spin-to-charge conversion. The spin-pumping method can be used to inject a pure spin-current into the NM layer. In addition, the conductivity mismatch between the FM and NM layers is not an issue in the spin-pumping technique. The rf precession of the magnetization pumps spins into the NM layer at the FMR condition in spin-pumping. The magnetization dynamics of the FM layer is given by the LLG equation,

$$\frac{d\hat{m}}{dt} = -\gamma\hat{m}\times\vec{H}_{eff} + \alpha\hat{m}\times\frac{d\hat{m}}{dt} \tag{1.8.1}$$

where $H_{eff} = H_m + H_{ext} + h_{rf}(t)$ and $h_{rf}(t)$ is the rf field.

According to the theoretical model by Tserkovnyak et al. [78,79], instantaneous rf precession of the magnetization pumps spin-current at FM/NM interface and that current is given by,

$$J_s^0 = \frac{\hbar}{8\pi}\mathrm{Re}(2g_{\uparrow\downarrow})[\vec{m}\times\frac{d\vec{m}}{dt}] \tag{1.8.2}$$

where $g_{\uparrow\downarrow}$ is real part of the spin-mixing conductivity and it is given by,

$$g_{\uparrow\downarrow} = \frac{4\pi M_s t_{FM}}{g\mu_B}(\alpha - \alpha_{\mathrm{int}}) \tag{1.8.3}$$

where α_{int} is the intrinsic value of the FM damping constant. $(\alpha - \alpha_{\mathrm{int}})$ is the damping enhancement due to the transfer of spin-angular momentum from FM to the NM layer.

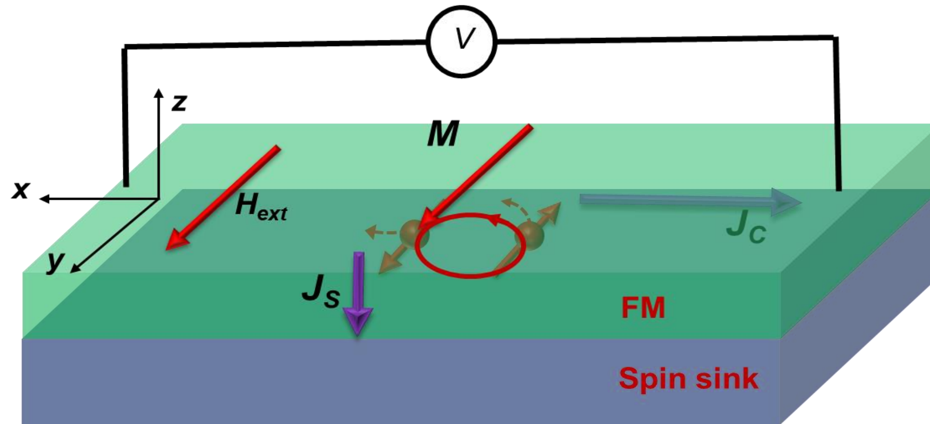

Figure 1.8.1 Schematic diagram of spin-pumping. RF field precesses the magnetization of the FM at an excitation frequency in the GHz range. In order to meet the FMR condition, H_{ext} is swept along the y-axis. At FMR, the FM pumps spins into the spin sink in the vertical direction. The spins

injected into the spin sink get converted into a measurable open circuit voltage due to a mixture of ISHE, IEE, and IREE effects.

The conversion of J_s into an electric field via ISHE is given by,

$$E_{ISHE} \propto \vec{J}_s \times \hat{\sigma} \quad (1.8.4)$$

this electric field produces a measureable open circuit voltage, which is given by,

$$V_{ISHE} = wR\lambda\theta \ \tanh(t/2\lambda)J_S \quad (1.8.5)$$

where x, θ, R, and λ are the thickness, spin Hall angle, device resistance, and spin-diffusion length of the HM, respectively.

Satoh et al., reported first electrical detection of a spin-current by spin-pumping from Py into Pt at room temperature [80]. Furthermore, spin-pumping from a magnetic insulator such as yttrium iron garnet into the HMs has also reported at room temperature [81]. In order to extract θ and λ, V_{ISHE} is measured for different thickness of the HM. In addition to the ISHE in HMs [82–84], spin-to-charge conversion has been observed in semiconductors [61,85,86]. The non-equillibrium spin-density created by spin-pumping is converted into a dc voltage by the inverse Edelstein effect (IEE) in crystalline TIs [32,33,87–94] grown by molecular beam epitaxy (MBE), and the inverse Rashba-Edelstein effect (IREE) in interfaces such as Ag/Bi [26,95,96], Fe/Ge [97], Cu/Bi_2O_3 [98], LAO/STO [99,100], and in two dimensional materials [101,102].

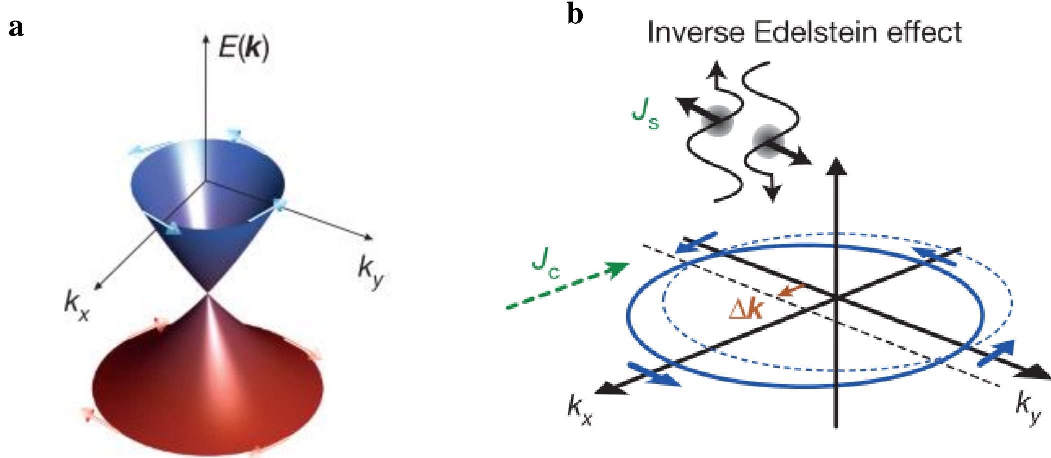

Figure 1.8.2 (a) Schematic diagram the showing spin-polarized band structure of a TI at the Fermi level (b) Spin-pumping into TI surface states shift the Fermi contour, which results in more electrons on one side of the Fermi contour than on another side. Reprinted from Ref. [9] *with permission from Nature Publishing Group.*

In the k-space, the non-equilibrium spin accumulation at the TI and Rashba interfaces along the y-axis shifts the Fermi-contour along the x-axis and induces an electric field along the x-direction. The figure of merit of spin-to-charge conversion in TIs is called the inverse Edelstein effect length (λ_{IEE}) and is given by [26,103,104],

$$\lambda_{IEE} = \frac{J_C}{J_s} = \frac{V_{IEE}}{RwJ_s} \tag{1.8.6}$$

Where w is the width of the device. The J_C in TIs and interfaces, 2DEG, and 2D materials is assumed to be two-dimensional and has the units of A/m. λ_{IEE} is equivalent to the mean free path of TIs. The spin rotation in TIs is caused by the momentum scattering from spin-momentum locked TI bands [104]. In terms of the momentum scattering time (τ_m) the λ_{IEE} is given by,

$$\lambda_{IEE} = v_f \tau_m \tag{1.8.7}$$

Where v_f is Fermi velocity.

Chapter 2. Experimental methods

2.1 Thin film growth and characterization techniques

2.1.1 Sputtering

All the thin film samples used in my projects were prepared using magnetron sputtering. In DC sputtering, the materials to be deposited are set at negative potential where as the substrate on which films are to be deposited is connected with the to the ground as shown in Figure 2.1.1 (a). The voltage applied between the parallel plates of the target and substrate is on the order of kilo Volts. Inert gas such as argon is used in the sputtering process as the working gas. The stray electrons present near the target are accelerated towards the substrate due to the electric field between the target and substrate. The momentum gained by the stray electron is sufficient to remove electron of an Ar gas atom. After loss of electron, the Ar gas atom becomes positively ionized. The ionized gas atoms gain momentum due to the electric field and transfer it to the target and eventually remove atoms from the target. The ejected atoms off the target get deposited on the substrate to form a thin film. The estimated film growth rate is given by the following relationship:

$$\text{Growth Rate (cm/s)}= \frac{\rho_d \langle x_{th} \rangle}{d\rho(1+\xi)E} \tag{2.1.1}$$

where ρ_d , $\langle x_{th} \rangle$, d , ρ , ξ , and E are the discharge power density in W/cm^2, average distance travelled by sputtered atoms before they come to thermal equilibrium, distance between target and substrate, atomic density in atoms/cm^3, Townsend secondary electron emission coefficient, and average sputtering energy of the order of keV, respectively.

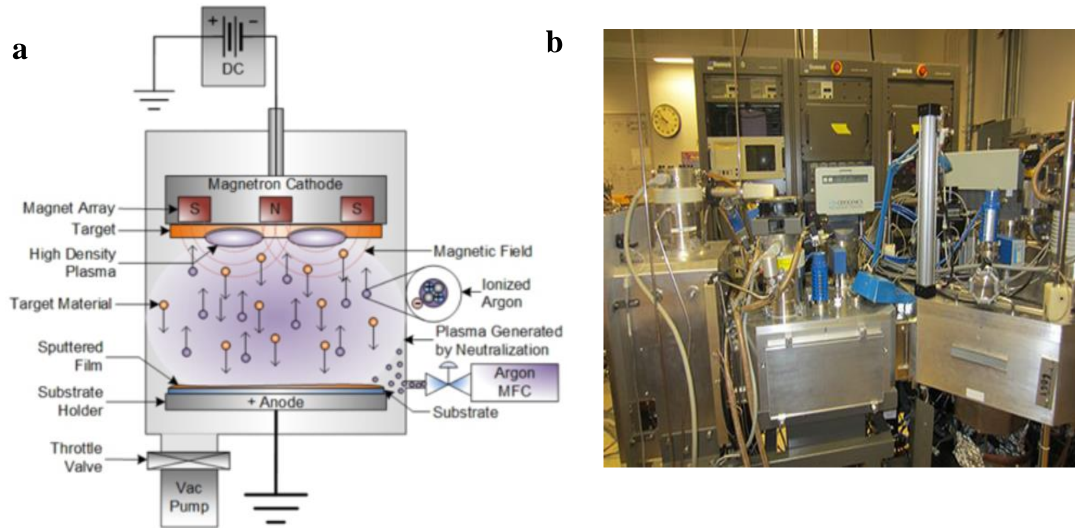

Figure 2.1.1 (a) Schematic diagram showing dc magnetron sputtering technique adapted from Ref. [105]. *(b) A photograph of Shamrock sputtering system in Prof. Jian-Ping Wang's lab.*

The magnetic field can control the motion of moving charged particles. In DC sputtering, applied magnetic field increases orbital motion of the electrons, which increases possiblity of collision between electron and inert atoms. This enhances the deposition rate at low pressure (~ few mTorr) of the working gas. The magnetic field can be applied by placing magnets behind the target as shown in Figure 2.1.1 (a). In our lab Shamrock sputtering system uses DC magnetron sputtering technique to grow high quality thin films. However, DC sputtering technique doesn't work to sputter insulators. In order to sputter insulators ac power supply is used, which can reduce the impedance of the insulators at high frequency. Figure 2.1.1 (b) shows Shamrock sputtering system, which contains five metal targets and one insulator target. The base pressure of the chamber is 5.0×10^{-8} Torr.

2.1.2 Atomic force microscopy (AFM)

Imaging of a thin film surface is carried out by using a sharp tip mounted at the end of a cantilever. In non-contact mode of AFM, the separation between the tip and surface atoms is tens

to a hundred angstroms. Because of vander Walls force, tip and the atoms are weakly attracted. The cantilever is vibrated with frequency on the order of few hundreds of kHz and any changes in this vibration due to the attractive force between surface atom and tip is detected. In the contact mode the tip and surface atoms come to the contact as a result a repulsive electrostatic force comes into play between tip and surface atoms. For the detection, the deflection of the tip is monitored and it is converted into electrical signal.

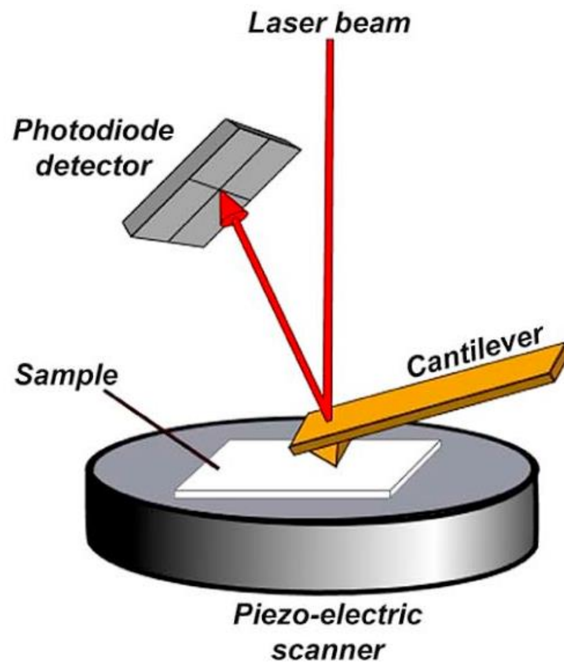

Figure 2.1.2 Schematic diagram of AFM adapted from Ref. [106] *doi:10.1016/j.trac.2016.03.014.*

2.2 Transmission electron microscopy (TEM)

Electrons can be used to image microstructure of thin films. Thermoinically generated electrons are accelerated by a potential of few hundreds of eV to MeV. Accelerated electrons can transmit through thin films due to their small wavelength. The wavelength can be estimated by using the de-Broglie equation,

$$\lambda = \frac{h}{(2meV)^{1/2}} \tag{2.1.2}$$

where h, m, e, and V are Planck's constant, the mass of an electron, charge of an electron, and accelerating potential, respectively. The electrons are elastically scattered at ion cores yielding diffraction patterns, and are inelastically scattered at grain boundaries and defects yielding a spatial variation of the transmitted beam. There are two modes of operation of the TEM, Dark field (DF) and Bright Field (BF). In DF mode of TEM operation, all the diffracted beams are allowed to transmit whereas in BF only the central beam is allowed to pass through, but all other diffracted beams are blocked. TEM not only does the imaging of the microstructure but also can estimate lattice constants and gives information of the crystal structure.

2.2.1 X-ray photo-electron spectroscopy (XPS)

The x-rays are incident on a material eject electrons from different bands which depends upon incident energy of the x-rays. The x-ray source used in our experiment was Al Kα .The kinetic energy of ejected electrons can be analyzed to investigate elements and their stoichiometry in the material. Furthermore, spin-orbit coupling of different bands of elements can also be estimated by XPS.

2.2.2 Raman spectroscopy

Raman spectroscopy uses laser light to identify stoichiometry, crystal structure of the material, and also gives information on thickness of thin films. The incident laser light vibrates molecules of sample as a result wavelength of the reflected laser light gets changed. The shift in the energy gives information of the modes of vibration, which can be analyzed to identify stoichiometry of the sample.

2.3 Device fabrication

2.3.1 Optical lithography

In order to print features into the films using the photomask a light sensitive chemical known as the photoresist was coated on the film by spinning at 4000 rpm for 30 s. In order to remove moisture from the film a soft-bake was done at 100 ˚C for 60 s. Then ultraviolet light was exposed for short time (~ 5 s) to break the bonds between carbon and hydrogen present in the photoresist so that exposed photoresist can easily dissolve in alkaline solution. The exposure was done using aligner MA6. Then the photoresist development was done by immersing the ultraviolet light exposed film in the alkaline solution for approximately 30 s followed by deionized water for approximately 60 s. In this way, photoresist is present only in the desired areas of the film or in another word features are transferred from photomask to the film.

2.3.2 Ion mill

The unwanted portion of the film was removed by exposing energetic Ar ions into the film while patterning films into devices. Ion mill can etch both insulators as well as conductors. The principle of ion mill is same as the sputtering in which the film to be etched is connected to the negative potential of the DC power supply.

2.3.3 CHA e-beam evaporator

For most part of the electrical contacts, I used e-beam evaporator to deposit thin Ti layer followed by thick Au layer. In an e-beam evaporator, W filament is used to produce electrons thermally and the electron beam is directed in to the source placed in a crucible by electric and magnetic fields. E-beam heats the source and when temperature of the source reaches above its boiling point then the evaporation of source occurs.

2.4 Process flow for fabrication of Hall bar and ST-FMR devices

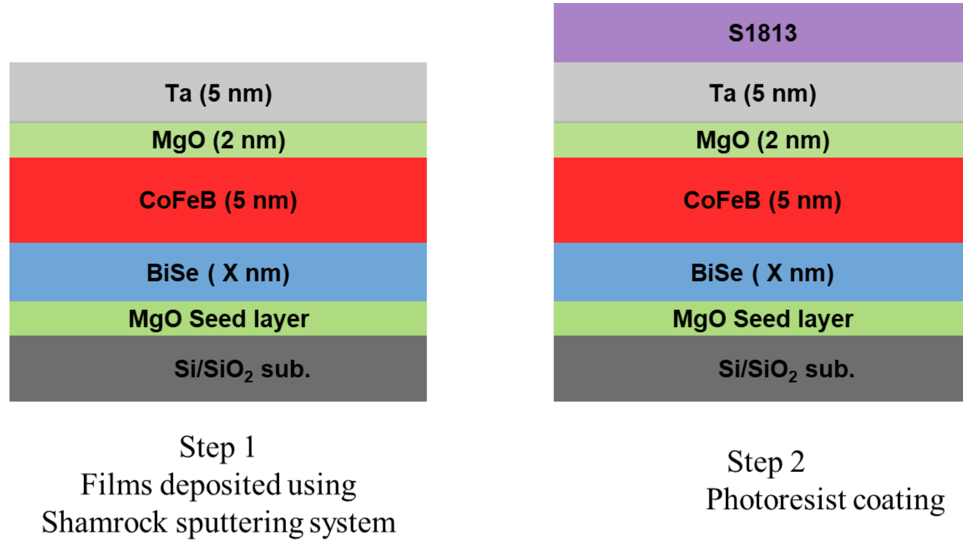

Step 1
Films deposited using
Shamrock sputtering system

Step 2
Photoresist coating

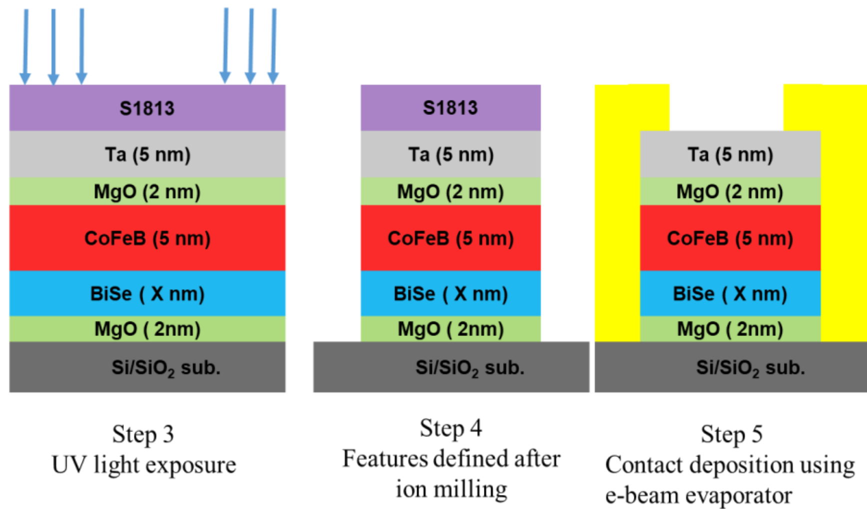

Step 3
UV light exposure

Step 4
Features defined after
ion milling

Step 5
Contact deposition using
e-beam evaporator

2.5 Process flow for spin-pumping device fabrication

Steps 1-4 are same for all the device fabrication.

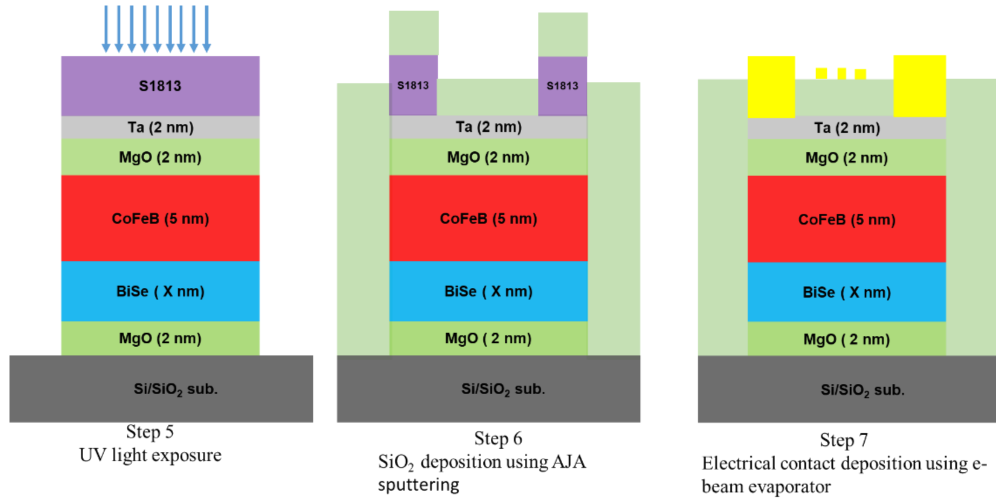

Step 5
UV light exposure

Step 6
SiO_2 deposition using AJA sputtering

Step 7
Electrical contact deposition using e-beam evaporator

2.6 SOT measurement set up for different types of measurement techniques

2.6.1 DC planar Hall measurement set up

Schematic block diagram of the dc planar Hall measurement set up is presented in Figure 2.6.1. The chip containing Hall cross-bar devices was mounted on a rotating stage of the physical property measurement system (PPMS). DC current was supplied by Keithley 2400 current source (K2400) and Hall voltage was measured by Keithley's nanovoltmeter 2182 (K2182). The data were collected by the lab view program.

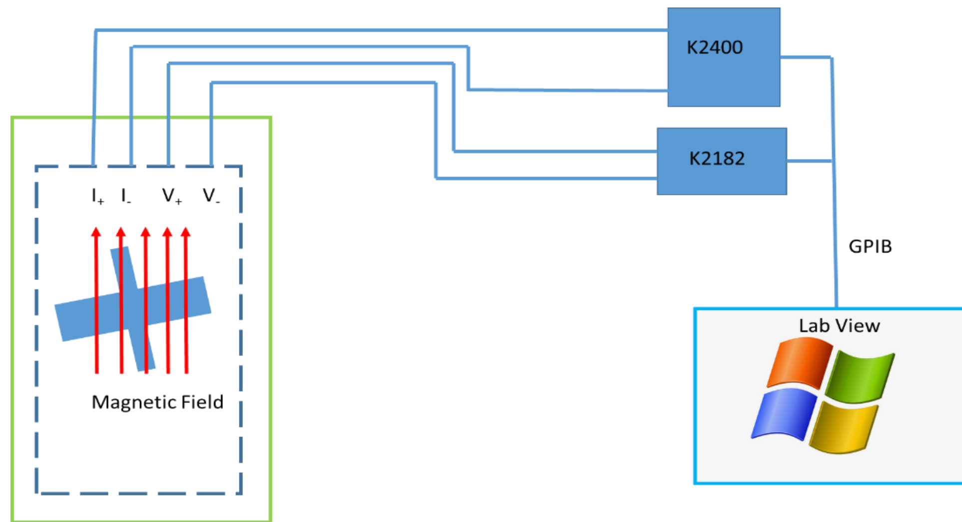

Figure 2.6.1 Schematic block diagram of showing dc planar Hall measurement for the characterization of SOT.

2.6.2 Second harmonic Hall measurement set up

Schematic diagram of the second harmonic Hall measurement set up is shown in Figure 2.6.2. The chip containing Hall cross-bar devices was mounted on a rotating stage of the physical property measurement system. Low frequency ac current was supplied by Keithley's 6221 current source (K6221) and first and second harmonic Hall voltages were measured by lock-ins SR830 (LIA1ω) and EG7221 (LIA2ω), respectively. The data were collected by the lab view program.

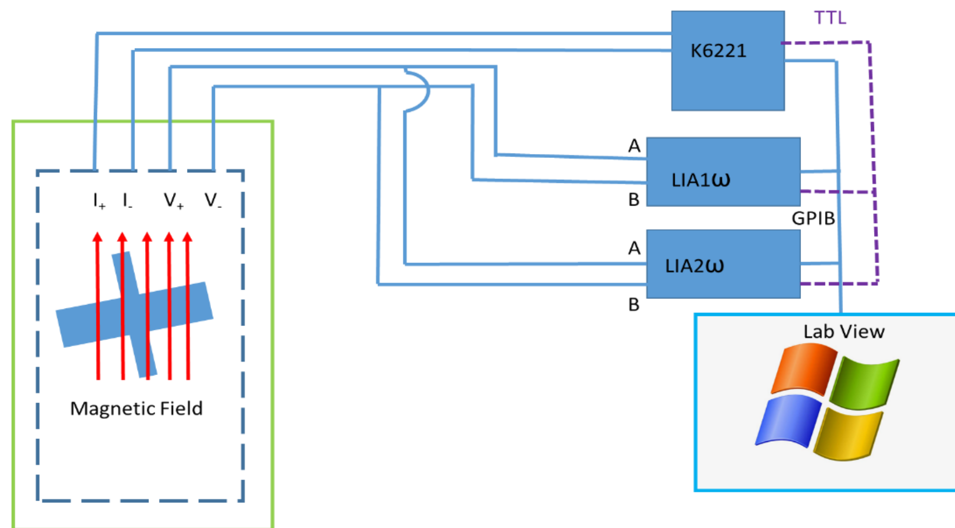

Figure 2.6.2 Shows schematic block-diagram of the SHH measurement set up.

2.6.3 ST-FMR measurement set up

Schematic of ST-FMR measurement setup is presented in Figure 2.6.3. The in-plane static magnetic field was generated by GMW 3D magnet whereas rf current was generated by the signal generator (SG). This source can generate up to 20 GHz and 4. 0 V rf excitation frequency and excitation amplitude, respectively. The rf current was supplied by the GSG probe into the device. Keithley 2182 nano-voltmeter was used to measure mixing voltage as a function of static in-plane magnetic field at different rf frequencies. The data were collected with the help of lab view program.

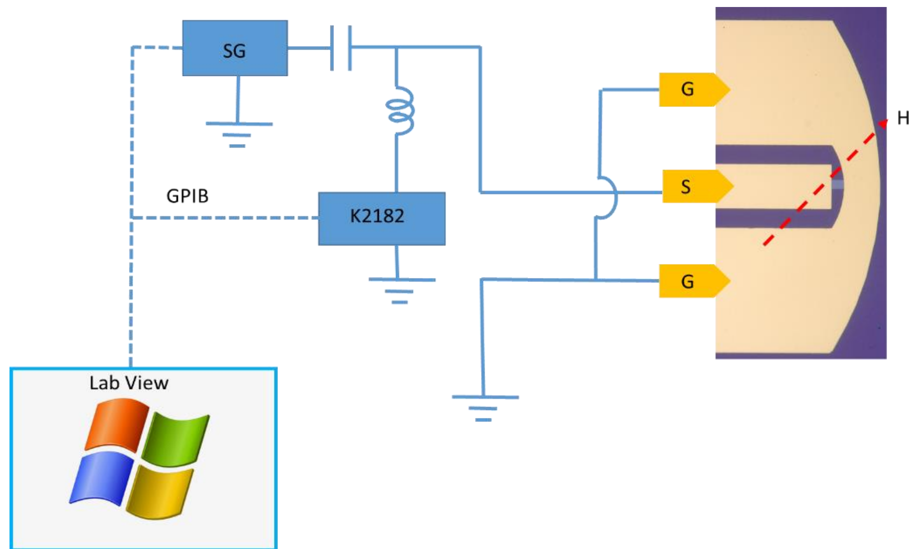

Figure 2.6.3 Schematic block diagram of ST-FMR measurement and optical image of the ST-FMR device. G and S stands for ground and signal, respectively.

2.6.4 Spin-pumping measurement setup

Schematic of spin-pumping measurement setup is presented in Figure 2.6.4. The in-plane static magnetic field is generated by GMW 3D magnet whereas rf field for the magnetization precession was generated by rf current flowing through the shortend coplanar wave guide as shown in Figure 2.6.4. The rf current was delivered by the co-axial cable and GSG probe into the wave guide. K2182 nano-voltmeter was used to measure spin-pumping voltage as a function of static in-plane magnetic field at different rf frequencies. The data were collected with the help of lab view program.

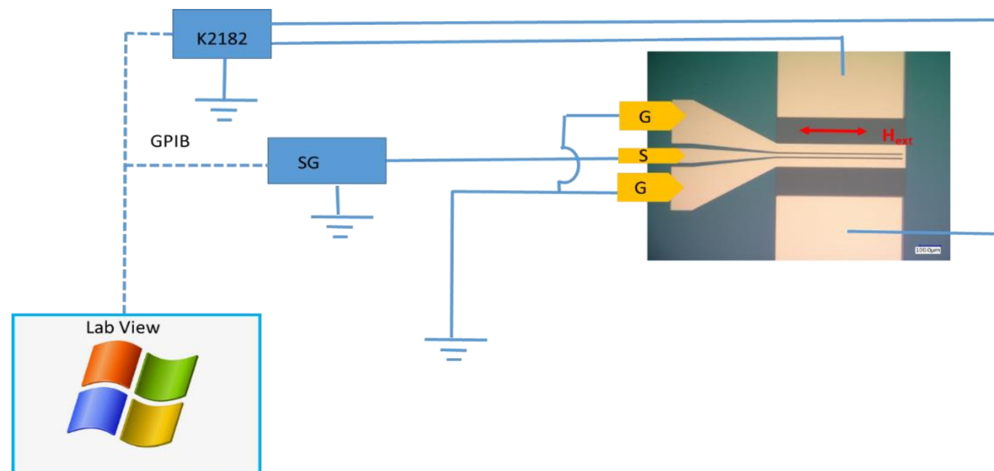

Figure 2.6.4 Spin-pumping measurement setup block diagram and optical image of the spin-pumping device. G and S stands for ground and signal, respectively.

Chapter 3. Room temperature high spin-orbit torque due to quantum confinement in sputtered $Bi_xSe_{(1-x)}$ films

This chapter has been reproduced from the manuscript, "Room temperature high spin-orbit torque due to quantum confinement in sputtered $Bi_xSe_{(1-x)}$ films" by Mahendra DC, Roberto Grassi, Jun-Yang Chen , Mahdi Jamali, Danielle Reifsnyder Hickey, Delin Zhang, Zhengyang Zhao, Hongshi Li, P. Quarterman, Yang Lv, Mo Li, Aurelien Manchon, K. Andre Mkhoyan, Tony Low, and Jian-Ping Wang, which was published in Nature Materials **17, 800-808(2018).*

3.1 Growth and characterization of bismuth selenide thin films

Bismuth selenide (BS) thin films for the characterization of SOT were grown on Si/SiO_2 substrates at room temperature by sputtering a composite Bi_2Se_3 (99.99% pure) target in our ultra-high vacuum (UHV) six-target Shamrock sputtering system with a base pressure of 5.0×10^{-8} Torr. Bi_2Se_3 is sputtered at 50 W dc power and at 3 mTorr Ar pressure yielding a deposition rate of 0.7 Å/s. The MgO layer is rf sputtered at a deposition rate of 0.07 Å/s whereas all of the metallic layers (Ta, CoFeB, and Gd) are dc sputtered at an Ar pressure 3 mTorr. BS films with thickness of 4, 6, 8, 10, 12, 16, 20, 40, and 50 nm were deposited onto a Si/SiO_2 substrate using a 2 nm-thick MgO layer as an adhesion layer and capped by 5 nm of MgO for the σ_c measurement. σ_c as a function of BS film thickness as shown in Figure 3.1.1 (a). The Hall resistance presented in Figure 3.1.1 (b) indicates that the majority of the carriers in the BS films are electrons. The 3D carrier concentrations of the 4, 16, and 40 nm thick BS films were found to be 1.6, 1.2, and $1.0\times10^{21}/cm^3$, respectively. The results of the temperature dependent σ_c measurement of the 16 and 40 nm BS film is presented in Figure 3.1.1 (c). σ_c decreases with the decrease in temperature, which indicates that the BS films are semiconductors.

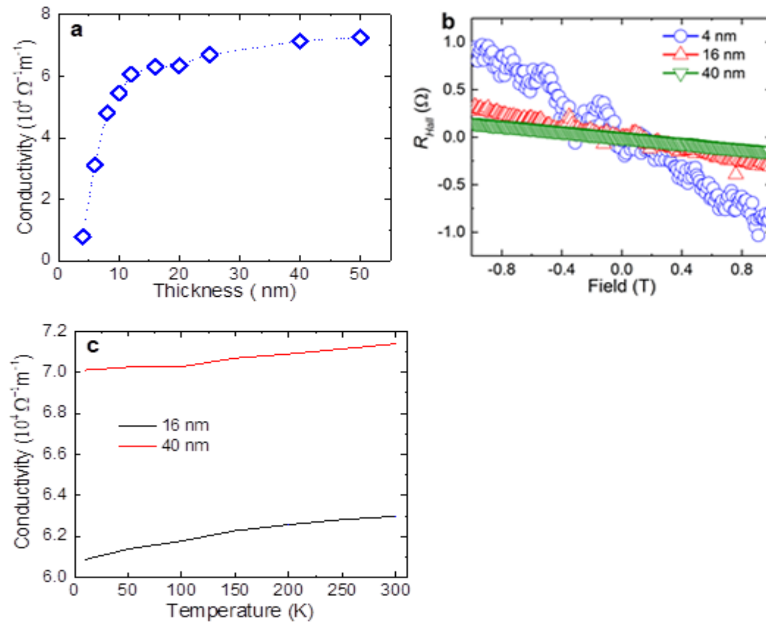

Figure 3.1.1 The electrical conductivity, Hall measurement, temperature dependent σ of bismuth selenide films. (a) The thickness-dependent electrical σ_c of the BS films. (b) The Hall measurement of 4, 16, and 40 nm BS films at room temperature to determine carrier concentration. (c) Temperature dependent σ_c of 16 and 40 nm BS films.

In order to characterize the SOT arising from the BS films, thin films with the multilayer structure Si/SiO_2/MgO (2 nm)/BS (t_{BS} nm)/CoFeB (5 nm)/MgO (2 nm)/Ta (5 nm) are prepared, with t_{BS} = 4, 8,16, and 40 nm as shown in the schematic drawing in Fig. 2a. Unless otherwise stated, we will use the labeling BS4, BS8, BS16, BS40 for the samples with t_{BS} = 4, 8, 16, 40 nm, respectively. The thin-film samples are cross-sectioned using an FEI Quanta 200 3D dual-beam focused ion beam (FIB) and then analyzed using bright field scanning transmission electron microscopy (BF-STEM) and high-angle annular dark-field STEM (HAADF-STEM). HAADF-STEM images are fast Fourier transform filtered to the instrumental resolution of ~0.8 Å. The HAADF-STEM images of samples BS4 and BS8, respectively presented in Figure 3.1.2 (a) and (b), respectively show that BS has a polycrystalline structure and that the atomic layers of Bi and

Se are continuous in both samples. Additionally, the average grain orientation in sample BS4 is 2° with a standard deviation of 9° (from vertical c-orientation), which is almost identical to the average grain orientation in sample BS8 (2° with a standard deviation of 8°). The average size of grains in sample BS4 is approximately 6 nm wide and 4 nm high, whereas that of grains in sample BS8 is approximately 18 nm wide and 8 nm high.

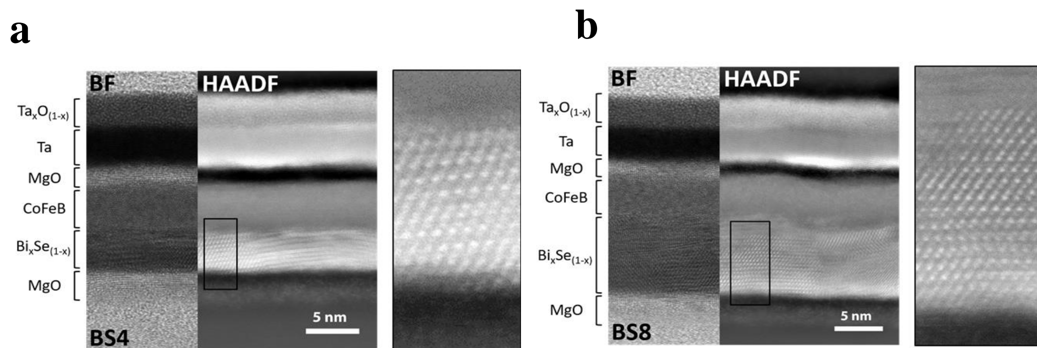

Figure 3.1.2 STEM characterization. (a) and (b) Composites of simultaneously acquired BF- and HAADF-STEM images of samples BS4 and BS8, respectively. The selected region of the HAADF-STEM image indicated by a black line is magnified at right to show the BS atomic detail.

Energy-dispersive X-ray spectroscopy (EDX) data is collected using a Super-X quad-SDD windowless in-pole piece EDX detector. EDX line scans are analyzed using Bruker Esprit software. The energy dispersive X-ray spectroscopy (EDS) line scan shows that stoichiometric Bi_2Se_3 exists at the top of the BS films; however, there is a gradient of the Bi concentration from the top to the bottom of the films as shown in Figure 3.1.3 (d) and (e). The average value of x in a BS film is 0.47 with ± 3% uncertainty, determined by Rutherford back-scattering spectroscopy (RBS).

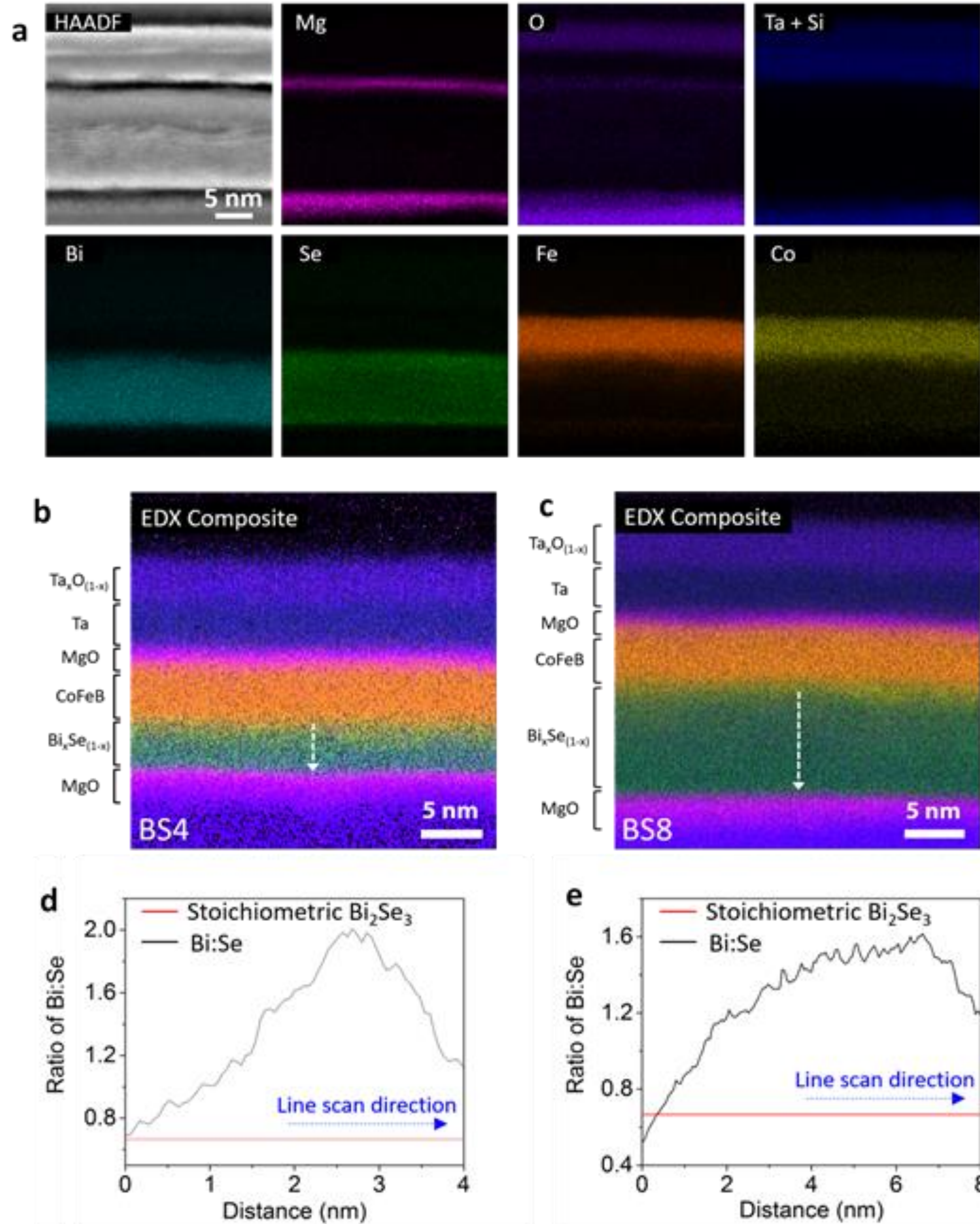

Figure 3.1.3 EDX maps and Bi:Se composition line scans for samples BS4 and BS8. (a) HAADF-STEM image and individual-element EDX maps for sample BS8 (Ta+Si map indicates the combined Ta and Si signal due to peak overlap). EDX maps in (a) are normalized for visibility. (b) and (c) EDX composite maps for samples BS4 and BS8, respectively, scaled for atomic percent of each element. Arrows represent direction of composition line scans plotted in (d) and (e). (d) and

(e) EDX line scan data for Bi:Se composition for samples BS4 and BS8, respectively (line scan data corresponds to white arrows in (b) and (c)). The line scans show that at the top surface of the BS layer, the stoichiometric ratio is Bi_2Se_3, but that the layers become Bi rich below the top surface, with the Bi concentration peaking several nm into the layer and then decreasing toward the layer's bottom edge (consistent for both the BS4 and BS8 samples).

Figure 3.1.4 (a) shows the AFM images of an Si/SiO_2/MgO (2 nm)/BS (4 nm) film. The root mean square (RMS) value of the surface roughness of the 4 nm BS film is 0.5 nm. Furthermore, we probed surface roughness propagation in the full stack, as shown in Figure 3.1.4 (b). The RMS value of 0.38 nm for the surface roughness in sample BS4 confirms the smoothness of the full stack, which is necessary for future device fabrication on a wafer level.

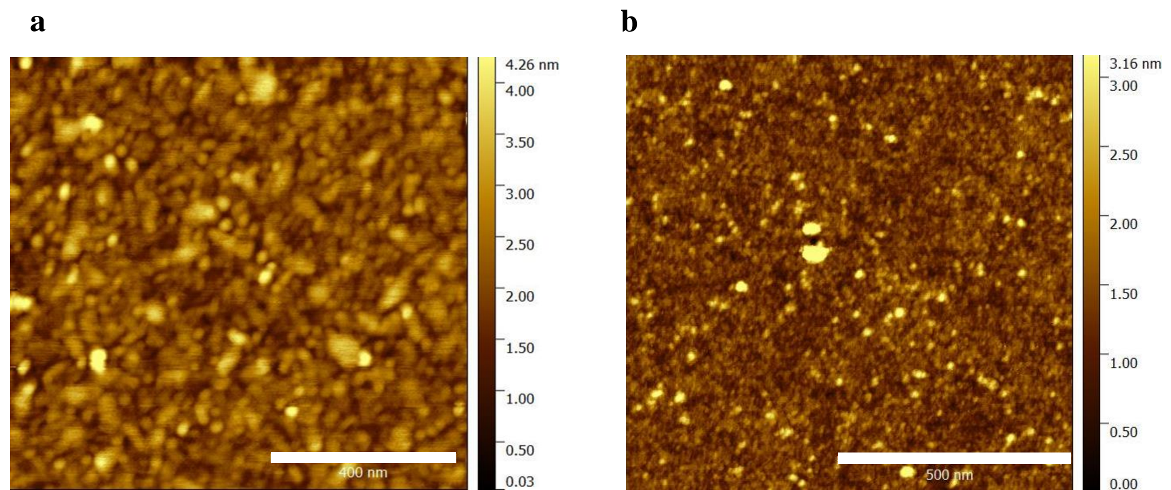

Figure 3.1.4 The AFM images of the (a) 4 nm BS film and (b) BS4 sample, respectively.

3.2 SOT characterization using dc planar Hall

The multilayer thin films with in-plane magnetization are patterned into Hall-cross bars with dimensions 5-30 μm wide and 70 μm long, and dc planar Hall measurement is performed on the Hall-cross bar with dimensions 10 μm × 70 μm, as shown in Figure 3.2.1 (b). The bipolar input current of magnitude up to 8.5 mA is injected along the *x*-direction, and the angle-dependent Hall resistance ($R_H(I,\alpha)$, where *I* is input current and α is angle between current flow direction and external field) is measured under the application of a constant 5000 Oe in-plane magnetic field while rotating the sample in the *xy* plane from -7 to 365°. The in-plane SOT or ADLT exerted by the accumulated spin-density on the interface of the BS/CoFeB as shown in Figure 3.2.1 (a) is obtained by using the Slonczewski's equation [107], $\tau_{\parallel} = \frac{\hbar J_s}{2eM_s t_{FM}}(\hat{m}\times(\hat{\sigma}\times\hat{m}))$, where $\hbar$ is the reduced Planck's constant, J_s is the effective spin-polarized current density, e is an electronic charge, M_s is the saturation magnetization, t_{FM} is the thickness of the FM layer, $\hat{m}$ is the magnetization unit vector, and $\hat{\sigma}$ is the unit vector of the current induced spin-polarization on the interface. The effective out-of-plane magnetic field associated with the in-plane torque ($\tau_{\parallel}$) is given by [2] $H_{OOP} = \frac{\hbar J_s}{2eM_s t_{FM}}(\hat{\sigma}\times\hat{m})$. In addition to the $\tau_{\parallel}$, there is also an out-of-plane component of SOT or FLT due to the spin-density at the interface, which is given by $\tau_{\perp} \propto (\hat{\sigma}\times\hat{m})$. The in-plane magnetic field associated with the out-of-plane torque ($\tau_{\perp}$) is given by $H_T \propto \hat{\sigma}$. Furthermore, there is also $\tau_{\perp}$ due to the Oersted field (H_{Oe}) generated by charge current flow in the NM layer. Figure 3.2.1 (c) shows $R_H(I,\alpha)$ for the sample BS4 at ± 8.5 mA. In principle, $R_H(I,\alpha)$ consists of the planar Hall resistance (R_{PHE}) and the anomalous Hall resistance (R_{AHE}) due to the planar and anomalous Hall effects, respectively. The R_{PHE} is due to the combined effects of the external field, current-induced effective fields, and the anisotropy field acting on the magnetization ($R_{PHE} \propto \sin(2\beta)$, where β is the angle between the magnetization and current flow direction). R_{AHE}

is due to the pulling of the magnetization in the out-of-plane direction by a current-induced effective field ($R_{AHE} \propto M_z$, where M_z is the z-component of magnetization).

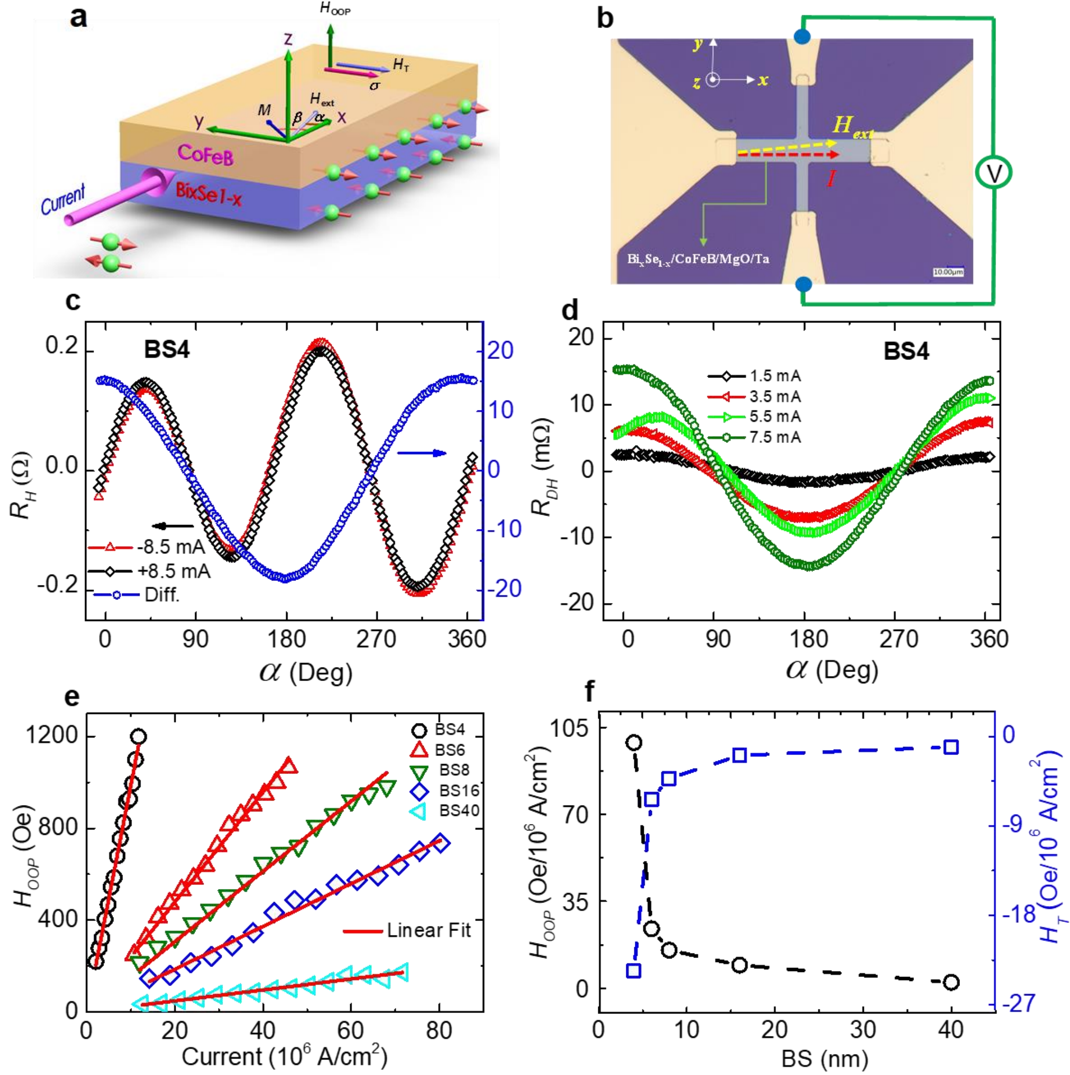

Figure 3.2.1 Schematic diagram, experimental set up, angle-dependent Hall resistance measurements, and characterization of SOT. (a) A three-dimensional schematic diagram demonstrating the SOT in a BS/CoFeB heterostructure. H_{ext} and M represent an in-plane externally applied magnetic field and the in-plane magnetization, respectively. H_T and H_{OOP} are the current-induced transverse and out-of-plane magnetic fields, respectively. The red arrows represent the direction of spin-magnetic moment. (b) An optical micrograph of the fabricated Hall-cross bar with

schematic drawings of the Hall measurement set up. (c) The $R_H(I,\alpha)$ *of sample BS4 at ± 8.5 mA input current on the left axis and* $R_{DH}(I,\alpha)$ *on the right axis at RT under a constant 5000 Oe in-plane magnetic field. (d) The* $R_{DH}(I,\alpha)$ *at different input currents for the BS4 sample. (e) The variation of* H_{OOP} *with the current density. (f) The variation of* H_{OOP} *(left axis) and* H_T *(right axis) as a function of BS thickness.*

The difference in Hall resistance as a function of input current and magnetization angle is given by,

$$R_{DH}(I,\beta) = R_{PHE}(I,\beta) - R_{PHE}(-I,\beta) + R_{AHE}(I,\beta) - R_{AHE}(-I,\beta) + C \qquad (3.2.1)$$

where C is resistance offset. Following Kawaguchi et al [54]., $R_{AHE}(I,\beta) - R_{AHE}(-I,\beta) \simeq 2\frac{dR_{AHE}}{dH} H_{OOP}\cos\alpha$ and $R_{PHE}(I,\beta) = R_{PHE}\sin 2\beta$. From Figure 3.2.1 (a) the total x- and y-components of the magnetic field are $H_{Total,x} = H_{Total}\cos\beta = H_{ext}\cos\alpha$ and $H_{Total,y} = H_{Total}\sin\beta = H_{ext}\sin\alpha \pm (H_T + H_{Oe})$; dividing the y-component of the total magnetic field by the x-component, we get $\beta = \tan^{-1}\left(\frac{H_{ext}\sin\alpha \pm (H_T + H_{Oe})}{H_{ext}\cos\alpha}\right)$, where + for positive input current and – for negative input current. Substituting all the values in Eqn.(3.2.1) the difference in Hall resistance as a function of magnetic field angle is given by,

$$R_{DH}(I,\alpha) = R_{PHE}\sin(2\tan^{-1}\left(\frac{H_{ext}\sin\alpha + (H_T + H_{Oe})}{H_{ext}\cos\alpha}\right) - R_{PHE}\sin(2\tan^{-1}\left(\frac{H_{ext}\sin\alpha - (H_T + H_{Oe})}{H_{ext}\cos\alpha}\right)) + 2\frac{dR_{AHE}}{dH} H_{OOP}\cos\alpha + C$$

$$= 2R_{PHE}\frac{\left[2\left(\frac{(H_T + H_{Oe})}{H_{ext}}\right)^3\cos\alpha + \frac{(H_T + H_{Oe})}{H_{ext}}\cos\alpha + \frac{(H_T + H_{Oe})}{H_{ext}}\cos 3\alpha\right]}{\left[\left(\frac{(H_T + H_{Oe})}{H_{ext}}\right)^4 + \left(\frac{(H_T + H_{Oe})}{H_{ext}}\right)^2\cos\alpha + 1\right]} + 2\frac{dR_{AHE}}{dH} H_{OOP}\cos\alpha + C$$

where C is the resistance offset. At $\frac{(H_T + H_{Oe})}{H_{ext}} << 1$ approximation

$$R_{DH}(I,\alpha) = 2R_{PHE}\frac{(H_T + H_{Oe})}{H_{ext}}(\cos\alpha + \cos 3\alpha) + 2\frac{dR_{AHE}}{dH}H_{OOP}\cos\alpha + C \quad (3.2.2)$$

The current-induced effective fields H_T and H_{OOP} can be extracted using Eqn. (3.2.2) by characterizing $R_H(I,\alpha)$ for positive and negative input currents.

Figure 3.2.1 (d) shows $R_{DH}(I,\alpha)$ versus an externally applied field angle for the sample BS4 at different input currents. The $R_{DH}(I,\alpha)$ increases with increase in input current and has a maximum located at approximately 180°. $\frac{dR_{AHE}}{dH}$ is obtained by sweeping the out-of-plane field at a small 1 mA input current. R_{AHE} is measured by rotating the sample in the *xz* plane under constant 5000 Oe field, which is the same in-plane field used for dc planar Hall measurement as shown in Figure 3.2.2. At 90° and 270° the external field is parallel to the magnetization. The R_{AHE} is plotted against z-component of the magnetic field close to 90° as shown in Figure 3.2.2 (b). After considering current shunting and short circuit effects [108], $\frac{dR_{AHE}}{dH}$ is determined to be 6.75, 7.33, 7.37, 7.55, and 6.51 × 10-4 Ω/Oe for samples BS4-BS40, respectively. The H_{Oe} is estimated by using Ampere's law after knowing the charge current in NM layer using one dimensional current shunting Eqn. (3.3.1). The R_{PHE} is obtained by fitting $R_H(I,\alpha)$ data to the Eqn. $R_0 + R_{AHE}\cos(\alpha) + R_{PHE}\sin(2\alpha)$, where R_0 is resistance offset. After determining R_{PHE}, $\frac{dR_{AHE}}{dH}$, and H_{Oe} values, H_{OOP} and H_T can be determined by curve fitting of the $R_{DH}(I,\alpha)$ experimental data to Eqn. (3.2.2). The H_{OOP} versus the current density is presented in Figure 3.2.1 (e). The $\frac{H_{OOP}}{J_{BS}}$ determined by the linear fit is as large as (98.83 ± 0.7) Oe per 106 A/cm^2 for sample BS4, where J_{BS} is the current density in the BS layer (the uncertainty is the standard error from the linear fit).

The spin torque efficiency $\theta_S = \frac{2eM_s t_{FM}}{\hbar}\frac{H_{OOP}}{J_{BS}}$ of sample BS4 is determined to be 18.62 ± 0.13. The $\frac{H_{OOP}}{J_{BS}}$ values for samples BS6-BS40 are (23.96 ± 0.19), (15.32 ± 0.16), (9.32 ± 0.11), and (2.39 ± 0.05) Oe per 106 A/cm^2, respectively. The θ_S for samples BS6-BS40 are determined to be 4.50 ± 0.03, 2.88 ± 0.03, 1.75 ± 0.02, 0.45 ± 0.01, respectively. The σ_S is determined to be as large as $1.45 \pm 0.01 \times 105 \frac{\hbar}{2e} \Omega^{-1}m^{-1}$ for sample BS4. The BS films have both σ_c and σ_S values comparable to those from previous reports on TIs [65,66,87,109]. A summary of σ_c, θ_S, σ_S for our samples and the best previously reported TIs and HMs are presented in Table 1.

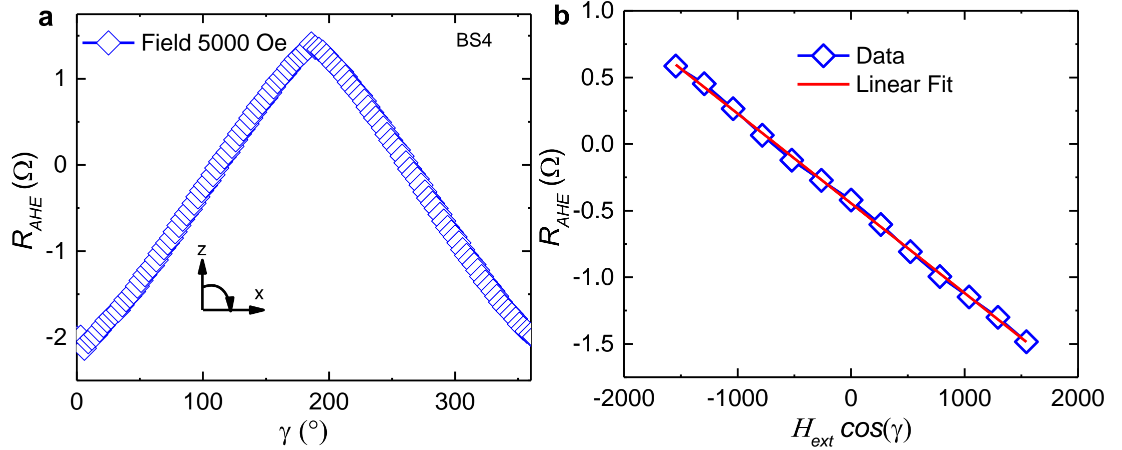

Figure 3.2.2 Estimation of $\frac{dR_{AHE}}{dH}$ of sample BS4 (a) R_{AHE} as a function of rotation angle (γ) in the xz plane. (b) R_{AHE} as a function of external field when the magnetization is close to in-plane.

The $\tau_\perp$ is absent at large in-plane fields; however, it is sizeable at smaller fields. Figure 1.2.1 (a) shows the Hall resistance for ± 4 mA at a 200 Oe in-plane field for sample BS4. The 200 Oe in-plane field is sufficient to saturate the magnetization along the in-plane direction. The left and right axes correspond to the $R_H(I,\alpha)$ and $R_{DH}(I,\alpha)$, respectively. The solid red line is fit to

Eqn. (3.2.2) by keeping H_T and H_{OOP} as the only fitting parameters. The R_{PHE} is $\sim -0.1479\,\Omega$, which is determined by fitting $R_H(I,\alpha)$ to the Eqn. $R_0 + R_{AHE}\cos(\alpha) + R_{PHE}\sin(2\alpha)$. H_T versus current density is plotted in Figure 3.2.3 (b), and as expected, it shows linear behavior. The $\frac{H_T}{J_{BS}}$ value obtained from the linear fit is (-23.60 ± 0.04) Oe per 10^6 A/cm^2 for sample BS4.

H_T for samples BS4-BS40 is presented in Figure 3.2.1 (f). The positive $\tau_\perp$ in sputtered BS indicates that the Rashba-Edelstein induced $\tau_\perp$ is absent, which is consistent with the previous reports on crystalline Bi_2Se_3 [65,110]. Experimentally, we observe that as the thickness of the BS film increases, the grain size also increases and the magnitude of the $\tau_\parallel$ and $\tau_\perp$ decreases (Figure 3.2.1 (f)). This gives a clear indication of the influence of grain size on the SOT in sputtered BS films.

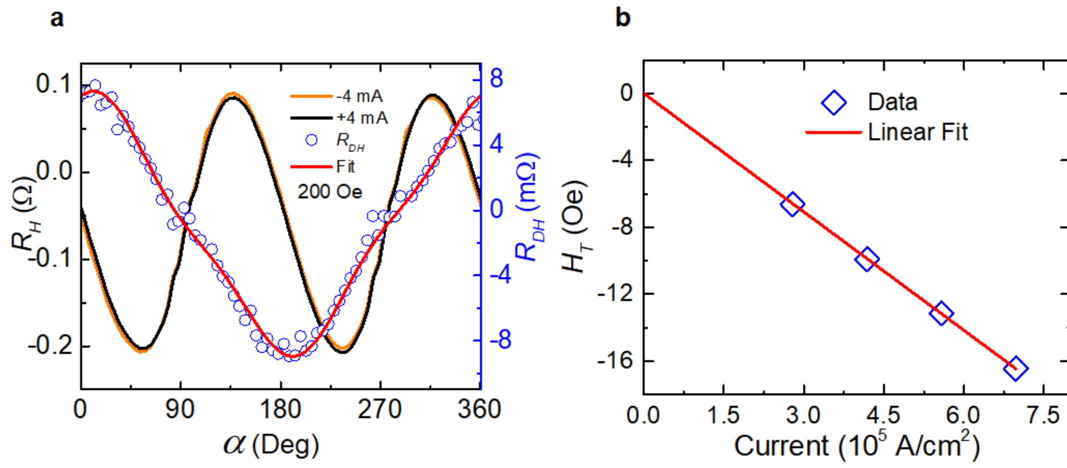

Figure 3.2.3 The characterization of FLT in sample BS4 (a) R_H and R_{DH} as a function of the field angle under a 200 Oe in-plane field. (b) The H_T is plotted against current density.

3.3 Estimation of J_{BS}

J_{BS} is determined by knowing the σ_c of each layer and using the one dimensional current shunting Eqn. (3.3.1). The one dimensional current shunting equation treats each layer in the stack as a resistor connected in parallel. The thickness-dependent σ_c of the BS films is presented in Figure 3.1.1 (a). σ_c of the Ta (5 nm) and CoFeB (5 nm) films are determined to be 5.0×10^5 and $7.2 \times 10^5\ \Omega^{-1}m^{-1}$, respectively. The capping layer is approximately 50% oxidized; as a result, there is a 50% decrease in its conductivity. We also incorporated current shunting through the capping layer in the θ_S characterization. The current shunting equation assuming homogenous current distribution through each layer is given by,

$$J_{BS} = \frac{I_{total}\sigma_{BS}}{W(\sigma_{BS}t_{BS} + \sigma_{BS}t_{BS} + \sigma_{Cap}t_{Cap})} \quad (3.3.1)$$

where σ and t are the conductivities and thicknesses of the layers, respectively; I_{total} is total input current in the device, and W is the width of the device.

3.4 SOT characterization of reference sample Ta by dc planar Hall

The dc planar Hall characterization of the reference Si/SiO2/Ta (5 nm)/CoFeB (5 nm)/MgO (2 nm)/ ta (5 nm) referred as Ta sample is presented in Figure 3.4.1. The $R_H(I,\alpha)$ and $R_{DH}(I,\alpha)$ of the Ta sample show the same trend as that of the BS samples, except for an opposite sign in $R_{DH}(I,\alpha)$. $\frac{dR_{AHE}}{dH}$ value for sample Ta is determined to be 9.00×10^{-4} Ω/Oe. H_{OOP} versus the current density in Ta (J_{Ta}) is plotted in Figure 3.4.1 (c). The $\frac{H_{OOP}}{J_{Ta}}$ value is determined to be (-0.76 ± 0.01) Oe (10^{-6})/(A/cm^2) for the Ta sample by using a linear fit. The $\frac{H_{OOP}}{J_{Ta}}$ from the BS samples is as large as two orders of magnitude greater than that of the Ta sample. The θ_S of the Ta

sample is determined to be -0.14 ± 0.01. The σ_S of the Ta sample is (-0.7 ± 0.05) × $10^5 \frac{\hbar}{2e} \Omega^{-1}m^{-1}$.

The $\frac{H_{OOP}}{J_{Ta}}$, θ_S, and σ_S values of the control Ta sample are comparable to those from previous reports [2,49,54,55].

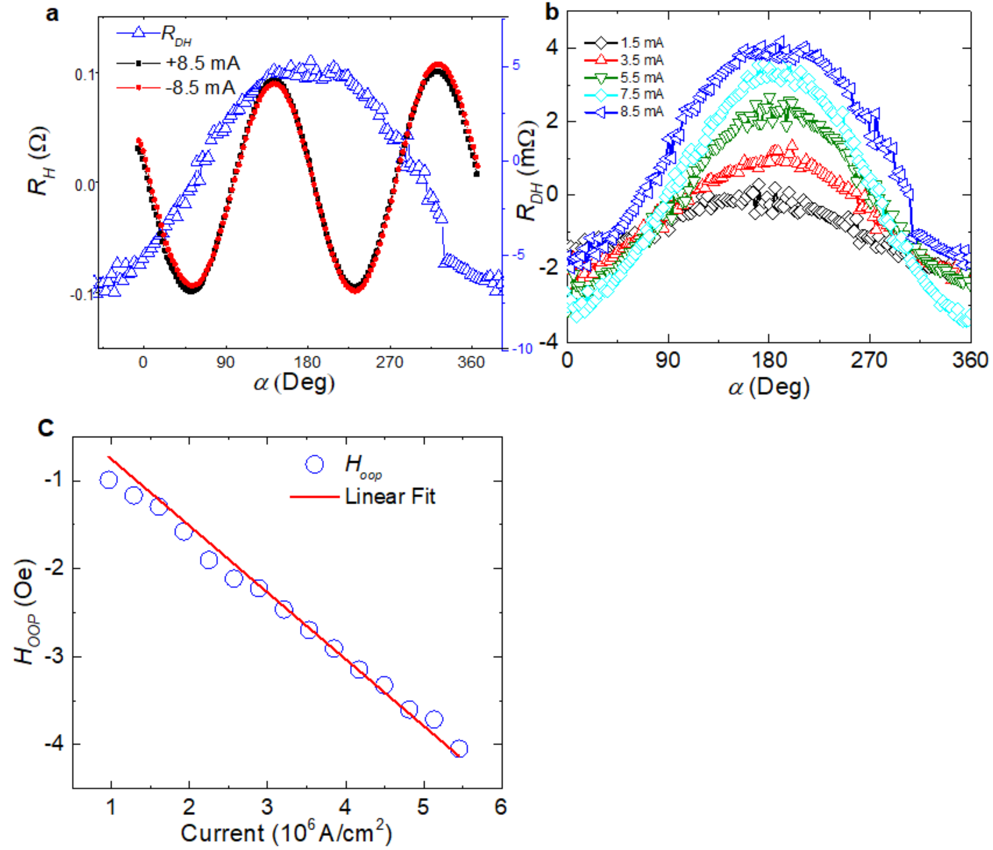

Figure 3.4.1 The angle-dependent Hall measurement for SOT characterization from the control sample. (a) The angle-dependent Hall resistance of the Ta sample at an input current of ± 8.5 mA on the left axis and difference in the Hall resistance on the right axis at room temperature under a constant 5000 Oe in-plane magnetic field. (b) The angle-dependent difference in the Hall

resistances at different bias currents for sample Ta. (c) The current-induced out-of-plane field as a function of the input current density for Ta sample.

3.5 Spin-torque characterization using ferromagnetic resonance (ST-FMR)

The ST-FMR measurement technique has been used to determine SOT in NM/FM bi-layers with an in-plane magnetic layer [45,46,65,67]. We performed ST-FMR measurements on Si/SiO_2/MgO (2 nm)/BS (4 and 16 nm)/CoFeB (5 nm)/MgO (2 nm)/Ta (1 nm) samples to confirm the high SOT from the sputtered BS films. A reference sample with the BS layer replaced by Ta (5 nm) is also prepared. The films are patterned into rectangular strips using optical lithography with dimensions 3-40 µm (wide) × 30 µm (long), and devices with dimensions 15 µm × 30 µm are used for the ST-FMR measurement. In the ST-FMR measurement, a constant radio frequency (rf) current is applied while sweeping the static in-plane magnetic field at 45° or -135° with the current as shown in Figure 3.5.1 (a). The rf current in the BS layer generates oscillating spin-density in the vertical direction and gets accumulated at the interface of the BS layer and CoFeB layer. Thus, accumulated oscillating spin-density exerts ADLT on the CoFeB layer. Additionally, out-of-plane FLT due to the H_T and H_{Oe} exert on the CoFeB layer. In our case, the torques due to H_T and H_{Oe} are in the same direction. As a consequence of the torques the CoFeB magnetization oscillates, which induces oscillating resistance due to the anisotropic magnetoresistance. The product of the injected rf current and oscillating resistance yields a mixing voltage (V_{mix}), as shown in Figure 3.5.1 (b). The symmetric part of the V_{mix} corresponds to the $\tau_{\parallel}$ and the anti-symmetric part of the V_{mix} corresponds to the $\tau_{\perp}$. The following relation can be used to obtain the θ_S [45]:

$$\theta_S = \frac{J_S}{J_{BS}} = \frac{S}{A}\frac{eM_s t_{FM} t_{BS}}{\hbar}\sqrt{1+\frac{M_{eff}}{H_0}} \quad (3.5.1)$$

where H_0 is the resonance field, M_{eff} is the effective magnetization, and S and A are the symmetric and anti-symmetric voltages, respectively. The values of S, A, and H_0 are obtained by fitting V_{mix} with symmetric and anti-symmetric Lorentzian functions given by,

$$V = \frac{S\Delta H^2}{\Delta H^2 + (H_{ext} - H_0)^2} + \frac{A(H_{ext} - H_0)}{\Delta H(\Delta H^2 + (H_{ext} - H_0)^2)} \quad (3.5.2)$$

where ΔH is the line-width which is also obtained by fitting. In the measurements, the excitation rf frequency 6-8.5 GHz is used with constant output power, 23.9 dBm. The M_{eff} is obtained by fitting the frequency versus H_0 using the Kittel formula, $f = \frac{\gamma}{2\pi}\sqrt{H_0(H_0 + 4\pi M_{eff})}$, where γ is the gyromagnetic ratio. The values of M_{eff} obtained from Kittel fitting are 1.74, 1.96, and 1.81×10^4 Oe for the samples with BS (4 nm), BS (16nm), and Ta (5nm), respectively. The symmetric voltage is dominant in sample BS (4 nm) as shown in Figure 3.5.1 (b) where as it is comparable in sample BS (16 nm) as shown in Figure 3.5.1 (e). In the case of the reference Ta sample, the anti-symmetric voltage is dominant (Figure 3.5.1 (f)). From the fitting, the θ_S values of the 4 and 16 nm BS films are determined to be as large as 8.67±1.0 and 1.56±0.01, respectively. The θ_S of reference sample Ta (5 nm) is determined to be ~ -0.065± 0.002. The error bars are the uncertainties present in the *S/A* from fitting. The θ_S values obtained from the ST-FMR measurement are similar to those determined by using the dc planar Hall measurement. Given the fact that the previous reports of the θ_S values of TIs show large variability [65,87,110,111], we emphasize that our θ_S values determined by the dc planar Hall and ST-FMR methods match. The θ_S versus excitation frequency plot of sample BS (4 nm) is presented in Figure 3.5.1 (c) and shows that there is no significant variation of θ_S with the excitation frequency, which indicates that there is negligible current shunting due to the parasitic impedance. The frequency versus linewidth presented in Figure 3.5.1 (d) shows a linear relationship between them. The damping constant (ξ) of the CoFeB layer can

be obtained by linear fitting of the relationship $\Delta H = \Delta_0 + \frac{4\pi}{\sqrt{3}\gamma}\xi f$, where Δ_0 is extrinsic linewidth contribution. From the linear fitting, the damping constant is determined to be 0.0048.

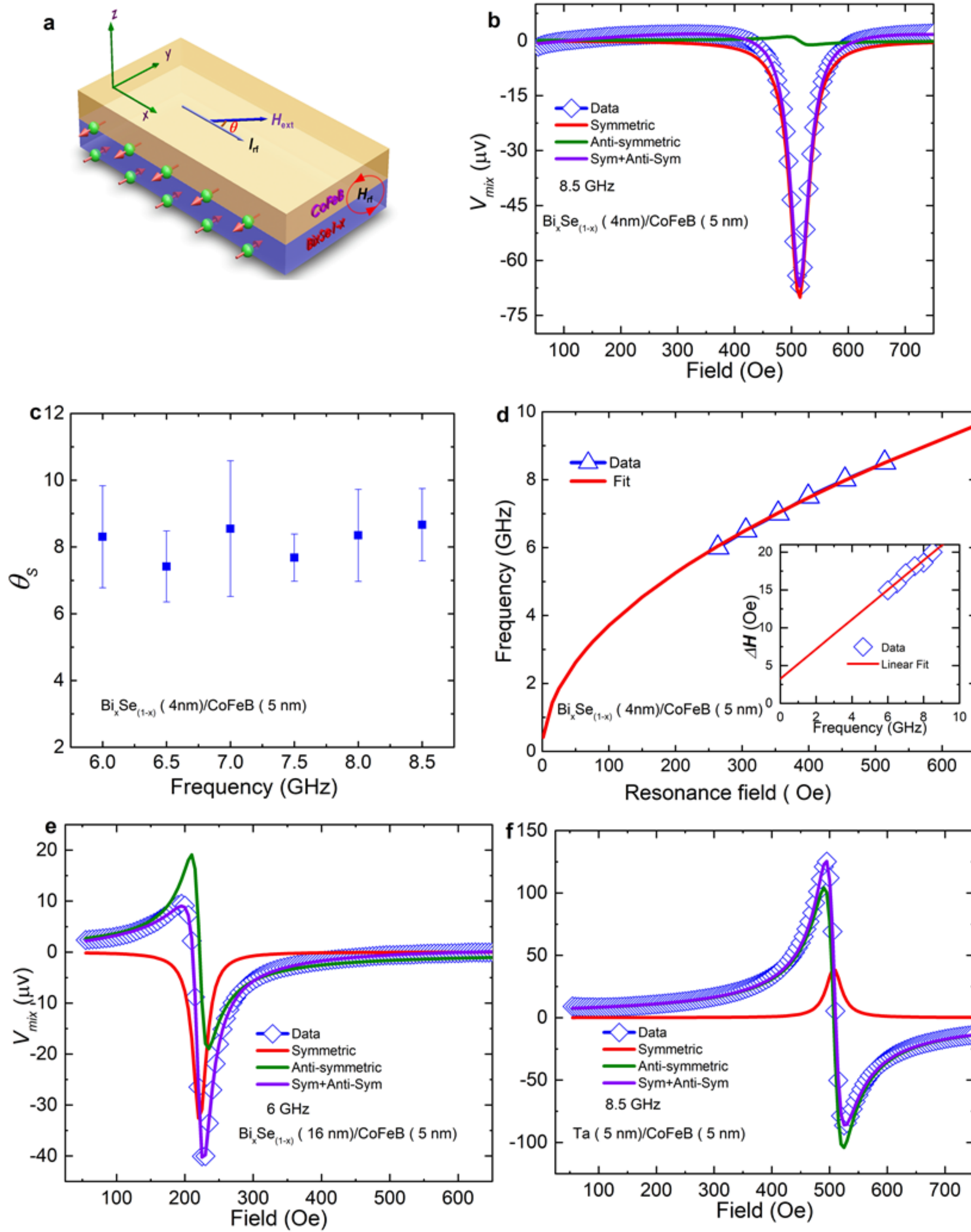

Figure 3.5.1 ST-FMR measurement for the characterization of SOT (a) Schematic diagram showing the stack structure and co-ordinate system. (b), (e), and (f) ST-FMR resonance line shape of samples BS 4 and 16 nm, and Ta, respectively. The red and green solid lines are the symmetric

and anti-symmetric components separated from the mixing voltage using Lorentzians. (c) The θ_S variation with excitation frequency of sample BS (4 nm). The error bars are from the uncertainties in the S and A values. (d) The plot of frequency versus resonance field of sample BS (4 nm); the red line is fit to Kittel's formula. Inset: linewidth versus frequency of sample BS (4 nm).

3.6 Estimation of spin-pumping contribution to the symmetric voltage

The spin-pumping might contribute to the symmetric voltage due to the inverse SHE and inverse Edelstein effect. The spin-pumping voltage is given by [46,65]

$$V_{SP} = \theta_S ewR\lambda \tanh({}^{t_{BS}}\!/_{2\lambda}) fg_{\uparrow\downarrow} \sin^2 \phi_p \sqrt{\frac{H_0}{H_0 + M_{eff}}} \tag{3.6.1}$$

where w, R, λ, f, φ, and $g_{\uparrow\downarrow}$ are the width of the device, resistance of the device, spin-diffusion length, excitation frequency, angle between field and current flow, and real part of the spin-mixing conductance, respectively. The maximum precession angle ϕ_p is given by

$$\phi_p = \frac{1}{dR/d\varphi} \frac{2}{I_{rf,tot}} \sqrt{S^2 + A^2} \tag{3.6.2}$$

where $I_{rf,tot}$ is total rf current supplied to the device and $dR/d\varphi$ is obtained by measuring anisotropic magnetoresistance (AMR) of the device.

The G_{eff} is given by

$$g_{\uparrow\downarrow} = \frac{4\pi M_s t_{FM}}{g\mu_B} (\xi - \xi_{\text{int}}) \tag{3.6.3}$$

where g is the Landé's g-factor, μ_B is the Bohr magneton, and ξ_{int} is the intrinsic value of the CoFeB damping constant. The G_{eff} value is determined to be 6.58×10^{18} m^{-2} of sample BS (4 nm)

after substituting in values of 0.0048 for ξ, 0.0030 for ξ_{int}, and 2.165 for g [112]. At 8.5 GHz excitation frequency θ_S =8.67, S=-70.3μV, A=-2.27μV, and H_0 =513.8 Oe. The AMR measurement gives $dR/d\varphi$ =0.62Ω/rad, and $I_{rf,tot}$ is estimated to be 26.8 mA (without considering loss); by plugging these values into Eqn. (3.6.2) ϕ_p is determined to be 8.6×10^{-3}rad. We have used λ as 1.6 nm [91]. After substituting all of the values into Eqn. (3.6.1), V_{SP} is determined to be 4.71 μV, which is less than 7% of the symmetric voltage and it can be safely discarded.

3.7 Current induced perpendicular CoFeB multilayer switching

The SOT arising from BS can be directly observed by switching a FM with perpendicular magnetization in close proximity to the spin-channel [2,68,69,113]. We prepared a Si/SiO_2/MgO (2 nm)/BS (4 nm)/Ta (0.5 nm)/CoFeB (0.6 nm)/Gd (1.2 nm)/CoFeB (1.1 nm)/MgO (2 nm)/Ta (2 nm) switching sample (labelled as BS switching sample) as shown in schematic diagram Figure 3.7.1 (b). And a control switching sample BS (4 nm) replaced by Ta (4.5 nm) for the switching experiment, which is labelled as Ta switching sample. The out-of-plane field sweep hysteresis loop of the BS switching sample (Figure 3.7.1 (a)) clearly shows the easy axis along the out-of-plane direction. *Ms* of as deposited BS switching sample is determined to be 300 emu/cc. The perpendicular magnetization anisotropy originates from the negative exchange interaction between the CoFeB and Gd layers, in addition to the interfacial effect. The anisotropy energy density, anisotropy field, and coercivity of the switching sample are determined to be approximately 1.5×10^6 erg/cc, 6000 Oe, and 100 Oe, respectively.

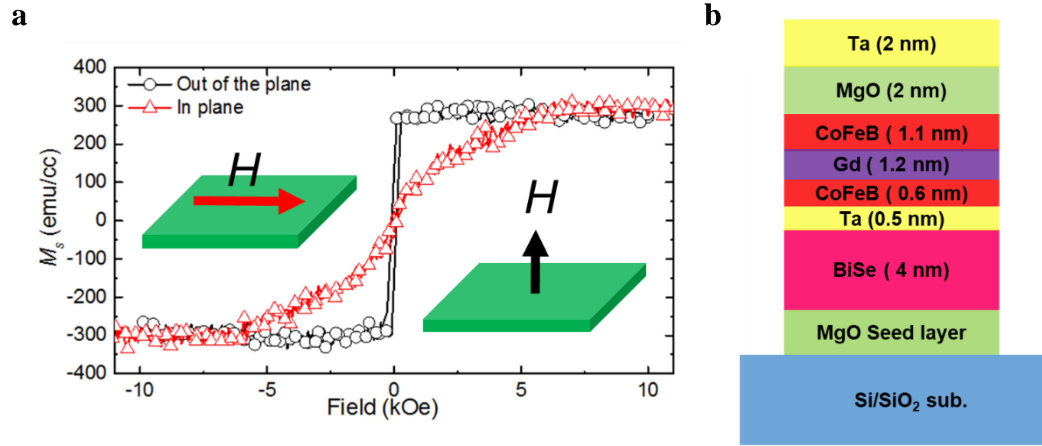

Figure 3.7.1 (a) The VSM measurement of the BS switching sample shows that the easy axis is in the out-of-plane direction and the anisotropy field is approximately 6000 Oe. (b) Schematic diagram of BS switching sample.

Figure 3.7.2 (b) shows the R_{AHE} loop of the BS switching sample obtained by sweeping the out-of-plane field at a constant input current of 50 μA. The non-zero R_{AHE} at zero magnetic field confirms the easy axis of the magnetization along the out-of-plane direction. The R_{AHE} loops of the BS switching sample resulting from current sweep under the application of a constant + 80 Oe and - 80 Oe field along the current channel are displayed in Figure 3.7.2 (c) and (d), respectively. The magnetization switching occurs at approximately ±7.2 mA as shown in Figure 3.7.2 (c) and (d). Upon changing the polarity of the external field, the chirality of the R_{AHE} loop changes, which is consistent with the results of previous reports [2,69,113]. The σ_c of the CoFeB (0.6 nm)/Gd (1.2 nm/CoFeB (1.1 nm) stack is found to be $5.3 \times 10^5\,\Omega^{-1}\text{m}^{-1}$. In our switching samples, the Ta capping thickness is 2 nm, which is completely oxidized as a result; current flow through the capping layer is ignored. The σ_c of the BS (4 nm)/ Ta (0.5nm)/MgO (5nm) is $1.4 \times 10^4\,\Omega^{-1}\text{m}^{-1}$. J_{sw} in switching BS sample is estimated to be ~4.3×10^5 A/cm^2.

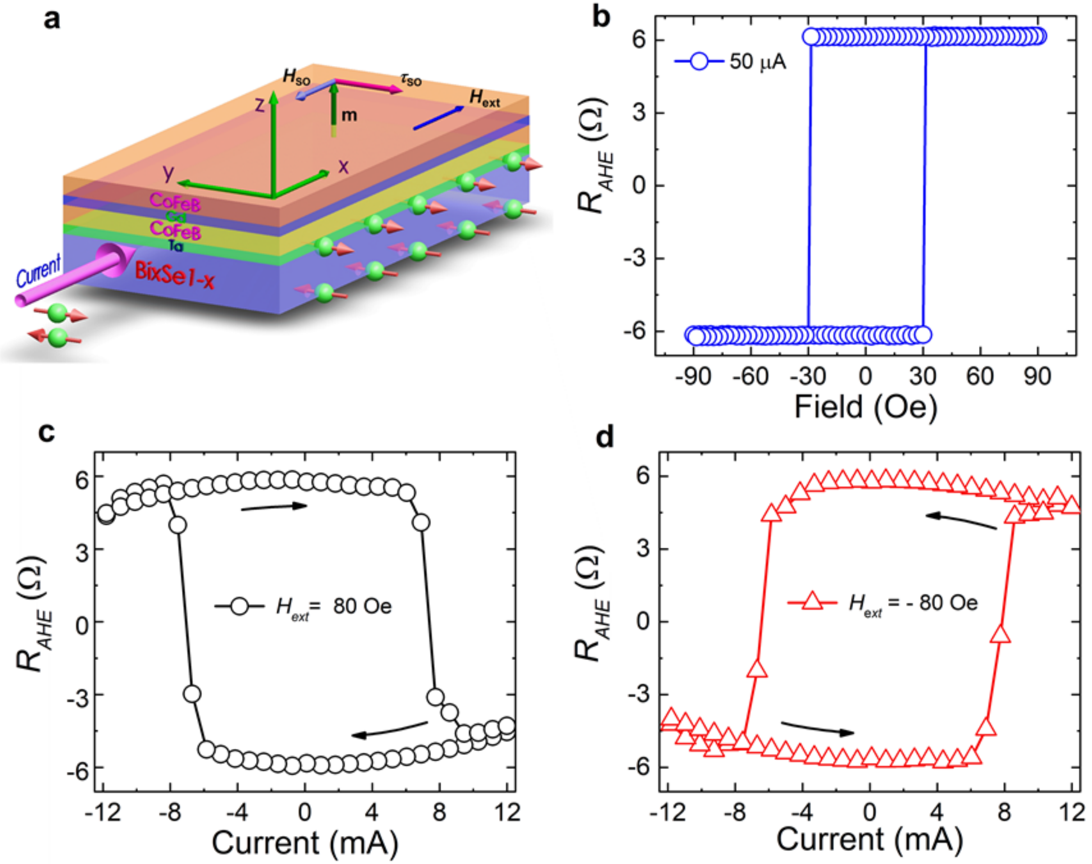

Figure 3.7.2 Current-induced magnetization switching in the BS (4 nm)/Ta (0.5 nm)/CoFeB(0.6 nm)/Gd (1.2 nm)/CoFeB (1.1 nm) heterostructure. (a) A schematic drawing of the switching sample stack structure. (b) The R_{AHE} measured in the BS switching sample using a current of 50 μA. (c) and (d) Current-induced switching of the magnetization due to the SOT arising from the BS underlayer in the presence of a constant 80 Oe in-plane bias field. The Hall-cross bar with dimensions of 15 μm × 70 μm is used for the switching experiment.

Figure 3.7.3 (b) shows the results of measurement of the out-of-plane magnetization by measuring R_{AHE} in the Ta switching sample; these results confirm that the perpendicular magnetic anisotropy as R_{AHE} is hysteretic and non-zero at zero magnetic field. In the presence of + 80 Oe bias field along the current channel (Figure 3.7.3 (c)), the dc current

sweep from positive to negative current favors magnetization in the upward direction (M_z>0), and switching of the magnetization occurs at ~ -24.6 mA. J_{sw} of Ta switching sample occurs at ~ 2.0 × 10^7 A/cm^2. The J_{sw} of CoFeB/Gd/CoFeB switching via SOT from PtMn is ~ 10^7 A/cm^2 [114].

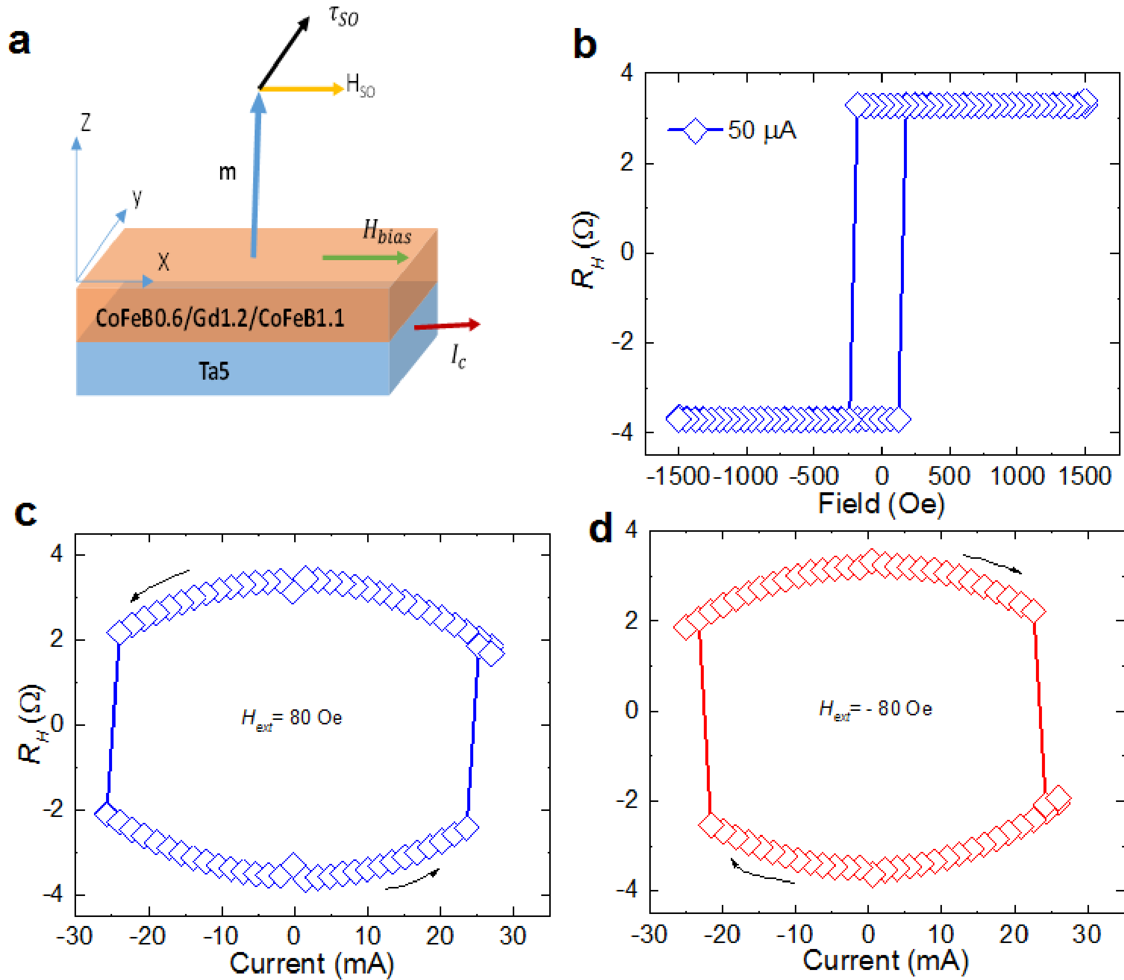

Figure 3.7.3 Current-induced magnetization switching in the Ta (5 nm)/CoFeB (0.6 nm)/Gd (1.2 nm)/CoFeB (1.1 nm) heterostructure. (a) Schematic drawing of the stack structure with thicknesses in nm and SOT where numbers represent thickness of the layers in nm. (b) The anomalous Hall resistance measured in the Ta switching sample using a 50 μA current. (c) and (d) Current-induced switching of the magnetization due to the SOT arising from the Ta underlayer in the presence of a

constant 80 Oe in-plane bias field, measured using a Hall-cross bar with dimensions of 15 μm × 70 μm.

A comparison between SOT switching power dissipation ($\frac{J_{sw}^2}{\sigma_c}$) in our switching BS sample, recent reports on Bi_2Se_3, and best previously reported results on HMs are presented in Table 1. The switching power dissipation in our BS switching sample is approximately one order of magnitude smaller than in Bi_2Se_3/CoTb [75] and Pt/Co [68,69], whereas it is comparable with the in-plane Bi_2Se_3/NiFe [76].

Parameters	$Bi_xSe_{(1-x)}$ (This work)	Bi_2Se_3 [75]	Bi_2Se_3 [76]	β-Ta [2]	Pt [68,69]
σ ($\Omega^{-1}m^{-1}$)	0.78×10^4	9.43×10^4	2.43×10^4	5.3×10^5	4.2×10^6
σ_S ($10^5 \frac{\hbar}{2e} \Omega^{-1}m^{-1}$)	1.5	0.15	0.43	-0.8	3.4
θ_S	18.62	0.16	1.75	-0.15	0.08
J_{sw} (A/cm^2)	4.3×10^5*	3×10^6	6×10^5	5.5×10^6	2.85×10^7-10^8
Switching power dissipation ($\frac{J_{sw}^2}{\sigma}$ watt/m^3)	1.29×10^{15}*	9.54×10^{15}	1.48×10^{15}	5.7×10^{15}	1.93×10^{16}
Symmetry breaking external in-plane magnetic field (Oe)	80*	1000	0	100	100
Switched magnetic system	CoFeB/Gd/CoFeB Out-of-plane	CoTb Out-of-plane	NiFe In-plane	CoFeB Out-of-plane	Co Out-of-plane

*These results are of switching $Bi_xSe_{(1-x)}$ sample.

Table 1 A summary of the θ_S, σ_S, J_{sw}, σ_c, and switching power dissipation of the TIs and HMs in this work and the best previous reports at room temperature. Note that the switching current density is the current density only through the NM layer.

3.8 Effect of thin Ta insertion layer on SOT from BS in switching sample

The effect of the Ta (0.5 nm) insertion layer on the SOT in switching BS(4 nm) sample is studied by characterizing the SOT of the switching stack using the second harmonic Hall method. Additionally, the perpendicular CoFeB/Gd/CoFeB is replaced by an in-plane CoFeB (5 nm) layer on which ST-FMR is performed. In the second harmonic Hall measurement, an ac current $I = I_0 \sin\omega t$, with frequency of 133.7 Hz and amplitude (I_0) up to 4 mA, is injected into the Hall-cross bar, and the first (V_ω) and second harmonic ($V_{2\omega}$) Hall voltages are measured as a function of the external field angle. The Hall-cross bar used for the harmonic measurement is 10 μm wide and 70 μm long with a 5 μm wide voltage probe. The ac current injected into the Hall-cross bar induces an effective spin-orbit field, which oscillates the magnetization around its equilibrium position, and as a result, a second harmonic Hall voltage is induced. In the measurement, the sample is rotated in the *x-y* plane under constant static magnetic field larger than the H_K such that the magnetization remains always in-plane. The current-induced spin-orbit fields can be obtained by fitting the following relation over the second harmonic Hall resistance data [21,56]:

$$R_{2\omega} = \frac{R_{AHE} H_{OOP}}{2(H_{ext} - H_K)} \cos\alpha + \frac{R_{PHE}(H_T + H_{Oe})}{H_{ext}} (\cos 3\alpha + \cos(\alpha)) + R_{ANE} \cos\alpha \qquad (3.8.1)$$

where R_{ANE} is the anomalous Nernst effect induced resistance. The first and second harmonic Hall resistances at 3 mA current and constant 70 kOe in-plane field are presented in Figure 3.8.1 (a). The left and right axes correspond to the first harmonic and second harmonic resistances, respectively. The R_{PHE} is estimated to be ~-0.3981 Ω and is obtained by fitting $R_{1\omega}$ to the Eqn. $R_0 + R_{AHE}\cos(\alpha) + R_{PHE}\sin(2\alpha)$, where R_0 is the offset. The solid red line is fit to Eqn. (3.8.1) , from which the fitting parameters H_{OOP} and H_T are extracted. Figure 3.8.1 (b) shows H_{OOP} and H_T variation with respect to the different current densities. The values of $\frac{H_{OOP}}{J_{BS}}$ and $\frac{H_T}{J_{BS}}$

obtained from the linear fit are (229±3) and (-20.4 ± 0.6) Oe per 10^6 A/cm^2, respectively. The θ_S of the switching BSsample estimated by using Eqn. $\theta_S = \frac{2eM_s t_{FM}}{\hbar}\frac{H_{OOP}}{J_{BS}}$ is 6.0±0.1.

The ST-FMR mixing voltage versus static field of the in-plane BS (4 nm)/Ta (0.5 nm)/CoFeB (5 nm) sample is presented in Figure 3.8.1 (c). The resonance line shape shows that the mixing voltage is dominated by the symmetric component. The symmetric and anti-symmetric components are obtained by fitting the data over Eqn. (3.5.2). The θ_S is estimated to be as large as 1.35±0.06 at an excitation frequency of 6.5 GHz, which is similar to the θ_S value of the switching stack obtained by performing the harmonic Hall method. Furthermore, the sign of the θ_S obtained from both measurements is positive, confirming that the contribution of SOT is due to the BSlayer. In the inset of Figure 3.8.1 (c), θ_S is plotted against the excitation frequency, which shows that the variation of θ_S with frequency is negligible. θ_S has decreased significantly due to insertion of the Ta (0.5 nm) layer to get perpendicular magnetization in BS switching sample as compared to the in-plane sample BS4. The additional BS/Ta interface dissipates spin-density due to the spin-flip scattering [115]. Ta has spin-diffusion length larger than 0.5 nm, however, there is still loss of spin-density due to the spin-relaxation. Additionally, θ_S of Ta and BS are opposite as a result, spin-density generated by BS gets cancelled. In conclusion, the θ_S value decreases due to the thin Ta insertion layer; however, it is still significantly larger than the values for any other NMs reported with a perpendicular magnetic layer grown over them at room temperature.

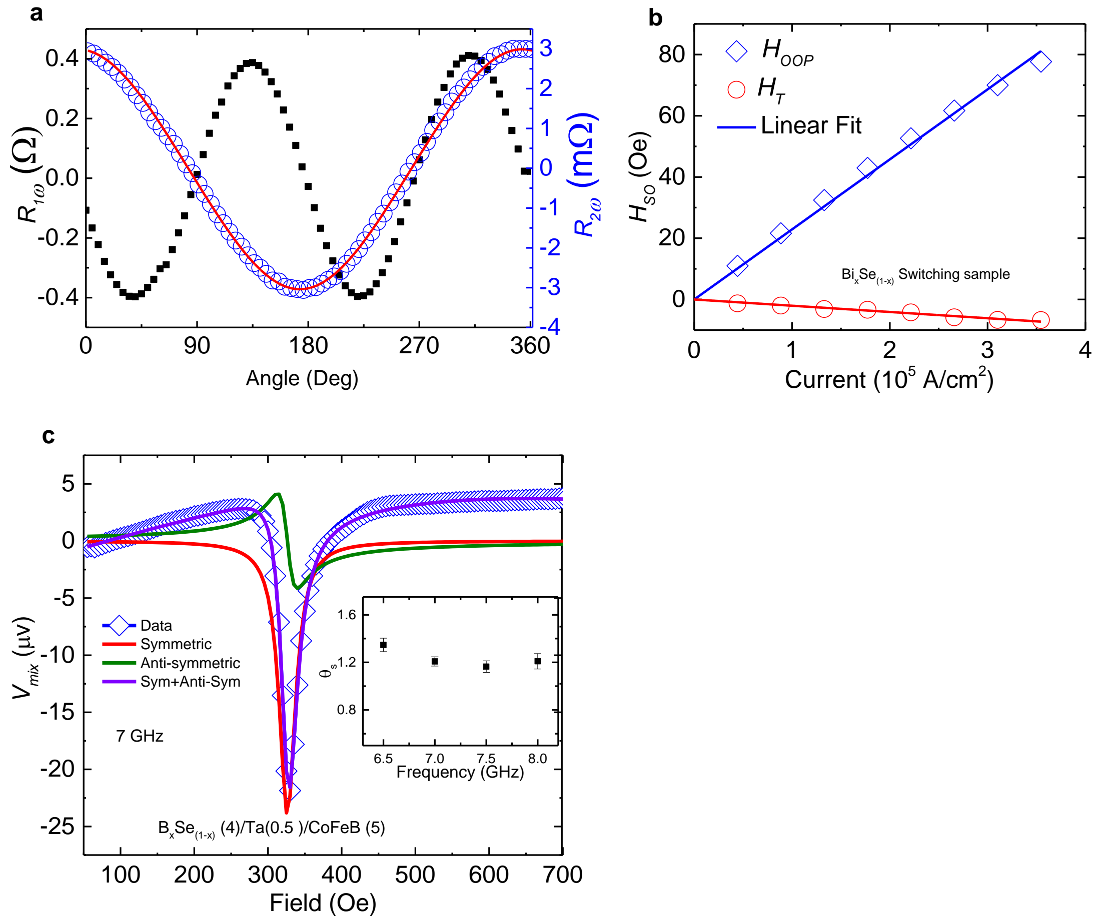

Figure 3.8.1 Characterization of SOT in BS (4 nm)/Ta (0.5 nm) layer. (a) The first and second harmonic resistances as a function of the field angle. The red solid line is fit to Eqn. (3.8.1). *(b) The current induced effective fields as a function of input bias current density. (c) The ST-FMR resonance line shape of the BS(4 nm)/Ta (0.5 nm)/CoFeB (5nm) sample at an excitation frequency of 7 GHz. Inset:* θ_S *is plotted against excitation frequency.*

In addition to the characterization of second harmonic Hall measurement of BS switching sample, we also performed the second harmonic Hall measurement of Ta switching sample. The first and second harmonic Hall resistances at 3 mA current and constant 70 kOe in-plane field for Ta switching sample are presented in Figure 3.8.2 (a). The left and right axes correspond to the first harmonic and second harmonic resistances, respectively. The R_{PHE} of Ta switching sample is

estimated to be ~-0.14 Ω. The Figure 3.8.2 (b) shows variation of $\frac{H_{OOP}}{J_{Ta}}$ and $\frac{H_T}{J_{Ta}}$ of Ta switching sample as a function of the current density. The values of $\frac{H_{OOP}}{J_{Ta}}$ and $\frac{H_T}{J_{Ta}}$ of Ta switching sample are estimated from the linear fit are (-6.2±0.1) and (-0.78 ± 0.08) Oe per 10^6 A/cm^2, respectively. The θ_S of the switching Ta switching sample estimated to be 0.16, which is comparable to the previously reported values [2,48].

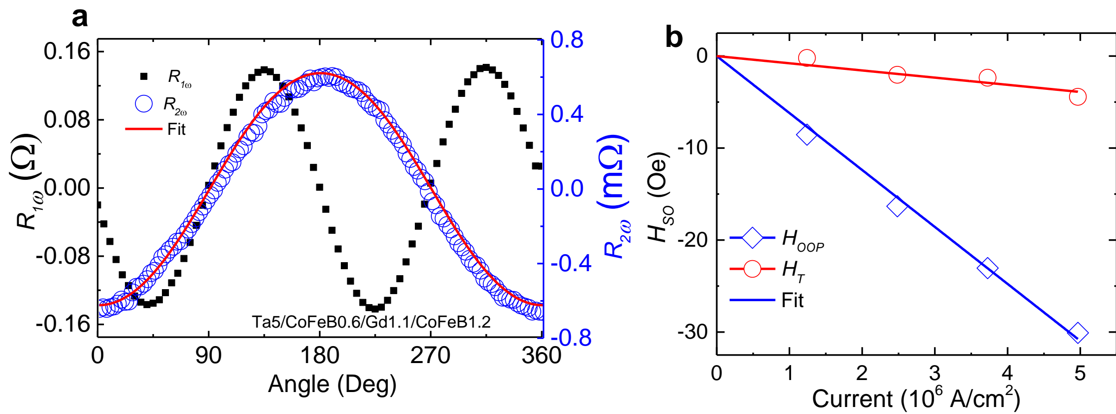

Figure 3.8.2 Characterization of SOT in Ta (5 nm)/CoFeB (0.6 nm)/Gd (1.2 nm)/CoFeB (0.6 nm). (a) The first and second harmonic resistances as a function of the field angle. The red solid line is fit to Eqn. (3.8.1) *(b) The current induced effective fields as a function of input bias current density.*

Chapter 4. Enhancement of the spin-accumulation due to quantum confinement

This chapter has been reproduced from the manuscript, "Room temperature high spin-orbit torque due to quantum confinement in sputtered $Bi_xSe_{(1-x)}$ films" by Mahendra DC, Roberto Grassi, Jun-Yang Chen , Mahdi Jamali, Danielle Reifsnyder Hickey, Delin Zhang, Zhengyang Zhao, Hongshi Li, P. Quarterman, Yang Lv, Mo Li, Aurelien Manchon, K. Andre Mkhoyan, Tony Low, and Jian-Ping Wang, which was published in Nature Materials **17, 800-808(2018).*

4.1 Introduction

A defining feature of our sputtered BS film is its granular nature with grain size down to order of nanometers, and the reduced dimensionality can have strong influence on electronic properties [116]. We perform quantum transport simulations (as well as calculations of the equilibrium properties in Fig. 3b,c,d) within the non-equilibrium Green's functions approach [117] using the same atomistic sp^3 tight-binding Hamiltonian as in [32]. Three geometries slab, wire, and dot are simulated by considering a simulation domain with finite length L_x in the transport direction but with different boundary conditions. In the slab and wire cases, semi-infinite leads are applied and the corresponding self-energies are calculated using a known iterative algorithm. In the dot case, a phenomenological self-energy corresponding to a contact-induced energy broadening of 1 eV is added to the on-site energies of the atomic orbitals belonging to the left and right, i.e. $(\bar{1}10)$, surfaces. This allows to distinguish between the contributions of forward and backward propagating states.

Equilibrium quantities are calculated assuming a flat electrostatic potential profile. The density-of-states are calculated by using following relation,

$$D(E) = \frac{1}{2\pi L_x L_y L_z} \mathrm{Tr}[G^R(\Gamma_1 + \Gamma_2)G^A] \quad (4.1.1)$$

where L_z is the TI thickness and the others symbols are as defined in the main text. Transport results at finite electric field are obtained by applying a small voltage V across the left and right contacts, such that the current

is in the linear regime, and by including a linear potential profile along the *x* direction. Results at finite *V* but zero electric field are obtained by approximating S_y and I_c as

$$S_y = e\int_{-\infty}^{\infty} dE S_{y,0}^{+}(E)[\frac{-\partial f_0}{\partial E}]V \quad (4.1.2)$$

$$I_c = \frac{e^2}{h}\frac{1}{L_y}\int_{-\infty}^{\infty} dE T_0(E)[\frac{-\partial f_0}{\partial E}]V \quad (4.1.3)$$

where the subscript 0 stresses the fact that the quantities are calculated in equilibrium condition.

The spin accumulation per unit area on the top surface is computed as

$$S_y = \int_{-\infty}^{\infty} dE\left[S_y^{+}(E)f_1(E) + S_y^{-}(E)f_2(E)\right] \quad (4.1.4)$$

where $f_{1,2}$ are the Fermi-Dirac distribution functions of the two contacts and

$$S_y^{+,-}(E) = \frac{1}{2\pi L_x L_y}\mathrm{Tr}[G^R\Gamma_{1,2}G^A P \otimes \sigma_y] \quad (4.1.5)$$

with $G^{R,A}$ the retarded/advanced Green's functions matrices and $\Gamma_{1,2}$ the broadening matrices corresponding to the left/right contacts. The charge current (per unit width) can be computed in a similar manner

$$I_c = \frac{e}{h}\frac{1}{L_y}\int_{-\infty}^{\infty} dE\, T(E)[f_1(E) - f_2(E)]$$

where the transmission function $T(E)$ is given by $T(E) = \mathrm{Tr}[\Gamma_1 G^R \Gamma_2 G^A]$. A bias of $V = 0.01$ V is applied between the Fermi levels of the left and right contacts and a corresponding uniform electric field $F = V/L_x$ is imposed along *x*. We also compare the results with the case where a small *V* is applied but $F = 0$, revealing insignificant differences.

4.2 Discussion and results

In Figure 4.2.1 (a), we show the evolution of the band structure as dimensionality is reduced from that of a 4 QL slab to its nanowire counterpart with the cross-section illustrated in the inset of Figure 4.2.1 (b). The electronic structure is modelled using an atomistic sp^3 tight binding Hamiltonian, which reproduces accurately the bulk band structure of Bi_2Se_3 obtained from *ab initio* calculations [118]. Electronic bands of the wire revealed additional states that are not within the energy spectrum of the slab (grey shaded region). Analysis of the wave functions presented in Figure 4.2.2 (a) affirm that the additional bands have a surface character and are localized mainly on the wire sidewalls and corners. The surface states exhibit robust spin-momentum locking as shown by the color plot in Figure 4.2.1 (a), where the color denotes projected in-plane spin density (S_y) on the top (111) surface of the nanowire. More precisely, using matrix notation,

$$S_{y,\upsilon} = \psi_\upsilon^\dagger P \otimes \sigma_y \psi_\upsilon$$

with P the projector matrix to the atomic orbitals belonging on the top surface, σ_y one of the three Pauli matrices, and ψ_υ the normalized wavevector corresponding to the quantum number υ (we use normalized units with respect to $\hbar/2$). Here, only S_y for forward propagating states (positive group velocity v_x) are shown, with the dominant contribution coming from the lowly dispersive surface bands.

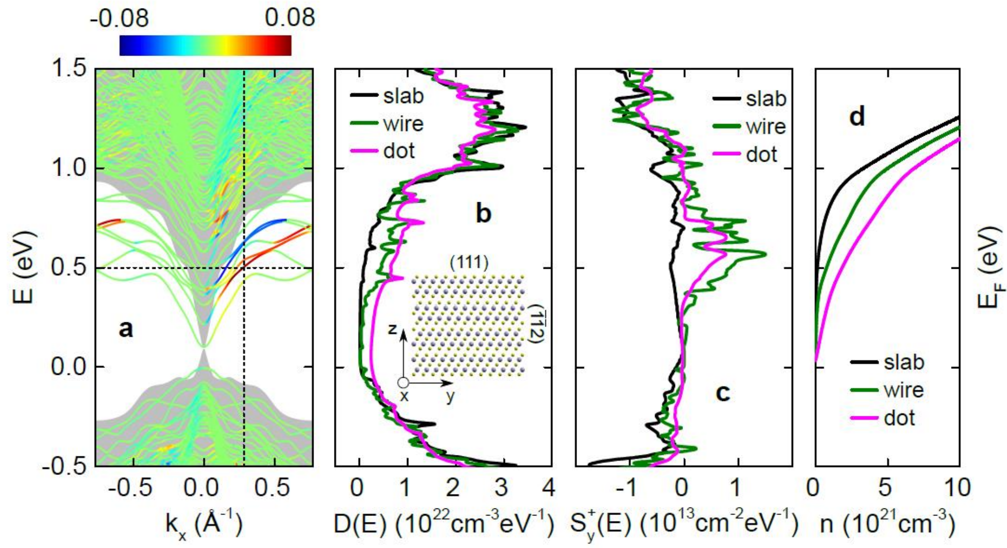

Figure 4.2.1 Effect of quantum confinement on spin accumulation. (a) Band structure of a slab (grey shaded region) and a square wire (lines) with a thickness of 4QLs. The color represents the projected spin density (y-component) on the top surface of forward propagating states. (b) Density-of-states vs energy for the slab, wire, and a cubic dot with the same thickness of 4QLs. Inset of (b), cross section view of the wire atomic structure. (c) Total projected spin density on the top surface of forward propagating states vs energy. (d) Carrier density vs Fermi energy at 300 K.

In the case of nanodot, the electronic band structure consists of discrete energy states which are best visualized through its density-of-states as shown in Figure 4.2.1 (b). We found a close similarity between the wire and dot spectra. In both cases, the density-of-states spectrum is enhanced in the energy window 0.3 – 0.9 eV compared to the slab case. In addition, some of the quasi-singularities in the spectrum of the wire persist in the nanodot spectrum at similar energies. This clearly indicates that the additional lowly dispersive states of the wire survive in the dot geometry. These states also produce enhanced surface S_y spectrum, as shown in Figure 4.2.1 (c). Here, the total contribution (per unit area) of states at energy E is considered, e.g. in the dot case:

$$S_y^+(E) = \frac{1}{L_x L_y} \sum_{\upsilon,\upsilon_x>0} \delta(E - \varepsilon_\upsilon) S_{y,\upsilon}$$

where $L_{x,y}$ are the dot dimensions in the x and y directions, δ is Dirac's delta function, ε_υ is the energy eigenvalue corresponding to ψ_υ, and the sum is restricted to forward propagating states. We have verified that the x and z components of the spin polarization of the top surface are typically smaller in all three geometries. The non-equilibrium spin polarization due to an applied current in an electron gas lacking inversion symmetry is also known as the Edelstein effect [32]. As we will elaborate below, we suggest that the additional lowly dispersive surface states due to the quantum confinement effect is the reason for high charge-to-spin conversion in our nano-scale granular sputtered BS (Refs. [119–122]). In this context, the intraband transitions at Fermi level produce the $\tau_\perp$, while interband transitions in the Fermi sea, associated with the Berry curvature of the surface states [22] , produces the $\tau_\parallel$ [119,120]. In the present model, we focus on the intraband driven Edelstein effect. Experimentally, it is also likely that defects or surface reconstruction might lead to built-in electric field, which can produce Rashba split bands [123], leading to additional contributions due to Rashba-Edelstein effect. However, due to the sub-10 nm nanoscale grain sizes in our experiments, the size confinement has a stronger influence on the energy spectrum.

To investigate this idea, we evaluate the quantum spin transport properties of a 2D array of Bi_2Se_3 grains of varying sizes ranging from 4 nm to 6 nm as shown in Figure 4.2.2 (b). The crystal orientation of these nano-grains along x, y, z directions are $[\bar{1}10]$, $[\overline{11}2]$, and [111], respectively. We consider electrical current flowing in the x direction using the standard non-equilibrium Green function approach. For comparison, we also consider the slab and wire counterparts of a dot with a thickness of 4 nm.

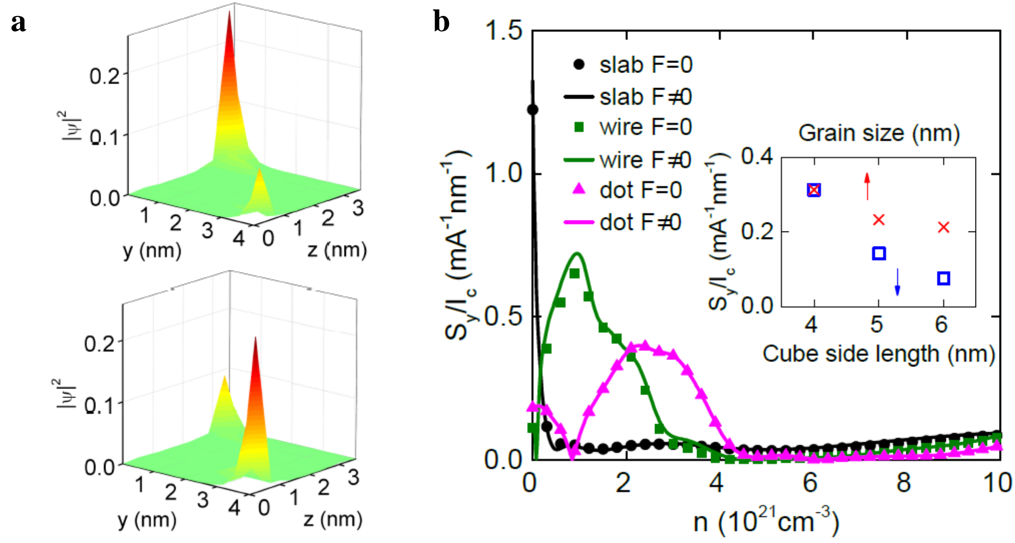

Figure 4.2.2 . (a) Two degenerate and orthogonal wave-functions of the wire corresponding to the energy and k-vector indicated by the dashed lines in Figure 4.2.1 (a). (b) Charge-to-spin conversion efficiency, i.e. the ratio between spin accumulation at the top surface and charge current, as a function of carrier concentration, calculated in the linear response with or without an applied electric field F. Inset of (b), conversion efficiency of the dot geometry, averaged over the range of carrier densities (n) $1\times10^{21} - 3\times10^{21}$ cm^{-3} and plotted as a function of confinement size, for dots with cubic shape (blue symbols) and for dots with the same thickness of 4QLs in the z direction and different size in the xy-plane (red symbols).

In Figure 4.2.2 (b), we plot as a function of carrier density, the ratio between S_y and I_c, which can be interpreted as a measure of the charge-to-spin conversion. The conversion between carrier density and Fermi level position in energy is provided in Figure 4.2.1 (d). Compared to the slab, the wire and dot geometries provide better performance in the range of carrier densities between 3×10^{20} and 3×10^{21} cm^{-3}. The enhancement can be traced back to the peaks in spin density spectrum occurring at about 0.55 eV (Figure 4.2.1 (c)). When the size of dot is increased from 4 to

6 nm, the average conversion ratio is decreased (inset of Figure 4.2.2 (b)), in agreement with the trend observed for $\frac{H_T}{J_{BS}}$ in the experiment (Figure 2.6.1 (f)). A similar trend is observed when the thickness is kept fixed at 4 nm and only the in-plane size (grain size) is increased, which can be explained by the fact that the surface states localized at the edges with the $(\overline{11}2)$ surfaces (Figure 4.2.2 (a) become less densely packed. These results suggest that reducing size and dimensionality can enhance SOT-efficiencies. Although our calculations have considered only the only the intraband current-driven spin-density responsible for the $\tau_{\perp}$, it is reasonable to speculate that the interband spin-density – not calculated in this model – should also be enhanced. As a matter of fact, the interband contribution is a correction to the intraband Edelstein effect arising from the precession of the non-equilibrium spin accumulation about the magnetization[43]. Therefore, the enhancement of the intraband Edelstein effect by quantum confinement is expected to be accompanied by a corresponding enhancement of the interband contribution. Our modeling is limited to ideal structures having a Bi_2Se_3 composition and a regular rectangular shape. The disordered nature of the experimental sputtered BS (stoichiometric ratio deviating from that of Bi_2Se_3 and irregular granular shape) might also influence the charge-to-spin conversion mechanism. For example, in Figure 4.2.3, we showed the influence on charge-to-spin conversion due to different crystal orientation.

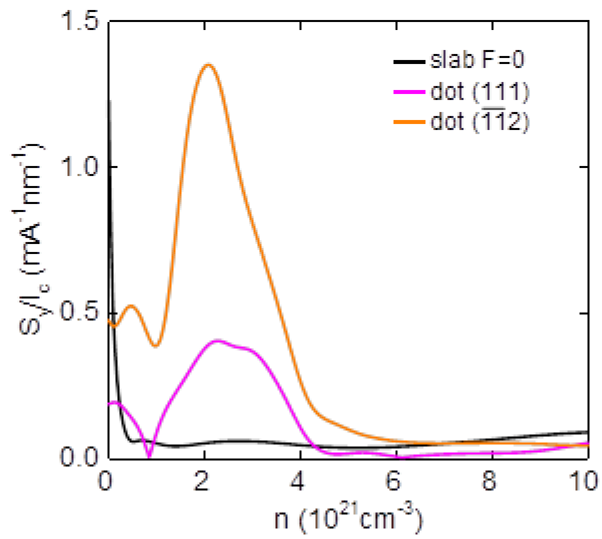

Figure 4.2.3 Effect of orientation on charge-to-spin conversion efficiency: Black and purple lines are efficiency ratio for slab and dot at zero electric field obtained by projected the spin density y component on the top surface. The orange line represents the spin density z component of the dot projected to the side surface. Size of the dot is 4x4x4 nm.

Chapter 5. Spin-to-charge conversion by sputtered bismuth selenide thin films at room temperature

**This chapter has been reproduced from the manuscript, "Observation of high spin-to-charge conversion by sputtered bismuth selenide thin films at room temperature" by Mahendra DC, Jun-Yang Chen, Thomas Peterson, Protyush Sahu, Bin Ma, Naser Mousavi, Ramesh Harjani, and Jian-Ping, which is currently under review in Nano Letters.*

5.1 Introduction

TIs have drawn a great deal of attention recently due to the efficient conversion of charge-to-spin and vice versa [34,65,67,87,104,124]. The main mechanism behind the efficient interconversion between charge and spin is the spin-momentum locking in TIs due to spin-orbit coupling [34,37,125–127]. Additionally, quantum confinement enhances the conversion of charge-to-spin in nano-sized granular TIs [124]. Recently, a logic device known as magneto-electric spin-orbit (MESO) has been proposed, which uses spin-to-charge conversion for the reading of data bits [128,129]. MESO requires high spin-to-charge conversion voltage for its operation. In this chapter, we present spin-pumping from sputtered granular bismuth selenide (BS)/CoFeB thin films at room temperature. The thin films with the stack structure Si/SiO_2/MgO (2 nm)/ BS (2, 4, 6, 8, and 16 nm)/CoFeB (5 nm)/MgO (2 nm)/Ta (2 nm) were prepared by magnetron sputtering for the spin-pumping experiments. Unless otherwise stated the labeling BS2-BS16 will be used for the samples with thickness of the BS layer ranging from 2-16 nm, respectively. Room temperature magnetron sputtering was carried out in an ultra-high vacuum (UHV) six-target Shamrock sputtering system with a base pressure of 5.0×10^{-8} Torr. A composite target of Bi_2Se_3 was sputtered at 30 W dc power and at 3 mTorr Ar pressure resulting in a deposition rate of ~ 0.6 Å/s. The MgO layer was rf sputtered at a deposition rate of ~ 0.07 Å/s, whereas the metallic layers Pt, Ta, Ag, and CoFeB were dc sputtered at 3 mTorr Ar pressure.

5.2 Raman, XPS, and TEM characterization

The Raman spectrum of 16 nm thick BS film is presented in Figure 5.2.1. The peaks observed at 123 and 167 cm^{-1} correspond to E_g^2 and A_{1g}^2, respectively. These values agree well with the previously calculated and experimental values of Bi_2Se_3 films [130–132]. The A_{1g}^1 mode is absent in the spectrum due to the use of a filter. Thus, it is confirmed by Raman spectroscopy that Bi and Se form an alloy, not individual clusters. The Raman measurement was performed using a laser with wavelength of 532 nm. The other peak present in the Raman spectrum at 520 cm^{-1} corresponds to the Si substrate.

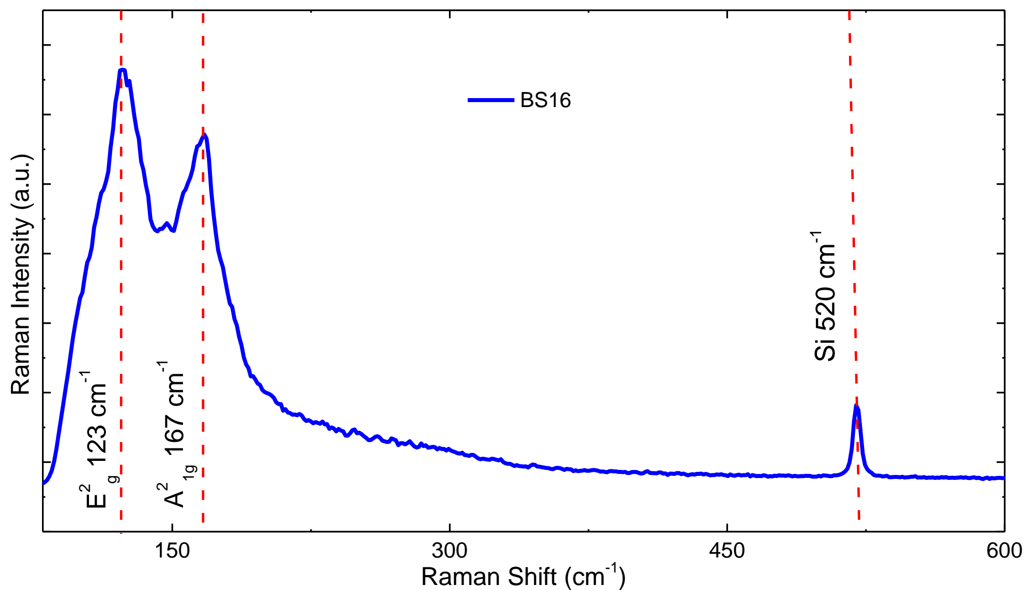

Figure 5.2.1 Raman spectrum of 16 nm thick BS thin film.

We performed X-ray photoelectron spectroscopy (XPS) measurement on BS8 sample using Al Kα X-ray source. XPS spectrum of BS film is presented in *Figure 5.2.2* shows a high-resolution Bi 4f spectrum. At binding energies 156.95 and 162.22 eV Bi $4f_{7/2}$ and $4f_{3/2}$, peaks are observed, respectively. The spin-orbit splitting of 5.27 eV of Bi 4f levels is comparable to the previous report [133]. The reported values of binding energies of metallic Bi $4f_{7/2}$ and $4f_{3/2}$ are 156.6

and 161.9 eV, respectively. The shift compared to metallic Bi 4f with our BS sample in 0.35 eV (blue-shift). In *Figure 5.2.2* (c) high resolution Se 3d spectra is presented. At binding energies 54.16 and 54.90 eV, Se $3d_{5/2}$ and $3d_{3/2}$ levels are seen, respectively. The spin-orbit splitting in the case of Se 3d is determined to be 0.74 eV. The binding energies and splitting of Se 4d levels are also comparable to the previous reports [133,134]. The reported values of binding energies of elemental $3d_{5/2}$ and $3d_{3/2}$ are 54.5 and 55.3 eV, respectively. Our BS samples show Se red-shift by 0.34 eV. The atomic concentration of Bi and Se in our sputtered bismuth selenide film is obtained by estimating area under Bi 4f and Se 4d levels, which is determined to be Bi: (42.81±0.52)% Se: (57.2±0.70)%, respectively. This is very close to the stoichiometry of the target Bi_2Se_3.

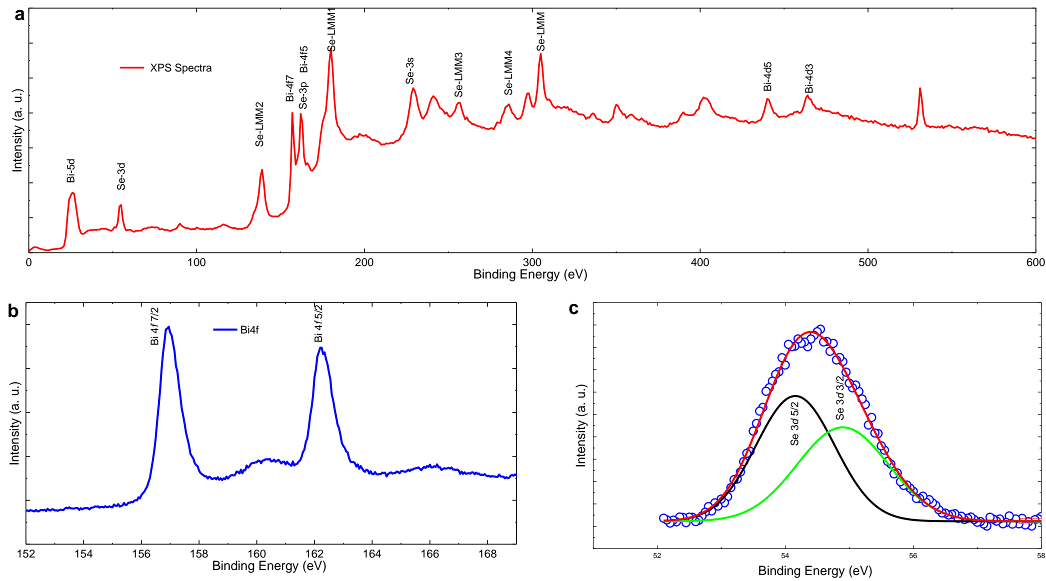

Figure 5.2.2 (a) XPS spectra of BS sample (b) High resolution 4f bands of Bi and (c) 3d bands of Se, respectively.

The resistivity of BS (4 nm) film increases with decrease in temperature as shown in Figure 5.2.3 (a). The room temperature resistivity of BS (4 nm) is estimated to be ~ 6000 μΩcm. The Hall resistance measured on Sub/ BS (4 nm) as a function of the magnetic field is presented on Figure

5.2.3 (b). The carrier concentration obtained by linear fit on the Hall data is estimated to be 2.6×10^{20} cm^{-3}.

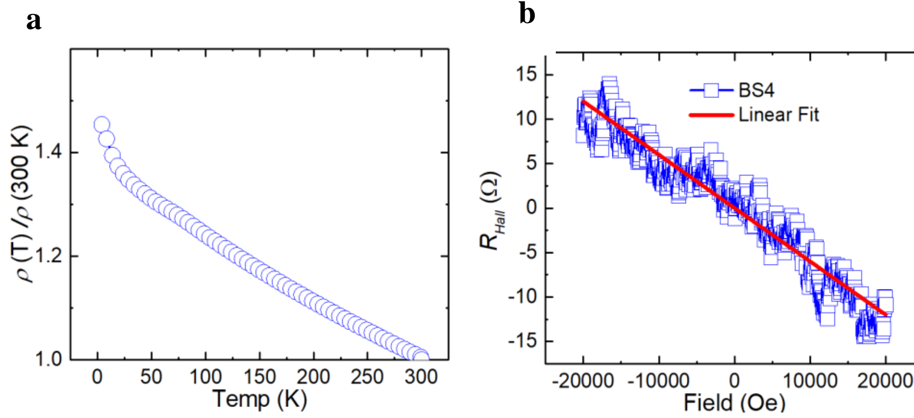

Figure 5.2.3 (a) Temeperature dependent resistivity of 4 nm thick BS film. (b) Hall measurement of 4 nm thick BS film at room temperature.

The cross-sectional HAADF-STEM image of sample BS8 is presented in Figure 5.3.1 (b). The CoFeB and MgO layers are amorphous, as expected, whereas the BS has a polycrystalline structure and the atomic layers of Bi and Se are continuous within grains. The average grain size in the BS8 sample is approximately 18 nm wide and 8 nm high, which is consistent with our previous batch of samples (Chapter 3) [124]. Moreover, TEM image shows that the interface between BS and CoFeB is sharp, which is necessary for efficient spin-pumping.

5.3 Spin-pumping into BS from CoFeB

The thin film samples were patterned into rectangular strips with a width and length of 620 μm and 1500 μm, respectively using photolithography and ion milling. Then SiO_2 with thickness of ~ 50 nm was deposited to insulate the CoFeB layer from the wave-guide. The shorted coplanar wave-guides and contacts were patterned using lithography and Ti (10 nm)/Au (150 nm) was deposited using an e-beam evaporator. The spin-pumping measurements were performed on the

symmetric wave-guide with the signal line width of 75 μm, ground width of 225 μm, and separation between the ground and signal line of 37.5 μm. These spin-pumping devices are similar to our previous reports [87,135].

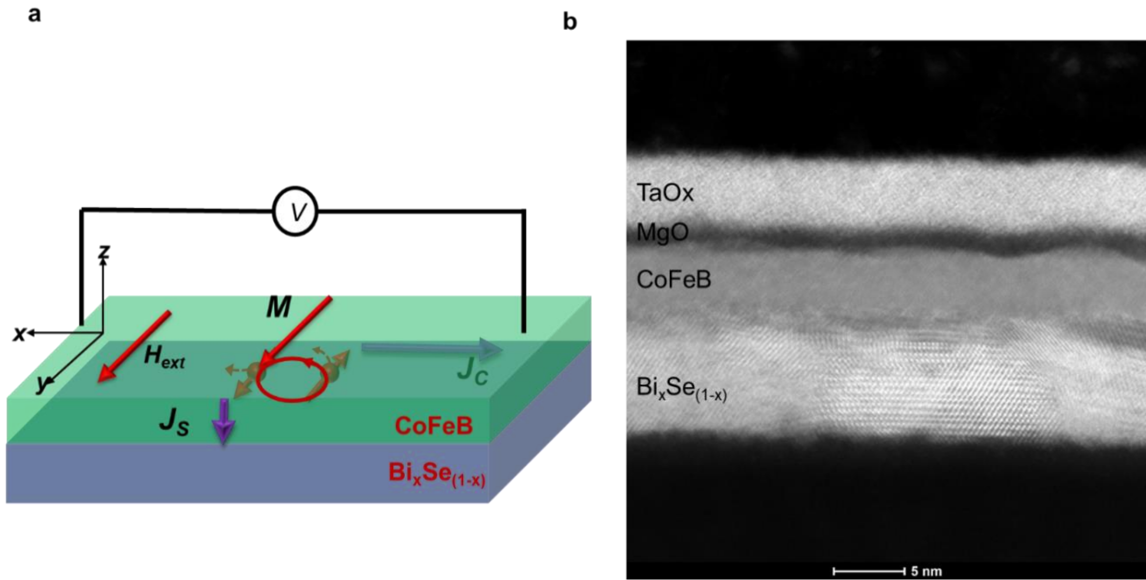

Figure 5.3.1 Spin-pumping into $Bi_{0.43}Se_{0.57}$ and structural characterization. (a) Schematics of the experimental set up for the spin-to-charge conversion (b) TEM image of the BS8 sample.

The schematics of the spin pumping into the BS layer is shown in Figure 5.3.1 (a). The rf field induces a precessional magnetization of the CoFeB layer at a fixed frequency in the GHz range. At resonance the CoFeB layer pumps spin into the BS layer and the spin-momentum locking present in the BS layer creates a non-equilibrium charge accumulation [103,104]. The open circuit voltage is probed by using a nanovoltmeter. Figure 5.3.2 (a) shows the measured open-circuit voltage (V) as a function of the external magnetic field (H_{ext}) at an excitation frequency (f) of 9 GHz and an excitation amplitude of 2.0 V (~19.03 dBm). V can be attributed to the contribution from the IEE effect (V_{IEE}), Seebeck effect (V_{SE}), and anomalous Hall effect (V_{AHE}) or anomalous

magnetoresistance (V_{AMR}). The V_{IEE} and V_{SE} can be separated from V_{AHE} by fitting the experimental data to the symmetric and antisymmetric Lorentzian provided below in Eqn. (5.3.1)

$$V = \frac{V_S \Delta H^2}{\Delta H^2 + (H_{ext} - H_0)^2} + \frac{V_A (H_{ext} - H_0)}{\Delta H(\Delta H^2 + (H_{ext} - H_0)^2)} \tag{5.3.1}$$

where ΔH is the line-width, which is also extracted by fitting, and H_{ext} is the external dc magnetic field. The V_{IEE} and V_{SE} corresponds to the coefficient of symmetric component (V_S) and the coefficient of anti-symmetric component (V_A) corresponds to (V_{AHE}), respectively. Then the V_{IEE} and V_{SE} can be separated by using $V_{IEE} = (V_S(+H_0) - V_S(-H_0))/2$ and $V_{SE} = (V_S(+H_0) + V_S(-H_0))/2$, respectively. At a positive and negative resonance field ($\pm H_0$) V_S changes sign, which corresponds to the change in the spin direction. As expected, V_A doesn't change sign at $\pm H_0$. Figure 5.3.2 (b) shows V as a function of the excitation frequency at constant excitation amplitude for the BS2 sample. Increase in V as the excitation frequency decreases is consistent with the previous report [136]. V_{IEE} as a function of the BS film thickness is presented in Figure 5.3.2 (c). V_{IEE} decreases with increase in thickness of the BS films. V_{IEE} as a function of the excitation amplitude is presented in Figure 5.3.2 (d). V_{IEE} shows parabolic behavior with the excitation amplitude consistent with previous reports [87]. f as a function of the H_0 is presented in Figure 5.3.3 (a) for different BS samples. The data points are fitted to the Kittel formula, $f = \frac{\gamma}{2\pi}\sqrt{H_0(H_0 + 4\pi M_{eff})}$, where γ is the gyromagnetic ratio to extract M_{eff}. The ΔH as a function of the excitation frequency is presented in Figure 5.3.3 (b). The damping constant (α) is obtained by fitting the $\Delta H = \Delta_0 + \frac{4\pi}{\sqrt{3}\gamma}\alpha f$ relation to the ΔH versus f data, where Δ_0 corresponds to the inhomogeneities present in the CoFeB layer. α as a function of the different BS samples is presented in Figure 5.3.3 (c) (left y-axis). The enhancement in the α of the BS samples

as compared to the control sample: $Si/SiO_2/CoFeB$ (details in Section 5.2) value of α (0.003) corresponds to the spin-to-charge conversion [78].

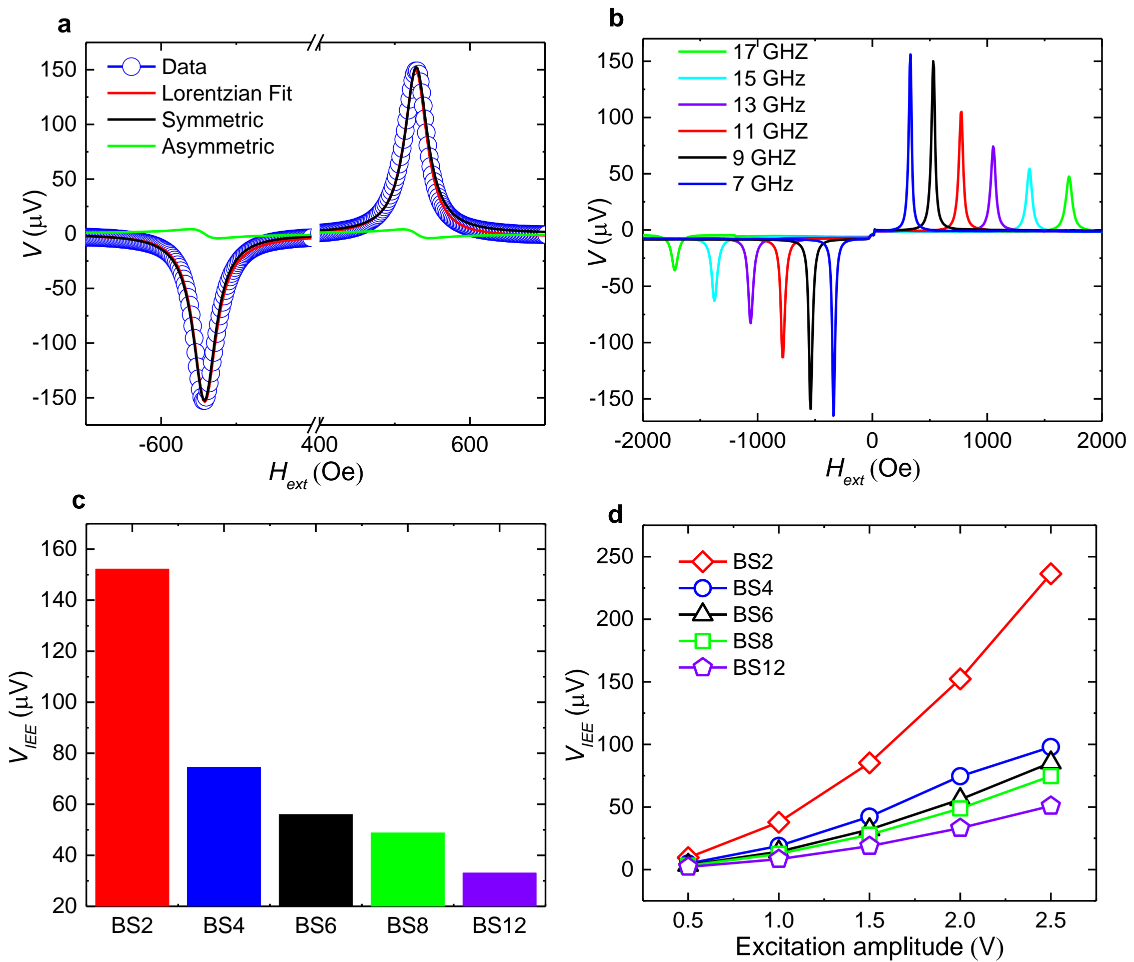

Figure 5.3.2 Conversion of spin-to-charge current by spin-pumping in to sputtered $Bi_{43}Se_{57}$ thin films (a) The spin-pumping voltage measured in BS2 sample at 9 GHz excitation frequency. (b) The spin-pumping voltage in BS2 sample as a function of the excitation frequency. (c) The spin-pumping voltage as a function of the BS film thickness at 9 GHz excitation frequency and 2.0 V excitation amplitude. (d) The spin-pumping voltage as a function of the excitation amplitude for different samples at 9 GHz excitation frequency.

The spin-current density (J_s) injected from the CoFeB layer to the CoFeB/ BS interface is given by,

$$J_S = \frac{g_{\uparrow\downarrow}\gamma^2 h_{rf}^2 \hbar}{8\pi\alpha^2} \frac{(M_S\gamma + \sqrt{(M_S\gamma)^2 + 4\omega^2})}{(M_S\gamma)^2 + 4\omega^2} \frac{2e}{\hbar} \tag{5.3.2}$$

where M_S, $\omega(2\pi f)$, h_{rf}, $g_{\uparrow\downarrow}$, $\hbar$, and e are saturation magnetization of CoFeB, excitation frequency, microwave rf field, spin-mixing conductivity, Planck's constant, and electronic charge, respectively. $g_{\uparrow\downarrow}$ is presented in right axis of Figure 5.3.3 (c) as a function of BS samples. The $g_{\uparrow\downarrow}$ values estimated for the BS samples are comparable to the previous report [91].

At the 9 GHz excitation frequency and the 2.0 V excitation amplitude the h_{rf} is estimated to be 0.95 Oe. The J_s of the samples BS2-BS16, obtained by using Eqn. (5.3.2), is 4.24, 4.85, 3.57, 4.77, 4.06, and, 4.84 $\times$ 10^6 A/cm^2, respectively. The efficiency of the spin-to-charge conversion is given by [26,104]: $\lambda_{IEE} = \frac{J_C}{J_s} = \frac{V_{IEE}}{RwJ_s}$, where R and w are resistance and width of the device, respectively. V_{IEE}, R, and w for the BS2 sample are 152 µV, 183 Ω, and 620 µm, respectively. The λ_{IEE} for the BS2 sample is estimated to be 0.32 nm. This value of λ_{IEE} is comparable or better than the previously reported values in TIs and interfaces [26,33,89,137]. The λ_{IEE} as a function of the BS is presented in Figure 5.3.3 (d). λ_{IEE} shows the thickness dependence, which is opposite to the trend shown by crystalline Bi_2Se_3 [91] . The Fermi velocity (v_f) of BS (4 nm) is estimated to be 1.52 $\times$ 10^6 m/s. The momentum relaxation time (τ_m) in the surface states of BS4 sample is determined to be 9.21 $\times$ 10^{-17} S, using relation [26,33,103] $\lambda_{IEE} = v_f \tau_m$, which is an order of magnitude shorter compared to the previous reports on TIs and Rashba interfaces [33,99,138] but comparable to Cu/Bi [139] and YIG/BS [140] interfaces.

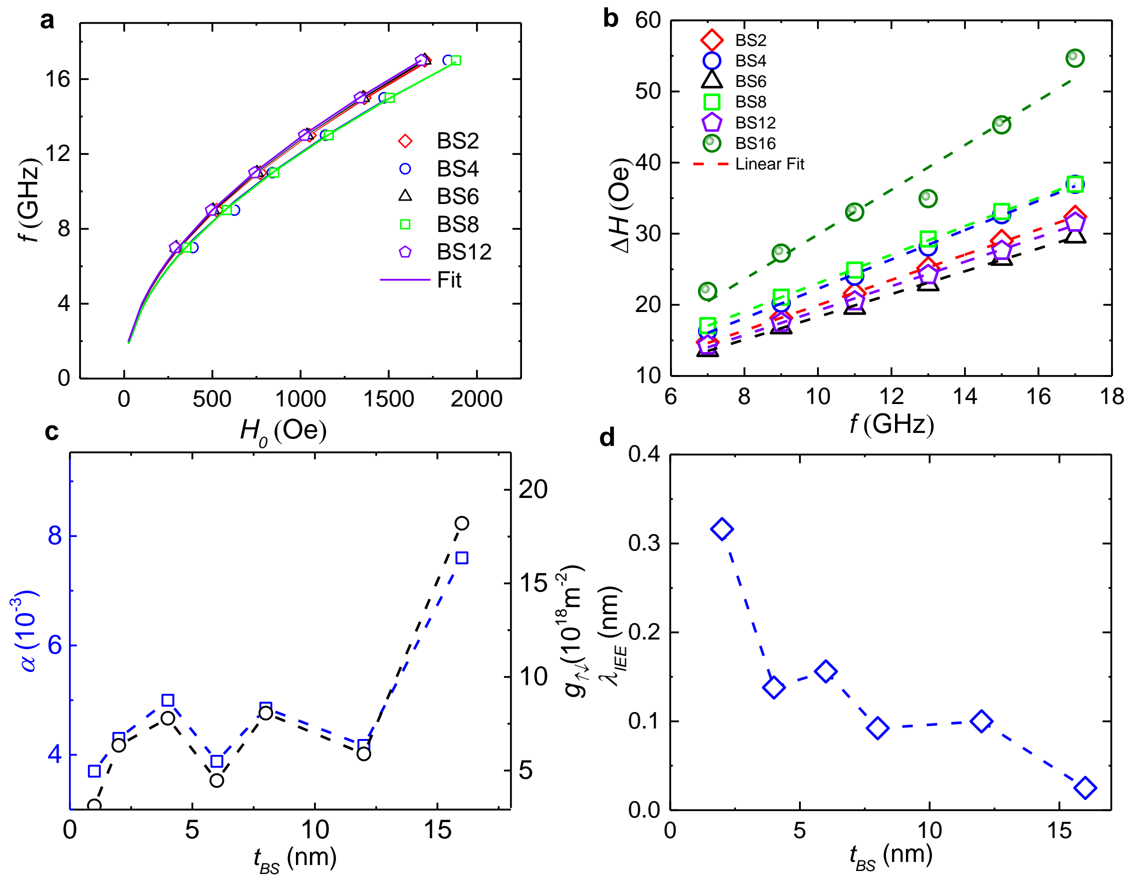

Figure 5.3.3 Characterization of spin-injection efficiency and inverse Edelstein effect length (a) Excitation frequency as a function of resonance field (b) The line-width as a function of the excitation frequency (c) Spin-mixing conductance (right axis) and damping constant (left axis) versus BS film thickness (d) Inverse Edelstein effect length as a function of the BS film thickness.

5.4 Spin-pumping on a control CoFeB sample

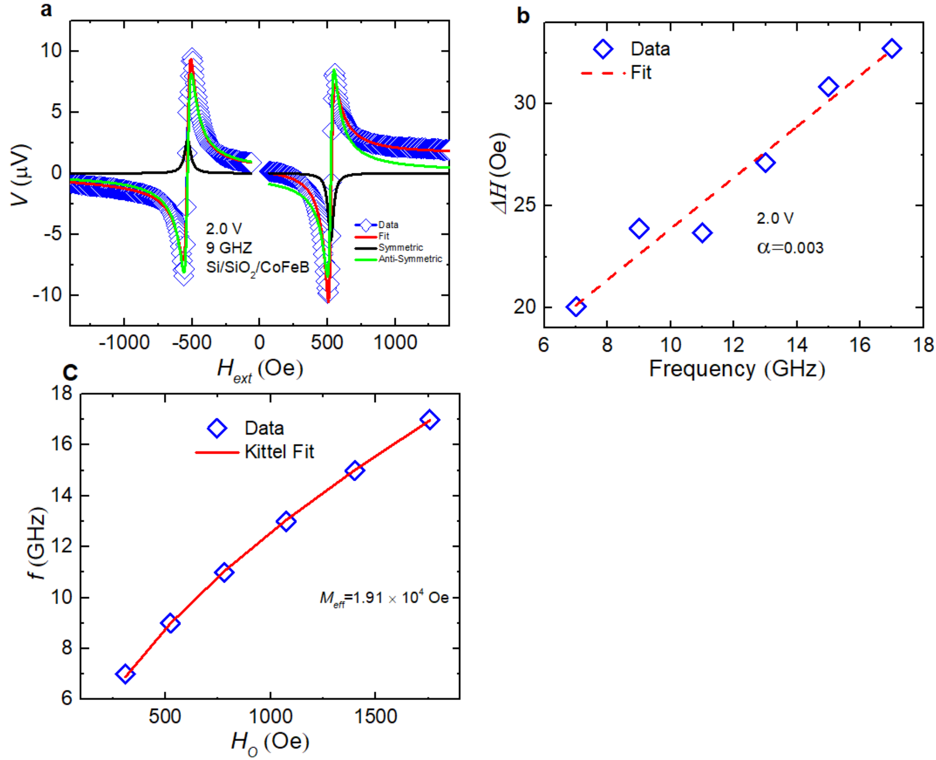

Figure 5.4.1 Characterization of α and M_s of control CoFeB sample. (a) The spin-pumping voltage measured in CoFeB sample at 9 GHz excitation frequency. (b) Line-width as a function of the excitation frequency. (c) Excitation frequency as a function of resonance field.

A control sample with the stack structure Si/SiO_2/CoFeB (5 nm)/MgO (2 nm)/Ta (2 nm) was prepared to determine intrinsic damping constant (α_{int}) of the CoFeB. The V_{SP} of the control sample CoFeB is as shown in Figure 5.4.1 (a). As expected the V_{AS} is dominant in CoFeB sample and a small V_S is observed mainly due to the Seebeck effect and self spin-pumping of the CoFeB layer. ΔH as a function of the excitation frequency is presented in Figure 5.4.1 (b). α_{int} determined by linear fit is 0.003. The excitation frequency is plotted against resonance field Figure 5.4.1 (c). The M_{eff} obtained by Kittel fitting is 1.91×10^4 Oe.

5.5 Spin-pumping on a reference Pt sample

A reference Pt sample with stack structure Si/SiO_2/Pt (10 nm)/CoFeB (5 nm)/MgO (2 nm)/Ta (2 nm) was prepared. The V_{SP} of the control sample Pt is as shown in Figure 5.5.1 (a). As expected the V_S is dominant, which corresponds to the spin-to-charge conversion voltage due to the inverse spin Hall effect and a small V_{AS} is due to AHE. ΔH as a function of the excitation frequency is presented in Figure 5.5.1 (b). α estimated by linear fit is 0.0066 and $g_{\uparrow\downarrow}$ is obtained to be 1.58×10^{19} m^{-2}. The excitation frequency as a function of the resonance field is presented in the Figure 5.5.1 (c). The M_{eff} is estimated to be 1.76×10^4 Oe using Kittel's formula. The V_{ISHE} as a function of the excitation voltage is presented in Figure 5.5.1 (d). The estimated J_S is 5.02×10^6 A/cm^2 and the spin Hall angle is obtained to be ~0.1 estimated by using Eqn. (1.8.5), λ used for the θ estimation was 3.4 nm [115]. This value of θ is comparable to the previous reports [115,141].

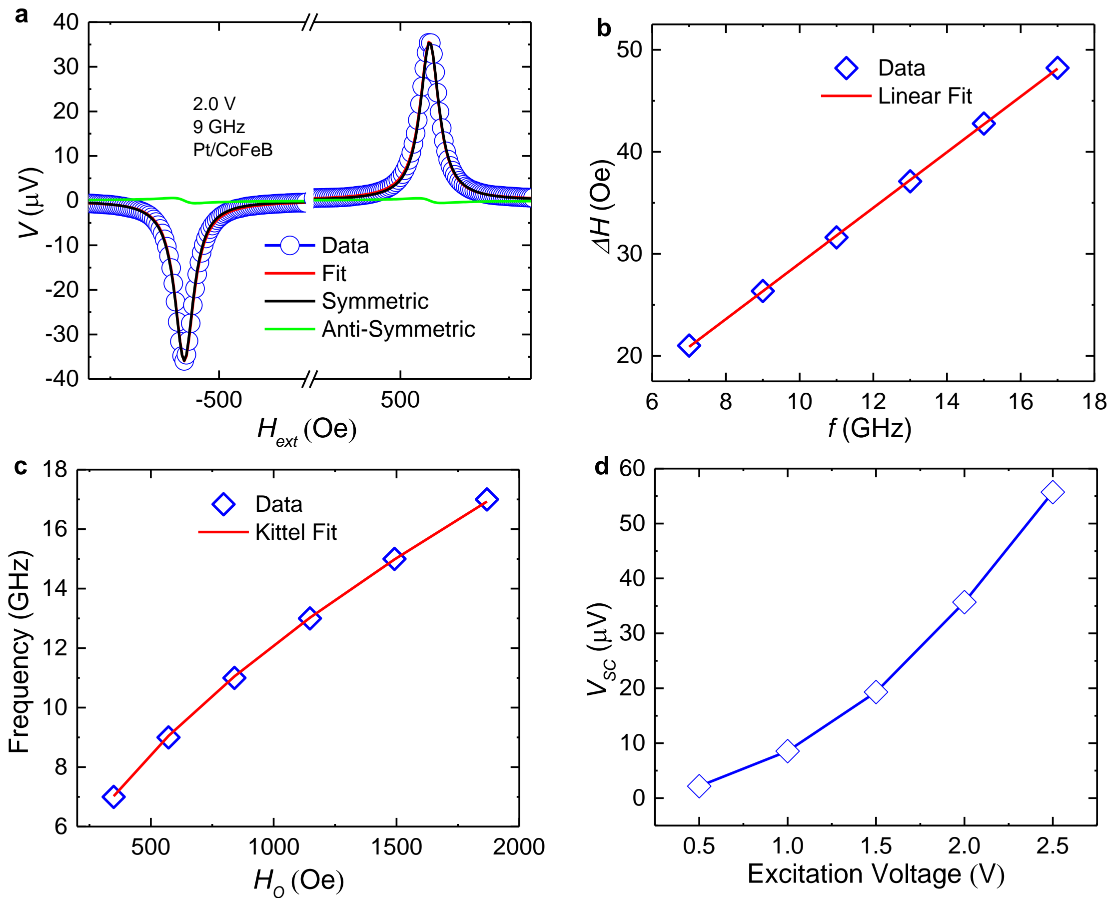

Figure 5.5.1 Spin-pumping in Sub/Pt (10 nm)/CoFeB (5 nm)/MgO (2 nm)/Ta (2 nm) (a) The spin-pumping voltage measured in Pt/CoFeB sample at 9 GHz excitation frequency. (b) Line-width as a function of the excitation frequency. (c) Excitation frequency as a function of resonance field.(d) ISHE voltage as a function of excitation voltage.

5.6 Effect on spin-to-charge conversion due to insertion layers

In addition to the Seebeck effect due to the microwave heating thermoelectric signals induced by Nernst and anomalous Nernst effects can contaminate the spin-pumping signal [94,142,143]. The spin-pumping signal can be suppressed by the insertion of a barrier layer such as MgO between the FM and the spin-sink if the spin-to-charge conversion is due to a physical mechanism [97,144] otherwise if the voltage is coming from the thermal artifacts it will remain almost the same. To identify whether the V_S is contributed from the IEE or thermal effects, we prepared a sample with stack structure of Sub/MgO (2 nm)/ BS (4 nm)/ MgO (1 nm)/CoFeB (5 nm)/MgO (2 nm)/Ta (2 nm), referred to as the BS-MgO sample. The V of the BS4 sample and the BS-MgO sample are presented in Figure 5.6.1 (a) and (b), respectively. It can be clearly seen that the V_S decreases quite significantly in the BS-MgO sample compared to the BS4 sample. α and $g_{\uparrow\downarrow}$ of the BS-MgO sample are 0.0032 and 7.76×10^{17} m^{-2}, respectively, which indicates that most of the spin-current pumped from CoFeB layer is reflected back. The reduction of the V_{IEE} by more than 5 times in the BS-MgO sample confirms negligible presence of the thermal signals.

Alves-Santos et al., observed giant enhancement in the spin-pumping signal induced by Ag nanoparticles due to the IREE [145]. Furthermore, It has been observed that the insertion of a Ag layer has enhanced the efficiency of the conversion from charge-to-spin due to the additional spin-momentum locking, induced by the Rashba-Edelstein effect [146]. We have prepared a sample with the stack structure Sub/MgO (2 nm)/ BS (4 nm)/ Ag (2 nm)/CoFeB (5 nm)/MgO (2 nm)/Ta (2 nm), labelled as BS-Ag sample, to investigate if a Ag insertion layer can enhance spin-to-charge conversion. Indeed, as shown in Figure 5.6.1 (c), V_{IEE} of the BS-Ag sample clearly indicates that

the spin-to-charge conversion is enhanced due to the insertion of the Ag layer. V_{IEE} is enhanced in the BS-Ag sample by approximately 40% compared to the BS4 sample. The V_{SE} in the BS4 and the BS-Ag samples is estimated to be 3.22 and 0.6 μV, respectively at 2.0 V excitation amplitude. Figure 5.6.1 (d) shows ΔH as function of the excitation frequency for the BS-Ag sample. α and $g_{\uparrow\downarrow}$ of the BS-Ag sample are determined to be 0.0051 and 1.02×10^{19} m^{-2}, respectively. In comparison to the BS4 sample both α and $g_{\uparrow\downarrow}$ enhanced on the BS-Ag sample. The λ_{IEE} of BS-Ag is found to be 0.20 nm, which is approximately 43% enhancement as compared to the BS4 sample.

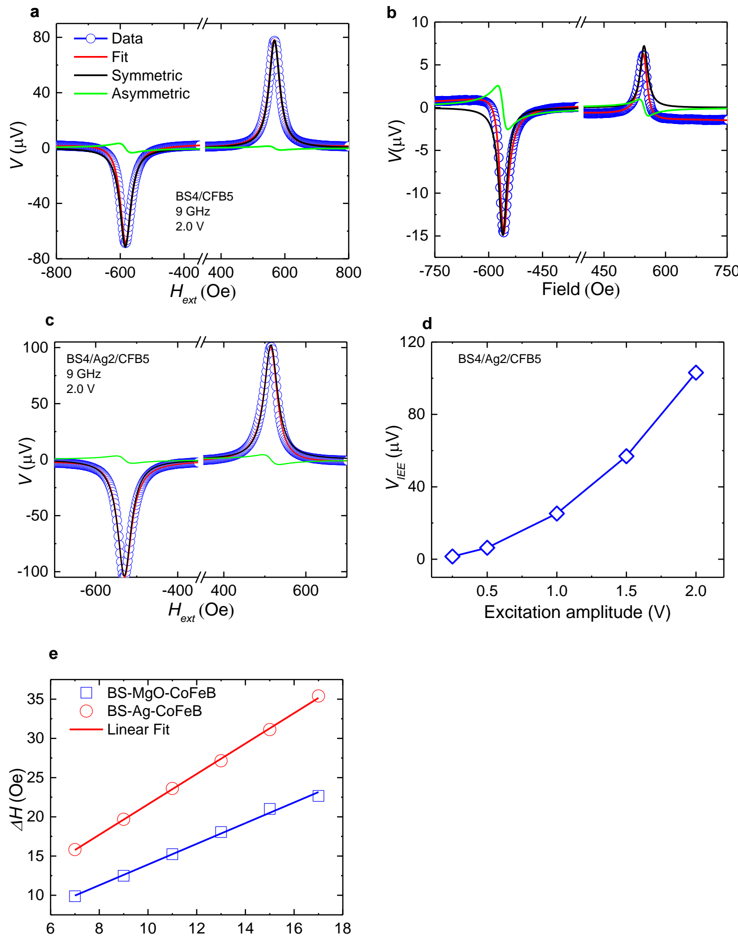

Figure 5.6.1 Influence of interfacial layers on spin-to-charge current conversion (a) The output dc voltage due to spin-to-charge current conversion in the BS4 sample (b), (c) Influence on the

spin-pumping voltage due to the insertion layers MgO (0.5 nm) and Ag (2 nm), respectively. (d) The spin-pumping voltage as a function of the excitation amplitude in BS-Ag sample. (e) The linewidth as a function of the excitation frequency.

5.7 Discussion

A large value of λ_{IEE} 2.1 nm is reported at room temperature in α-Sn interfaced with Ag/Fe, however, the additional contribution of the Ag insertion layer was not estimated [33]. A λ_{IEE} value of 0.075 nm was reported in $(Bi_{0.22}Sb_{0.78})_2Te_3$ at room temperature [90]. Shiomi et al., reported λ_{IEE} value of 0.1 nm in $Bi_{1.5}Sb_{0.5}Te_{1.7}$ at 15 K, but did not observe any spin-to-charge conversion by Bi_2Se_3 [88,89]. Jamali et al. and Deorani et al., observed significant contribution of bulk effect in spin-to-charge conversion from Bi_2Se_3 [87,111]. However, Wang et al. and Fanchiang et al. reported the spin-to-charge conversion in YIG/Bi_2Se_3 was mainly due to the Dirac surface states [91,147]. In order to confirm the mechanism of spin-to-charge conversion in our BS, we analyze $g_{\uparrow\downarrow}$ as a function of thickness of the BS films. $g_{\uparrow\downarrow}$ presented in Figure 5.3.3 (c) does not show any specific pattern as a function of the film thickness. If the mechanism of spin-to-charge conversion is due to the bulk effect $g_{\uparrow\downarrow}$ should linearly increase first and then saturates after certain thickness as a function of BS film thickness as in the case of HMs [79,148,149]. $g_{\uparrow\downarrow}$ as a function of film thickness dependence in our BS agrees with the previous reports in YIG/ Bi_2Se_3 [91,147]. Wang et al. and Fanchiang et al. reported the mechanism of spin-to-charge conversion in YIG/ Bi_2Se_3 was mainly due to the IEE. Furthermore, $g_{\uparrow\downarrow}$ as a function of BS thickness in case of BS/CoFeB shows similar behavior as in YIG/BS [140]. λ_{IEE} estimated in sputtered BS films is comparable or larger than the reported values of it in other TIs [33,67,87–91] and in interfaces such as Ag/Bi [26]and Fe/Ge [97] with mainly IEE and IREE being the origin of spin-to-charge conversion, respectively. With the overall comparable or larger value of λ_{IEE}, $g_{\uparrow\downarrow}$ of BS film thickness dependence agrees with the IEE mediated spin-to-charge conversion rather than the HMs,

we can conclude that the observed high spin-to-charge conversion voltage present in the sputtered BS samples is due to the IEE. In addition, with substantial reduction of V_{IEE} in the BS-MgO sample any thermal related voltages are safely ignored. In chapter 3, high charge-to-spin conversion in sputtered BS was observed. In chapter 4, quantum transport numerical simulations revealed that the the sub-10 nm sized grains present in the sputtered BS films further enhances in the conversion of charge-to-spin due to the additional bands arising from quantum confinement. The figure of merit for both the charge-to-spin conversion and the spin-to-charge conversion show similar thickness dependent behavior. The increase in the thickness of the BS films corresponds to the increase in the grain size and hence the decrease of the quantum confinement effect. The quantum confinement influences the spin-to-charge conversion as well, which can be seen in the dependence of λ_{IEE} as a function of BS thickness in our case versus in YIG/ Bi_2Se_3 showing opposite behavior [91]. Not only in case of our BS but there are also other reports in which grain dimensions have affected the spin-to-charge conversion as well as charge-to-spin conversion [145,150,151].

Chapter 6. Spin-to-charge conversion by sputtered bismuth selenide thin films via spin pumping from yttrium iron garnet

**This chapter has been reproduced from the manuscript, "Room temperature spin-to-charge conversion in sputtered bismuth selenide thin films via spin pumping from yttrium iron garnet", by Mahendra DC, Tao Liu, Jun-Yang Chen, Thomas Peterson, Protyush Sahu, Hongshi Li, Zhengyang Zhao, Mingzhong Wu, and Jian-Ping Wang, which is currently under review in Applied Physics Letters.*

6.1 Introduction

Spin-orbit coupling is an efficient mechanism for the generation and detection of spin current in spintronic devices [9,152]. The detection of spin current is possible through the inverse spin Hall effect (ISHE) [82–84,115,135,141], the inverse Edelstein effect (IEE) [32,33,137,87,88,90–92,94,103,104], and the inverse Rashba-Edelstein effect (IREE) [26,96,97,99]; these effects have been realized in HMs, TIs, and certain interfaces such as Ag/Bi [26], Ag/Sb [96], LAO/STO [99], etc., respectively. Spin-to-charge conversion can be used in logic device such as magneto-electric spin-orbit (MESO) device [128,153]. One can examine the spin-to-charge conversion via spin pumping; to obtain strong spin-pumping signals and avoid spurious effects in spin-pumping signal one usually uses the ferromagnetic resonance (FMR) in low-damping ferrimagnetic insulators such as yttrium iron garnets (YIG) [95,141,154–156]. So far spin-momentum locking in crystalline TIs is the most efficient mechanism for the spin-to-charge conversion [33,87]. However, spin pumping from YIG to granular TIs has not been studied yet. In our previous report we observed that the charge-to-spin conversion in sputtered granular bismuth selenide (BS) films can be significantly influenced by quantum confinement (QC) [124].

6.2 Film preparation and device fabrication

We prepared $Gd_3Ga_5O_{12}$ (GGG)/YIG (20 nm)/BS (4 nm) /MgO (2 nm)/Ta (2 nm) and (GGG)/YIG (30 nm)/BS (8, 12, and 16 nm) /MgO (2 nm)/Ta (2 nm) samples for the spin-pumping

measurements. Unless otherwise stated, we label samples with 4, 8, 12, and 16 nm thick BS films as YBS4, YBS8, YBS12, and YBS16 samples, respectively. A reference sample GGG/YIG (20 nm)/Pt (5 nm) /MgO (2 nm)/Ta (2 nm) was also prepared and was labelled as the YPt sample. The YIG films were grown on GGG (111) wafers by RF magnetron sputtering at room temperature first and then in-situ annealed at 800 °C for 2 hours under the oxygen pressure of 1 Torr. For the annealing process, the heating rate was 10 °C/min, while the cooling rate was 2°C/min. BS thin films were grown on GGG/YIG (20 nm and 30 nm) films at room temperature by sputtering a composite Bi_2Se_3 target with a base pressure of 5.0×10^{-8} Torr at 30 W power. The concentration of Bi and Se in BS films is determined to be 43% and 57%, respectively using X-ray photoelectron spectroscopy. The thin films were patterned into rectangular strips with the width and length being 620 μm and 1500 μm, respectively, using optical lithography and ion milling. Then, 50 nm thick SiO_2 was deposited using sputtering to insulate the films from waveguides. In the last step of the lithography, contacts and co-planar waveguides were defined. A 10 nm thick Ti layer followed by 150 nm thick gold layer was deposited using an e-beam evaporator for electrical contacts and waveguides. The spin-pumping measurements were performed on a co-planar waveguide that had a signal line width of 75 μm, a ground width of 225 μm, and a ground-to-signal line separation of 37.5 μm.

6.3 Spin-pumping from YIG to BS

Figure 6.3.1 (a) and (c) present an AFM image of the YIG (20 nm) film grown on the GGG substrate and an AFM image of a BS (8 nm) film grown on thermally oxidized silicon substrate, respectively. The AFM characterization of the YIG film shows that the film is smooth and has a RMS surface roughness of 0.109 ± 0.01 nm, while the AFM measurement of the BS (8 nm) film shows that the film is granular, with a RMS roughness value of about 0.54 nm. The magnetic properties of the YIG film was characterized by FMR under an in-plane external magnetic field. The FMR line shape of the GGG/YIG (20 nm) film is presented in Figure 6.3.1 (b).

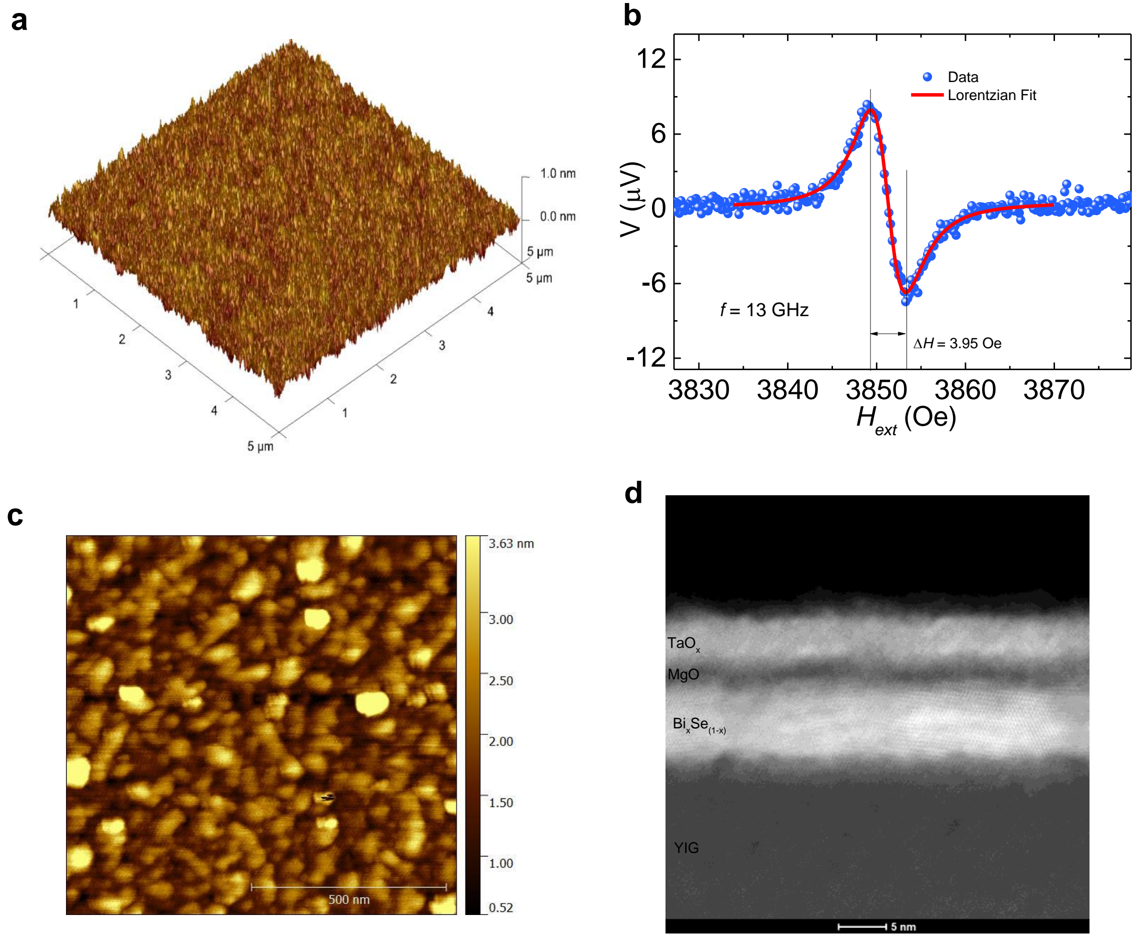

Figure 6.3.1 Characterization of YIG and BS films. (a) and (c) AFM surface images of GGG/YIG (20 nm) and Si/SiO2/MgO (2 nm)/ BS (8 nm) samples, respectively. (b) FMR profile of the GGG/YIG (20 nm) sample. (d) TEM cross-section image of a YIG/BS sample.

Lorentzian trial functions were used to fit the FMR profiles to extract the FMR field and linewidth values. The excitation frequency versus the FMR field was plotted to determine the saturation magnetization using the Kittel formula, $f = \frac{\gamma}{2\pi}\sqrt{H_0(H_0 + 4\pi M_{eff})}$, where γ is the absolute gyromagnetic ratio, H_0 is the FMR field, and M_{eff} is the effective saturation magnetization. The FMR linewidth vs. frequency data were linearly fitted to estimate the Gilbert damping constant (α). The M_{eff} and α were determined to be 139.54 ± 0.24 emu/cc and (1.16 ±

0.14) × 10^{-4}, respectively, for the GGG/YIG (20 nm) film. These values of M_{eff} and α_{int} are comparable to previous reports [157,158]. The high-angle annular dark-field transmission electron microscopy (HAADF-TEM) image of the full stack structure used for the spin-pumping measurements is presented in Figure 6.3.1 (d). The microstructure shows that BS and YIG are polycrystalline. The carrier concentration estimated from Hall measurement was 2.85× 10^{21}/cm^3 with the electrons being the majority carriers in BS (8 nm) film.

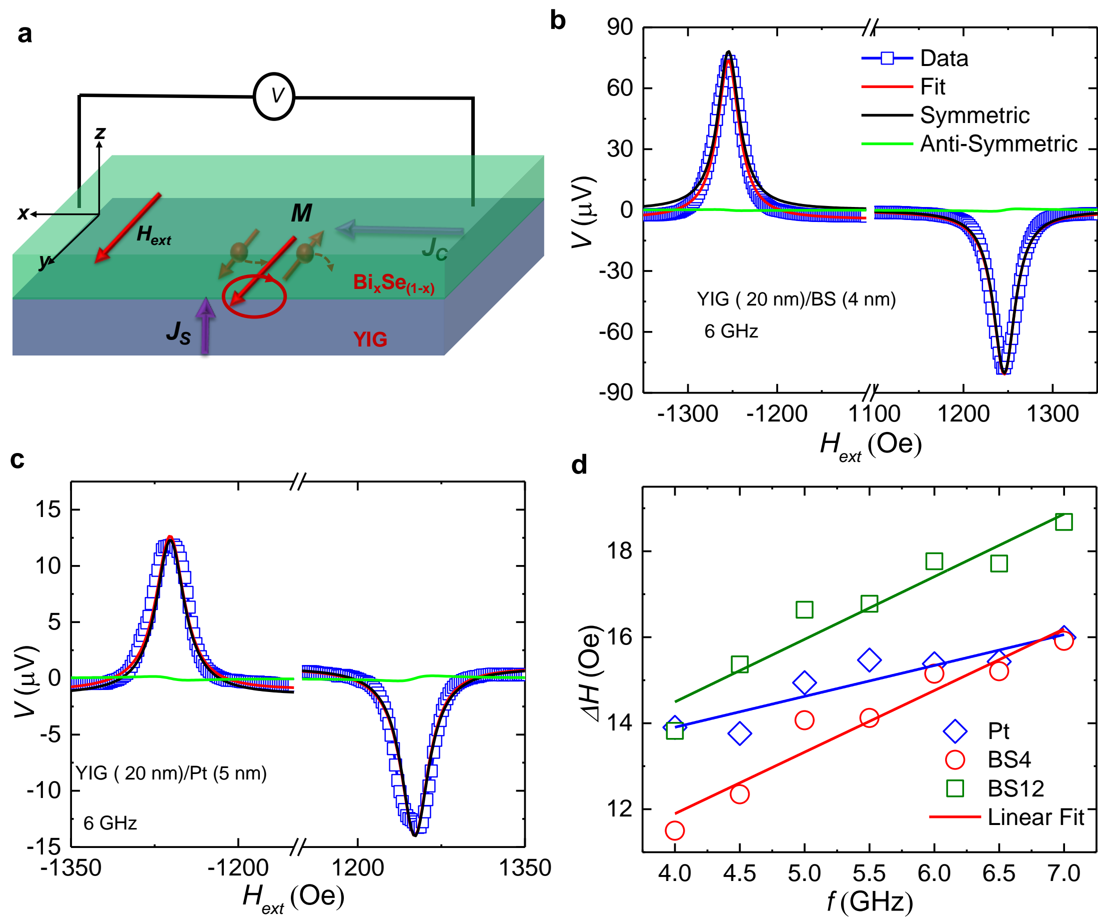

Figure 6.3.2 Spin-to-charge conversion by sputtered BS thin films. (a) Schematic of spin-to-charge conversion (b) and (c) The spin-pumping voltage measured in YBS4 and reference YPt samples at

6 GHz excitation frequency, respectively (d) The line-width as a function of excitation frequency is presented. The red solid line is linear fit to extract α .

The schematics of spin pumping from the YIG layer to the BS layer is as shown in Figure 6.3.2 (a). The rf field drives the magnetization of the YIG into precession at a fixed frequency in the GHz range. At resonance the YIG layer pumps spins to the BS layer and the spin-momentum locking in the BS layer creates non-equilibrium charge accumulation [103,104]. The open circuit voltage build up can be measured by using a nanovoltmeter. Figure 6.3.2 (b) shows the measured open-circuit voltage (*V*) of the YBS4 sample as a function of the external magnetic field (H_{ext}) at an excitation frequency (*f*) of 6 GHz and an excitation amplitude of 1.5 V (~16.53 dBm). Moreover, *V* as a function of H_{ext} presented in Figure 6.3.2 (c) clearly shows sign reversal as H_{ext} changes the sign. This confirms that the *V* originates from spin-to-charge conversion due to some physical mechanism not due to the artifacts. *V* in the YIG/BS spin-pumping is free from the anisotropic magnetoresistance (V_{AMR}) as YIG is an insulating ferrimagnet. The *V* experimental data are fitted to the symmetric and antisymmetric Lorentzians provided in Eqn. (5.3.1). Negligibly small V_A is present in both YBS and YPt samples. Since V_S flips sign when H_{ext} switches direction so this component consists of spin-to-charge voltage due to IEE (V_{IEE}) [87,88,92,100,159] or ISHE [82,84,111]. However, one needs to be careful while referring V_S directly to the IEE or ISHE effects because the inductive coupling between waveguide and the film could generate V_S [159,160]. In our case if there is proximity-induced magnetization it could mix with inductive coupling induced current, which could contribute to V_S . We confirmed there is no proximity-induced magnetism in between YIG and BS by performing anomalous Hall effect and out-of-plane AMR measurements (details in section 6.4). Additionally, Seebeck voltage (V_{SE}) [88,92] attributed to the microwave heating, which is mixed with the V_{IEE} in V_S . V_{SE} has symmetric line-shape but it doesn't change sign as H_{ext} changes sign. We can simply separate V_{IEE} and V_{SE} using

$V_{IEE} = (V_S(+H_0) - V_S(-H_0))/2$ and $V_{SE} = (V_S(+H_0) + V_S(-H_0))/2$ relations. Figure 6.3.2 (c) shows V as a function of H_{ext} at constant excitation amplitude (1.5 V) for the Pt sample. As expected from the ISHE, V flips the sign when the H_{ext} sign is flipped in the Pt sample [84]. ΔH as a function of the f is presented in Figure 6.3.2 (d). Increase in the V as f decreases is consistent with the previous reports [91,136]. α is obtained by using $\Delta H = \Delta_0 + \frac{4\pi}{\sqrt{3}\gamma}\alpha f$ to fit the ΔH versus f data, where Δ_0 corresponds to the contribution of the spatial inhomogeneity present in the YIG film. The α values for the YBS4, YBS8, YBS12, YBS16, and YPt samples are (3.5 ± 0.43), (3.5 ± 0.46), (2.40 ± 0.50), (4.10 ± 0.49), and (1.7 ± 0.33) × 10^{-3}, respectively. Furthermore, the enhancement of the α of the YBS samples as compared to the GGG/YIG value of α ~ (1.16 ± 0.14) × 10^{-4} also corresponds to the spin-to-charge conversion [78]. Moreover, α enhancement can be due to the spin-pumping [78,79], spin-memory loss [115,148,161,162], and interfacial spin-to-charge conversion [26]. Spin-memory loss is significant in case of spin-sink has magnetism including proximity-induced magnetism in between the FM and spin-sink [115,155,162,163]. In our case since there is no proximity-induced magnetism between YIG and BS so the spin-memory loss is less significant. In addition, BS is non-magnetic confirmed by the planar Hall measurement. Further investigation is required to identify contribution of interfacial spin-to-charge conversion such as IREE.

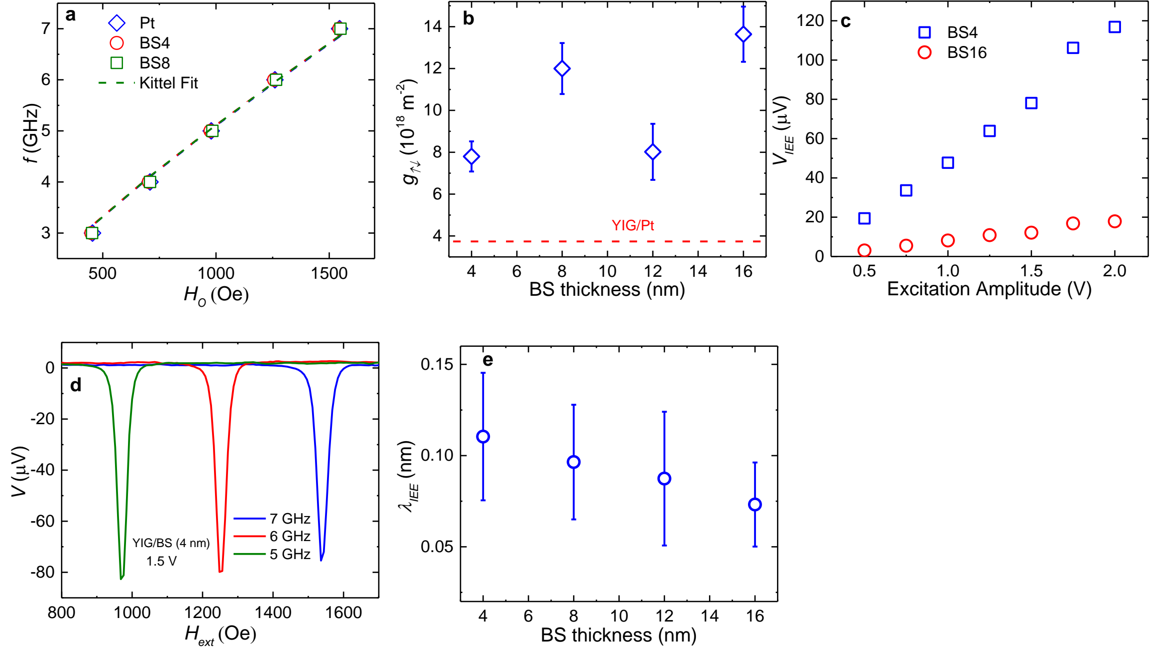

Figure 6.3.3 Characterization of inverse Edelstein effect length (a) Excitation frequency as a function of resonance field fits according to the Kittel formula (b) Spin-mixing conductance of BS samples as a function of BS film thickness. (c) Spin-to-charge conversion voltage as a function of the input excitation amplitude. (d) Spin-pumping voltage as a function of excitation frequency. (e) IEE length as a function of the BS film thickness, which shows thickness dependence.

Figure 6.3.3 (a) shows *f* as a function of H_0. The fit (dotted line) corresponds to the Kittel formula. M_{eff} is estimated to be (185.42 ± 7.42), (187.01 ± 8.28), (185.42 ± 8.71), (183.03 ± 8.02), and (183.83 ± 9.14) emu/cc for YBS4, YBS8, YBS12, YBS16, and YPt samples respectively. Figure 6.3.3 (c) shows V_{IEE} as a function of the excitation amplitude of the YBS4 and YBS16 samples. V_{IEE} as a function of the excitation amplitude is in agreement with our previous reports [87,135]. The *V* as a function of the H_{ext} at different *f* is presented in Figure 6.3.3 (d). As expected, *V* increases with decrease in *f*. $g_{\uparrow\downarrow}$ for YBS samples obtained by using Eqn. (1.8.3) are presented in Figure 6.3.3 (b). $g_{\uparrow\downarrow}$ for YBS samples is more than three times larger than that of the YPt sample. In addition, $g_{\uparrow\downarrow}$ values obtained in our YBS samples are better or comparable to

previously reported values in YIG/ Bi_2Se_3 [91] (~ 8×10^{18} m^{-2}) and YIG/Bi_2Se_3 [147] (~ 2.2×10^{19} m^{-2}), which means sputtered BS is a good spin-sink.

At 6 GHz excitation frequency and 1.5 V excitation amplitude the J_s injected in the YBS4, YBS8, YBS12, YBS16, and YPt samples is 2.63, 3.89, 4.41, 3.34, and 5.12×10^5 A/m^2, respectively. These values of the J_s are estimated by using spin Hall angle of the Pt as 0.07 ± 0.01 and spin-diffusion length 3.4 ± 0.4 nm [115] for the extraction of h_{rf}. h_{rf} for the samples with different conductivities can be different because h_{rf} could be shielded differently. The skin-depth of Pt and BS is 2.30×10^{-6} and 3.98×10^{-5} m, respectively, which is much larger than the film thickness so h_{rf} is same for YPt and YBS samples given that the input power is same. Note that the value of spin Hall angle of Pt 0.07 ± 0.01 is obtained by performing independent spin-torque ferromagnetic resonance on Pt (5 nm)/NiFe (6 nm) sample [45]. This value of spin Hall angle of Pt is comparable to the previous reports [45,115,141]. The efficiency of the spin-to-charge conversion for the IEE is given by [26,104]: $\lambda_{IEE} = \frac{J_C}{J_s} = \frac{V_{IEE}}{RwJ_s}$, where R and w are the resistance and width of the device, respectively. The V_{IEE} , R, and w for the BS4 sample are 79.29 μV, 4400 Ω, and 620 μm, respectively. λ_{IEE} for the YBS4 sample is estimated to be (0.11± 0.03) nm. This value of λ_{IEE} is more than three times larger than reported in YIG/CBS (0.035 nm) [91] and more than an order of magnitude than in YIG/Bi/Ag (0.01 nm) [95]. λ_{IEE} as a function of the BS is presented in Figure 6.3.3 (e). The error bars in λ_{IEE} are determined by incorporating errors in h_{rf} , $g_{\uparrow\downarrow}$, and α . λ_{IEE} shows BS thickness dependence, which is in agreement with the figure-of-merit of charge-to-spin conversion as a function of BS thickness as shown in chapter 3. Unlike the thickness dependence in the case of HMs, in BS λ_{IEE} is correlated with the size of grains present in the BS films. It should be noted that as thickness of the BS increases the grain size also increases demonstrated by TEM presented in chapter 3. In case of crystalline bismuth selenide, λ_{IEE} first increases and it remained

constant after certain thickness whereas in BS it has shown thickness dependence [91]. We also estimated the momentum relaxation time (τ_m) in the surface states of YBS8 sample using relation [26,33,103] $\lambda_{IEE} = v_f \tau_m$, where v_f is Fermi velocity. v_f for BS (8 nm) film is estimated to be 3.38×10^6 m/s. Using λ_{IEE} of YBS8 sample 0.96 nm, τ_m is determined to be 2.84×10^{-16} S, which is an order of magnitude shorter compared to the previous reports on TIs and Rashba interfaces [33,99,138] but comparable to Cu/Bi [139] interface.

6.4 Absence of proximity-induced magnetism in YIG/BS

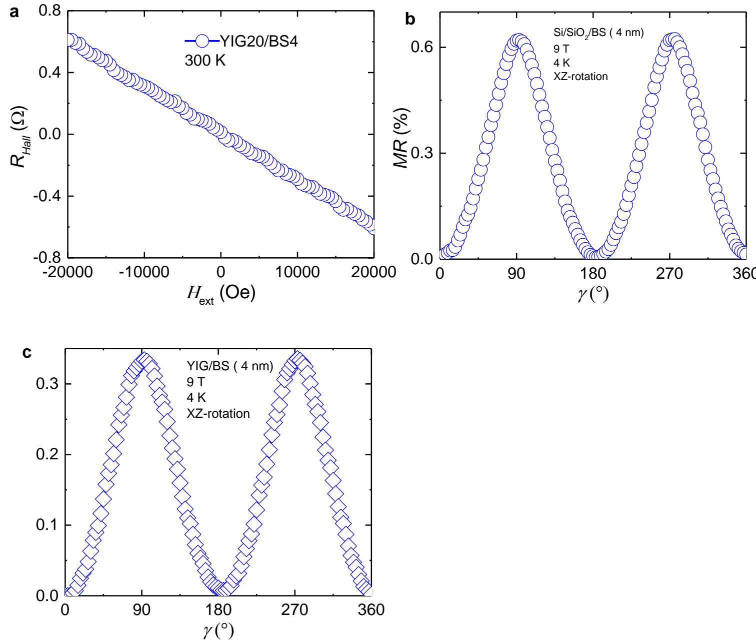

Figure 6.4.1 (a) Hall resistance of YIG/BS at room temperature. (b) Out-of-plane AMR of Si/SiO2/BS (4 nm). (c) Out-of-plane AMR of YIG/BS (4 nm).

We measured anomalous Hall effect at 300 K and out-of-plane anisotropic magneto-resistance (AMR) in YIG/BS (4 nm) sample and a control sample Si/SiO_2/BS (4 nm) at 4 K to see if there is any proximity-induced magnetism between the YIG and BS layer. The anomalous Hall measurement that is presented in Figure 6.4.1 (a) shows the linear Hall resistance as a function of the out-of-plane field. If there was any proximity-induced magnetism, the Hall resistance would

have saturated at the field equivalent to $4\pi Ms$. However, the Hall resistance remains linear as a function of out-of-plane magnetic field. In addition, the out-of-plane AMR measurement was performed by measuring the longitudinal resistance while rotating the field in *xz* plane. The results are presented in Figure 6.4.1 (b) and (c). At 4 K (where the signal level is the highest) under exactly identical experimental set up, out-of-plane AMR in YIG/BS and Si/SiO_2/BS is determined to be ~0.35% and 0.6%, respectively. If there was any proximity effect between the YIG and BS layer, the out-of-plane magnetoresistance should be larger in YIG/BS sample than that in Si/SiO_2/BS sample. At room temperature one would expect a reduced magnetic-proximity effect compared to that at lower temperatures. From Hall and AMR measurements, we can confirm that there is no sizeable magnetic-proximity effect involved in between YIG and BS layers.

6.5 Discussion

Shiomi et al., reported λ_{IEE} value of 0.1 nm due to the IEE in bulk insulating $Bi_{1.5}Sb_{0.5}Te_{1.7}$ and at 15 K [88]. Jamali et al., and Deorani et al., reported room temperature spin-to-charge conversion by CBS due to the ISHE and IEE [87,111]. Jamali et al., performed magnetization precession cone angle measurement to confirm contribution of ISHE in the spin-to-charge conversion by CBS but did not separate contributions of each effects. Deorani et al., separated contributions from ISHE and IEE by assuming surface state thickness of the CBS to be 3 nm. Wang et al., observed spin-to-charge conversion in YIG/CBS mainly due to the IEE and the estimated value of λ_{IEE} is as large as 0.035 nm at room temperature. From these aforementioned reports on spin-to-charge conversion by CBS there is contribution from both IEE and ISHE. In our YIG/BS samples there could be contribution from both ISHE, IEE, and IREE. In order to investigate contributions from IEE and ISHE, we analyze $g_{\uparrow\downarrow}$ as a function of BS thickness. $g_{\uparrow\downarrow}$ as a function of BS thickness (Figure 6.3.3 (b)) does not show any pattern as a function of BS film thickness. Our BS thickness dependence of $g_{\uparrow\downarrow}$ agrees with the previous reports, which claim IEE as their main mechanism for the spin-to-charge conversion [91,147]. However, in case of HM/FM

system on which ISHE is dominant mechanism for spin-to-charge conversion $g_{\uparrow\downarrow}$ increases as HM film thickness increases because spin-back flow in thicker films decreases [79,147–149]. $g_{\uparrow\downarrow}$ as a function of BS film thickness behavior indicates that in our YIG/BS samples, the main mechanism for spin-to-charge conversion is IEE rather than ISHE. In addition, $g_{\uparrow\downarrow}$ in BS/CoFeB (presented in chapter 5) also shows similar behavior as in the case of YIG/BS. Furthermore, $g_{\uparrow\downarrow}$ is independent of YIG thickness [164]. In case of proximity-induced magnetism between ferromagnet and spin-sink $g_{\uparrow\downarrow}$ as a function of spin-sink thickness can quickly saturate [115,160,162]. The largest reported values of Pt and Pd thickness after which $g_{\uparrow\downarrow}$ saturates even in the presence of proximity-induced magnetism are 3 and 5 nm, respectively [161]. We anticipate that $g_{\uparrow\downarrow}$ as a function of BS thickness may not saturate below 4 nm as there is no proximity-induced magnetism. A further investigation of spin memory loss is required YIG/BS. In BS/CoFeB presented in chapter 5, $g_{\uparrow\downarrow}$ did not depend upon BS thickness where much wider range of BS film thickness (2 nm-16 nm) was investigated. Now the question arises why sputtered BS films do have higher λ_{IEE} as compared to MBE grown CBS [91,111]? As the thickness of the films reaches nano-scale, electrons can move freely in two dimensions, but electronic motion is confined along the normal to the film plane. Confinement quantizes the wavefunction of the electron. Consequently, electronic properties of the material change drastically. In the case of sputtered BS, from the AFM and TEM images we can clearly see grains of nano-meter scale. In these nano-sized grains the electronic motion is confined along three dimensions. In chapter 4, we performed numerical simulations to study the effect of the grain size effect on the charge-to-spin conversion and found that the charge-to-spin conversion is largely influenced by grain size effect. There are additional discrete bands present in case of ~ 10 nm scale grains compared to triangular crystals present in MBE grown TI films. Note that in case of crystalline TI films confinement is only along the normal of the film plane. The additional discrete bands present in grains of BS, due to QC, contribute to the spin-momentum locking. In the case of

spin-to-charge conversion λ_{IEE} shows BS film thickness dependence and it has larger value than that of the CBS film, which confirms that the spin-to-charge conversion in BS films is also influenced by QC in the grains of BS film.

Chapter 7. Conclusions and outlook

SOT has been intensely studied in the past few years after the idea of using it to write data bits in the memory device SOT-MRAM. Primarily 5d and 3d transition metals, semiconductors, 2D materials, and recently TIs interfaced with the FMs for the study of SOT [53,68,69,165]. Switching of perpendicular magnet was achieved via SOT with the current density of the order of ~ 10^6-10^7 A/cm^2 from HMs. The switching of a magnetically doped perpendicular TI $(Cr_{0.08}Bi_{0.54}Sb_{0.38})_2Te_3$ layer at 1.9 K has been observed via the SOT from the TI, but with a much lower current density 8.9×10^4 A/cm^2 [66]. At room temperature, switching of perpendicular MnGa and CoTb via SOT from TIs has been demonstrated with current density ~10^6 A/cm^2 and large external magnetic field (~kOe) [75,77]. One of the key factors for widespread realization of SOT-based spintronic devices is the development of a spin-channel with high spin-density generation efficiency and growth process is compatible with the industry. In addition, growth and switching of state-of-art perpendicular magnet CoFeB is also necessary to integrate immediately in the current technology. Furthermore, the replacement of a conducting FM by an insulating FM avoids waste of current through the conducting FM [72,73]. This leads to a low magnetization switching current density and stops degradation of conducting FM due to electromigration. Another way of lowering down current shunting effect is by using highly conductive spin source.

The main disadvantages of SOT switching of a perpendicular FM are the need of an external magnetic field and large magnetization switching current density. Recently, the external field requirement for deterministic switching of a perpendicular FM via the SOT is removed by the in-plane exchange bias from an antiferromagnetic material [114,166]. Furthermore, by using bilayers of opposite spin Hall angle spin-source perpendicular spin-polarization is generated, which can switch a perpendicular FM without an external field [167]. Moreover, the interfacial SOT can also generate a perpendicular spin-polarization, which can switch the perpendicular FM without an external magnetic field [168].

In chapter 3 of this thesis, we demonstrated the growth of smooth BS films on a large silicon wafer with two orders of magnitude larger θ_S compared to HMs using a semiconductor industry compatible sputtering process. These films possess comparable or better σ_S compared to other reported spin-density generators at room temperature [2,46,65,75,76,110]. The poly-crystalline nature of the sputtered BS films was found and confirmed by quantum transport simulations to be the key for the high SOT due to the quantum confinement effect. Furthermore, we developed and switched a perpendicular CoFeB multilayer on BS films at room temperature by a TI material, which enables a path for reliable and efficient beyond-CMOS devices. The SOT switching of the state-of-art FM CoFeB with an order of magnitude smaller switching power dissipation compared to HMs and TIs makes sputtered BS an excellent candidate for the spin-channel in SOT-MRAM.

In chapter 5 of this thesis, we presented spin-to-charge conversion by sputtered BS thin films in BS/CoFeB heterostructure at room temperature. The spin-to-charge conversion voltage in BS/CoFeB is more than four times larger than the Pt/CoFeB. The figure-of-merit of spin-to charge conversion in BS (2 nm)/CoFeB (5 nm) is estimated to be as large as 0.32 nm. This value of the λ_{IEE} is larger than the reported values in other TIs such as 0.1 nm in $Bi_{1.5}Sb_{0.5}Te_{1.7}$ [88] and 0.075 nm in $(Bi_{0.22}Sb_{0.78})_2Te_3$ [90]. λ_{IEE} shows thickness dependence similar to the θ_S thickness dependence. We also investigated the MgO insertion layer to identify if there is thermal effect present in the spin-pumping signal. Insertion layer of a 1 nm almost completely suppressed the spin-to-charge voltage, which means negligible thermal effect is present in spin-pumping signal of BS/CoFeB. The logic device MESO, which uses spin-to-charge conversion voltage for detection of the magnetization requires high output voltage for its operation [129]. The insertion of 2 nm Ag layer (BS/Ag/CoFeB) enhanced spin-to-charge voltage by approximately 40% due to the additional spin-momentum locking originated from the Rashba potential at the interface between BS and Ag. The successful sputtered growth of the BS on silicon substrates makes for easier integration into

complementary metal oxide semiconductor (CMOS) devices and high spin-to-charge conversion can be utilized for the reading scheme in the MESO device.

In chapter 6 of this thesis, we demonstrated spin-to-charge conversion in YIG/BS. Ferrimagnetic insulator YIG avoids artifacts such as self spin-pumping, planar Hall effect present due to the conducting FM. In addition, the low damping constant compared to conducting FM makes YIG useful candidate for future spintronics device application. For the application point of view, it is important to have large spin-to-charge conversion voltage as well as a widely used growth technique. BS is grown by a magneton sputtering technique and we observed more than five times large spin-to-charge voltage at room temperature in YIG/BS (4 nm) compared to YIG/Pt. High spin-to-charge conversion makes sputtered BS a good choice for the practical applications in logic devices such as MESO. λ_{IEE} value of sputtered YIG/BS (4 nm) is three times larger than that of YIG/Bi_2Se_3 [91]. λ_{IEE} shows BS thickness dependence in YIG/BS, which is consistent with the BS thickness dependence of λ_{IEE} in BS/CoFeB.

Overall, in this thesis, efficient charge-to-spin and spin-to-charge convertor was developed, which can be grown by industry compatible technique. In addition, quantum confinement effect was also observed in nanoscale grains present in BS films. The reported preliminary results of poly-crystalline BS in this study has not been optimized, and we expect future development, such as exploring different crystalline orientations or chemical compositions, would see further improvement. In addition, another challenge could be keeping properties of BS intact after necessary thermal treatment above 300˚C for the integration into the current technology.

References

[1] M. Cubukcu, O. Boulle, M. Drouard, K. Garello, C. Onur Avci, I. Mihai Miron, J. Langer, B. Ocker, P. Gambardella, and G. Gaudin, Appl. Phys. Lett. **104**, 042406 (2014).

[2] R. A. Liu, L Pai, Chi-Feng Li, Y. Tseng, H. W. Ralph, D. C. Buhrman, Science **336**, 555 (2012).

[3] S. Manipatruni, D. E. Nikonov, and I. A. Young, Appl. Phys. Express **7**, 103001 (2014).

[4] K. L. Wang, J. G. Alzate, and P. Khalili Amiri, J. Phys. D. Appl. Phys. **46**, 074003 (2013).

[5] A. A. Tulapurkar, Y. Suzuki, A. Fukushima, H. Kubota, H. Maehara, K. Tsunekawa, D. D. Djayaprawira, N. Watanabe, and S. Yuasa, Nature **438**, 339 (2005).

[6] D. C. Ralph and M. D. Stiles, J. Magn. Magn. Mater. **320**, 1190 (2008).

[7] A. Brataas and K. M. D. Hals, Nat. Nanotechnol. **9**, 86 (2014).

[8] C. F. Pai, L. Liu, Y. Li, H. W. Tseng, D. C. Ralph, and R. A. Buhrman, Appl. Phys. Lett. **101**, 122404 (2012).

[9] A. Soumyanarayanan, N. Reyren, A. Fert, and C. Panagopoulos, Nature **539**, 509 (2016).

[10] C. Chappert, A. Fert, and F. N. Van Dau, Nat. Mater. **6**, 813 (2007).

[11] S. S. P. Parkin, C. Kaiser, A. Panchula, P. M. Rice, B. Hughes, M. Samant, and S.-H. Yang, Nat. Mater. **3**, 862 (2004).

[12] S. Ikeda, K. Miura, H. Yamamoto, K. Mizunuma, H. D. Gan, M. Endo, S. Kanai, J. Hayakawa, F. Matsukura, and H. Ohno, Nat. Mater. **9**, 721 (2010).

[13] J. E. Hirsch, Phys. Rev. Lett. **9**, 1834 (1999).

[14] M. I. Dyakonov and V. I. Perel, Phys. Lett. A **35**, 459 (1971).

[15] G. Y. Guo, S. Murakami, T.-W. Chen, and N. Nagaosa, Phys. Rev. Lett. **100**, 096401(2007).

[16] Y. K. Kato, R. C. Myers, A. C. Gossard, and D. D. Awschalom, *Science* **306**, 1910 (2004).

[17] S. O. Valenzuela and M. Tinkham, Nature **442**, 176 (2006).

[18] T. Kimura, Y. Otani, T. Sato, S. Takahashi, and S. Maekawa, (2007).

[19] M. Morota, Y. Niimi, K. Ohnishi, D. H. Wei, T. Tanaka, H. Kontani, T. Kimura, and Y. Otani, Phys. Rev. B - Condens. Matter Mater. Phys. **83**, 1 (2011).

[20] Y. Niimi, Y. Kawanishi, D. H. Wei, C. Deranlot, H. X. Yang, M. Chshiev, T. Valet, A. Fert, and Y. Otani, Phys. Rev. Lett. **109**, 1 (2012).

[21] Y. Wen, J. Wu, P. Li, Q. Zhang, Y. Zhao, A. Manchon, J. Q. Xiao, and X. Zhang, Phys. Rev. B **95**, 104403 (2017).

[22] H. Kurebayashi, J. Sinova, D. Fang, A. C. Irvine, T. D. Skinner, J. Wunderlich, V. Novák, R. P. Campion, B. L. Gallagher, E. K. Vehstedt, L. P. Zârbo, K. Výborný, A. J. Ferguson, and T. Jungwirth, Nat. Nanotechnol. **9**, 211 (2014).

[23] A. Manchon, H. C. Koo, J. Nitta, S. M. Frolov, and R. A. Duine, Nat. Mater. **14**, 871 (2015).

[24] B. Y. A. and R. E. I., J. Phys. C **17**, 6039 (1984).

[25] S. D. Ganichev, S. N. Danilov, P. Schneider, V. V Bel'kov, L. E. Golub, W. Wegscheider, D. Weiss, and W. Prettl, J. Magn. Magn. Mater. **300**, 127 (2006).

[26] J. C. Rojas Sánchez, L. Vila, G. Desfonds, S. Gambarelli, J. P. Attané, J. M. De Teresa, C. Magén, and & A. Fert, Nat. Commun. **4**, 2944 (2013).

[27] I. M. Miron, G. Gaudin, S. Auffret, B. Rodmacq, A. Schuhl, S. Pizzini, J. Vogel, and P.

Gambardella, Nat. Mater. **9**, 230 (2010).

[28] Q. Shao, G. Yu, Y.-W. Lan, Y. Shi, M.-Y. Li, C. Zheng, X. Zhu, L.-J. Li, K. Amiri, and K. L. Wang, Nano Lett. **16**, 7514 (2016).

[29] Y. M. Koroteev, G. Bihlmayer, J. E. Gayone, E. V Chulkov, S. Blügel, P. M. Echenique, and P. Hofmann, Phys. Rev. Lett. **93**, 046403 (2004).

[30] C. R. Ast, J. Henk, A. Ernst, L. Moreschini, M. C. Falub, D. Pacilé, P. Bruno, K. Kern, and M. Grioni, Phys. Rev. Lett. **98**, 186807 (2007).

[31] J. H. Dil, F. Meier, J. Lobo-Checa, L. Patthey, G. Bihlmayer, and J. Osterwalder, Phys. Rev. Lett. **101**, 266802 (2008).

[32] V. M. Edelstein, Solid State Commun. **73**, 233 (1990).

[33] J.-C. Rojas-Sánchez, S. Oyarzún, Y. Fu, A. Marty, C. Vergnaud, S. Gambarelli, L. Vila, M. Jamet, Y. Ohtsubo, A. Taleb-Ibrahimi, P. Le Fèvre, F. Bertran, N. Reyren, J.-M. George, and A. Fert, Phys. Rev. Lett. **116**, 096602 (2016).

[34] M. Z. Hasan and C. L. Kane, Rev. Mod. Phys. **82**, 3045 (2010).

[35] X.-L. Qi and S.-C. Zhang, Rev. Mod. Phys. **83**, 1057 (2011).

[36] K. V Klitzing, G. Dorda, and M. Pepper, *Phys. Rev. Lett.* **45**, 494 (1980).

[37] H. Zhang, C.-X. Liu, X.-L. Qi, X. Dai, Z. Fang, and S.-C. Zhang, Nat. Phys. **5**, 438 (2009).

[38] Y. Xia, D. Qian, D. Hsieh, L. Wray, A. Pal, H. Lin, A. Bansil, D. Grauer, Y. S. Hor, R. J. Cava, and M. Z. Hasan, Nat. Phys. **5**, 398 (2009).

[39] P. Roushan, J. Seo, C. V. Parker, Y. S. Hor, D. Hsieh, D. Qian, A. Richardella, M. Z. Hasan, R. J. Cava, and A. Yazdani, Nature **460**, 1106 (2009).

[40] A. Manchon and S. Zhang, Phys. Rev. B **79**, 094422 (2009).

[41] T. Valet and A. Fert, *Phys. Rev. B* **48***,* 7099(1993).

[42] J. Xiao, A. Zangwill, and M. D. Stiles, Eur. Phys. J. B **59**, 415 (2007).

[43] P. M. Haney, H.-W. Lee, K.-J. Lee, A. Manchon, and M. D. Stiles, Phys. Rev. B **87**, 174411 (2013).

[44] K. Ando, S. Takahashi, K. Harii, K. Sasage, J. Ieda, S. Maekawa, E. Saitoh, W. S. θ J Ni, and P. M. J, Phys. Rev. Lett. **101**, 036601 (2008).

[45] L. Liu, T. Moriyama, D. C. Ralph, and R. A. Buhrman, Phys. Rev. Lett. **106**, 036601 (2011).

[46] W. Zhang, W. Han, X. Jiang, S.-H. Yang, and S. S. P. Parkin, Nat. Phys. **11**, 496 (2015).

[47] J. Kim, J. Sinha, M. Hayashi, M. Yamanouchi, S. Fukami, T. Suzuki, S. Mitani, and H. Ohno, Nat. Mater. **12**, 240 (2013).

[48] C. Zhang, M. Yamanouchi, H. Sato, S. Fukami, S. Ikeda, F. Matsukura, and H. Ohno, Appl. Phys. Lett. **103**, 2013 (2013).

[49] K. Garello, I. M. Miron, C. O. Avci, F. Freimuth, Y. Mokrousov, S. Blügel, S. Auffret, O. Boulle, G. Gaudin, and P. Gambardella, Nat. Nanotechnol. **8**, 587 (2013).

[50] C. O. Avci, K. Garello, C. Nistor, S. Godey, B. Ballesteros, A. Mugarza, A. Barla, M. Valvidares, E. Pellegrin, A. Ghosh, I. M. Miron, O. Boulle, S. Auffret, G. Gaudin, and P. Gambardella, Phys. Rev. B **89**, 214419 (2014).

[51] Q. Hao and G. Xiao, Phys. Rev. Appl. **3**, 34009 (2015).

[52] R. Ramaswamy, X. Qiu, T. Dutta, S. D. Pollard, and H. Yang, Appl. Phys. Lett **108**, 202406 (2016).

[53] A. Ghosh, K. Garello, O. Avci, M. Gabureac, and P. Gambardella, Phys. Rev. Appl. **7**, 014004 (2017).

[54] M. Kawaguchi, K. Shimamura, S. Fukami, F. Matsukura, H. Ohno, T. Moriyama, D. Chiba, and T. Ono, Appl. Phys. Express **6**, 113002 (2013).

[55] M. Jamali, Z. Zhao, M. DC, D. Zhang, H. Li, A. K. Smith, and J. P. Wang, J. Appl. Phys. **119**, 133902 (2016).

[56] C. O. Avci, K. Garello, M. Gabureac, A. Ghosh, A. Fuhrer, S. F. Alvarado, and P. Gambardella, Phys. Rev. B **90**, 224427 (2014).

[57] J. Kim, J. Sinha, S. Mitani, M. Hayashi, S. Takahashi, S. Maekawa, M. Yamanouchi, and H. Ohno, Phys. Rev. B - Condens. Matter Mater. Phys. **89**, 174424 (2014).

[58] M. Isasa, E. Villamor, L. E. Hueso, M. Gradhand, and F. Casanova, Phys. Rev. B **91**, 024402 (2015).

[59] X. Qiu, P. Deorani, K. Narayanapillai, K.-S. Lee, K.-J. Lee, H.-W. Lee, and H. Yang, Sci. Rep. **4**, 4491 (2014).

[60] A. Chernyshov, M. Overby, X. Liu, J. K. Furdyna, Y. Lyanda-Geller, and L. P. Rokhinson, Nat. Phys. **5**, 10 (2008).

[61] L. Chen, M. Decker, M. Kronseder, R. Islinger, M. Gmitra, D. Schuh, D. Bougeard, J. Fabian, D. Weiss, and C. H. Back, Nat. Commun. **7**, 13802 (2016).

[62] Y. Wang, R. Ramaswamy, M. Motapothula, K. Narayanapillai, D. Zhu, J. Yu, T. Venkatesan, and H. Yang, Nano Lett **17**, 7659 (2017).

[63] W. Zhang, J. Sklenar, B. Hsu, W. Jiang, M. B. Jungfleisch, J. Xiao, F. Y. Fradin, Y. Liu, J. E. Pearson, J. B. Ketterson, Z. Yang, A. Hoffmann, APL Mater. **4**, 032302 (2016).

[64] M. H. D. Guimarã, G. M. Stiehl, D. Macneill, N. D. Reynolds, and D. C. Ralph, Nano Lett. (2018).

[65] A. R. Mellnik, J. S. Lee, A. Richardella, J. L. Grab, P. J. Mintun, M. H. Fischer, A. Vaezi, A. Manchon, E. A. Kim, N. Samarth, and D. C. Ralph, Nature **511**, 449 (2014).

[66] Y. Fan, P. Upadhyaya, X. Kou, M. Lang, S. Takei, Z. Wang, J. Tang, L. He, L. Chang, M. Montazeri, G. Yu, W. Jiang, T. Nie, R. N. Schwartz, Y. Tserkovnyak, and K. L. Wang, Nat. Mater. **13**, 699 (2014).

[67] K. Kondou, R. Yoshimi, A. Tsukazaki, Y. Fukuma, J. Matsuno, K. S. Takahashi, M. Kawasaki, Y. Tokura, and Y. Otani, Nat. Phys. **12**, 1027 (2016).

[68] I. M. Miron, K. Garello, G. Gaudin, P.-J. Zermatten, M. V Costache, S. Auffret, S. Bandiera, B. Rodmacq, A. Schuhl, and P. Gambardella, Nature **476**, 189 (2011).

[69] L. Liu, O. J. Lee, T. J. Gudmundsen, D. C. Ralph, and R. A. Buhrman, Phys. Rev. Lett. **109**, 096602 (2012).

[70] Q. Hao and G. Xiao, Phys. Rev. Appl. **3**, 034009 (2015).

[71] R. Yoshimi, K. Yasuda, A. Tsukazaki, K. S. Takahashi, M. Kawasaki, and Y. Tokura, Sci. Adv. **4**, eaat9989 (2018).

[72] C. O. Avci, A. Quindeau, C.-F. Pai, M. Mann, L. Caretta, A. S. Tang, M. C. Onbasli, C. A. Ross, and G. S. D. Beach, Nat. Mater. **16**, 309 (2016).

[73] P. Li, T. Liu, H. Chang, A. Kalitsov, W. Zhang, G. Csaba, W. Li, D. Richardson, A. DeMann, G. Rimal, H. Dey, J. S. Jiang, W. Porod, S. B. Field, J. Tang, M. C. Marconi, A. Hoffmann, O. Mryasov, and M. Wu, Nat. Commun. **7**, 12688 (2016).

[74] S. Fukami, T. Anekawa, C. Zhang, and H. Ohno, Nat. Nanotechnol. | **11**, 621 (2016).

[75] J. Han, A. Richardella, S. A. Siddiqui, J. Finley, N. Samarth, and L. Liu, Phys. Rev. Lett. **119**, 077702 (2017).

[76] Y. Wang, D. Zhu, Y. Y. Wu, Y. Yang, J. Yu, R. Ramaswamy, R. Mishra, S. Shi, M. Elyasi, K.-L. Teo, Y. Y. Wu, and H. Yang, Nat. Commun. **8**, 1364 (2017).

[77] N. Khang, D. Khang, Y. Ueda, and P. N. Hai, Nat. Mater. **17**, 808(2018).

[78] Y. Tserkovnyak, A. Brataas, and G. E. W. Bauer, Phys. Rev. Lett. **88,** 117601(2002).

[79] Y. Tserkovnyak, A. Brataas, G. E. W. Bauer, and B. I. Halperin, *Rev. of Mod. Phys.* **77**, 1305(2005).

[80] E. Saitoh, M. Ueda, H. Miyajima, and G. Tatara, Appl. Phys. Lett **88**, 182509 (2006).

[81] H. L. Wang, C. H. Du, Y. Pu, R. Adur, P. C. Hammel, and F. Y. Yang, Phys. Rev. Lett. **112**, 197201 (2014).

[82] O. Mosendz, J. E. Pearson, F. Y. Fradin, G. E. W. Bauer, S. D. Bader, and A. Hoffmann, Phys. Rev. Lett. **104**, 046601 (2010).

[83] K. Ando and E. Saitoh, J. Appl. Phys. **108**, 113925 (2010).

[84] K. Ando, S. Takahashi, J. Ieda, Y. Kajiwara, H. Nakayama, T. Yoshino, K. Harii, Y. Fujikawa, M. Matsuo, S. Maekawa, and E. Saitoh, J. Appl. Phys. **109**, 103913 (2011).

[85] K. Ando and E. Saitoh, Nat. Commun. **3**, 629 (2012).

[86] C. Liu, S. J. Patel, T. A. Peterson, C. C. Geppert, K. D. Christie, G. Stecklein, C. J. Palmstrøm, and P. A. Crowell, Nat. Commun. **7**, 10296 (2016).

[87] M. Jamali, J. S. Lee, J. S. Jeong, F. Mahfouzi, Y. Lv, Z. Zhao, B. K. Nikolic, K. A. Mkhoyan, N. Samarth, and J. P. Wang, Nano Lett. **15**, 7126 (2015).

[88] Y. Shiomi, K. Nomura, Y. Kajiwara, K. Eto, M. Novak, K. Segawa, Y. Ando, and E.

Saitoh, Phys. Rev. Lett. **113**, 196601 (2014).

[89] K. T. Yamamoto, Y. Shiomi, K. Segawa, Y. Ando, and E. Saitoh, Phys. Rev. B **94**, (2016).

[90] J. B. S. Mendes, O. A. Santos, J. Holanda, R. P. Loreto, C. I. L. De Araujo, C.-Z. Chang, J. S. Moodera, A. Azevedo, and S. M. Rezende, Phys. Rev. B **96**, 180415(R) (2017).

[91] H. Wang, J. Kally, J. S. Lee, T. Liu, H. Chang, D. R. Hickey, K. A. Mkhoyan, M. Wu, A. Richardella, and N. Samarth, Phys. Rev. Lett. **117**, 076601 (2016).

[92] Q. Song, J. Mi, D. Zhao, T. Su, W. Yuan, W. Xing, Y. Chen, T. Wang, T. Wu, X. H. Chen, X. C. Xie, C. Zhang, J. Shi, and W. Han, Nat. Commun. **7**, 13485 (2016).

[93] A. A. Baker, A. I. Figueroa, L. J. Collins-Mcintyre, G. Van Der Laan, and & T. Hesjedal, Sci. Rep. **5**, 7907 (2015).

[94] Z. Jiang, C.-Z. Chang, M. R. Masir, C. Tang, Y. Xu, J. S. Moodera, A. H. Macdonald, and J. Shi, Nat. Commun. **7**, 11458 (2016).

[95] M. Matsushima, Y. Ando, S. Dushenko, R. Ohshima, R. Kumamoto, T. Shinjo, and M. Shiraishi, Appl. Phys. Lett **110**, 072404 (2017).

[96] W. Zhang, M. B. Jungfleisch, W. Jiang, J. E. Pearson, and A. Hoffmann, J. Appl. Phys. **117**, 17C727 (2015).

[97] S. Oyarzún, A. K. Nandy, F. Rortais, J.-C. Rojas-Sánchez, M.-T. Dau, P. Noël, P. Laczkowski, S. Pouget, H. Okuno, L. Vila, C. Vergnaud, C. Beigné, A. Marty, J.-P. Attané, S. Gambarelli, J.-M. George, H. Jaffrè, S. Blügel, and & M. Jamet, Nat. Commun. **7**, 13857 (2016).

[98] H. Tsai, S. Karube, K. Kondou, N. Yamaguchi, F. Ishii, and Y. Otani, Sci. Reports **8**, 5564

(2018).

[99] E. Lesne, Y. Fu, S. Oyarzun, J. C. Rojas-Sánchez, D. C. Vaz, H. Naganuma, G. Sicoli, J. Attané, M. Jamet, E. Jacquet, J. George, A. Barthélémy, H. Jaarès, A. Fert, M. Bibes, and L. Vila, Nat. Mater. **15**, 1261 (2016).

[100] Q. Song, H. Zhang, T. Su, W. Yuan, Y. Chen, W. Xing, J. Shi, J. Sun, and Wei Han, Sci. Adv. **3**, 1602312 (2017).

[101] J. B. S. Mendes, O. A. Santos, L. M. Meireles, R. G. Lacerda, L. H. Vilela-Leão, F. L. A. Machado, R. L. Rodríguez-Suárez, A. Azevedo, and S. M. Rezende, Phys. Rev. Lett. **115**, 226601 (2015).

[102] S. Dushenko, H. Ago, K. Kawahara, T. Tsuda, S. Kuwabata, T. Takenobu, T. Shinjo, Y. Ando, and M. Shiraishi, Phys. Rev. Lett. **116**, 166102 (2016).

[103] K. Shen, G. Vignale, and R. Raimondi, Phys. Rev. Lett. **112**, 096601 (2014).

[104] S. Zhang and A. Fert, Phys. Rev. B **94**, 184423 (2016).

[105] Http://Www.Semicore.Com.

[106] U. Maver, T. Velnar, M. Gaberšček, O. Planinšek, and M. Finšgar, Trends Anal. Chem. **80**, 96 (2016).

[107] J. C. Slonczewski, J. Magn. Magn. Mater. **159**, L1 (1996).

[108] W. J. Xu, B. Zhang, Z. Wang, S. S. Chu, W. Li, Z. B. Wu, R. H. Yu, and X. X. Zhang, Eur. Phys. J. B **65**, 233 (2008).

[109] C. Şahin and M. E. Flatté, Phys. Rev. Lett. **114**, 107201 (2015).

[110] Y. Wang, P. Deorani, K. Banerjee, N. Koirala, M. Brahlek, S. Oh, and H. Yang, Phys. Rev. Lett. **114**, 257202 (2015).

[111] P. Deorani, J. Son, K. Banerjee, N. Koirala, M. Brahlek, S. Oh, and H. Yang, Phys. Rev. B **90**, 094403 (2014).

[112] T. Devolder, P.-H. Ducrot, J.-P. Adam, I. Barisic, N. Vernier, J.-V. Kim, B. Ockert, and D. Ravelosona, Appl. Phys. Lett. **102**, 022407 (2013).

[113] Z. Zhao, M. Jamali, A. K. Smith, and J. P. Wang, Appl. Phys. Lett. **106**, 132404 (2015).

[114] J.-Y. Chen, M. DC, D. Zhang, Z. Zhao, M. Li, and J.-P. Wang, Appl. Phys. Lett. **111**, 012402 (2017).

[115] J.-C. Rojas-Sánchez, N. Reyren, P. Laczkowski, W. Savero, J.-P. Attané, C. Deranlot, M. Jamet, J.-M. George, L. Vila, and H. Jaffrès, Phys. Rev. Lett. **112**, 106602 (2014).

[116] Neil W. Ashcroft and N. David Mermin, Brooks Cole (1976).

[117] S. Datta, Cambridge University Press, 5th Ed. (1995).

[118] K. Kobayashi, Phys. Rev. B **84**, 205424 (2011).

[119] P. B. Ndiaye, C. A. Akosa, M. H. Fischer, A. Vaezi, E. A. Kim, and A. Manchon, Phys. Rev. B **96**, 014408 (2017).

[120] S. Ghosh and A. Manchon, Phys. Rev. B **97**, 134402 (2018).

[121] M. H. Fischer, A. Vaezi, A. Manchon, and E.-A. Kim, Phys. Rev. B **93**, 125303 (2016).

[122] F. Mahfouzi, B. K. Nikoli, and N. Kioussis, Phys. Rev. B **93**, 115419 (2016).

[123] M. S. Bahramy, P. D. C. King, A. De La Torre, J. Chang, M. Shi, L. Patthey, G. Balakrishnan, P. Hofmann, R. Arita, N. Nagaosa, and F. Baumberger, Nat. Commun. **3**, 1157 (2012).

[124] M. DC, R. Grassi, J.-Y. Chen, M. Jamali, D. R. Hickey, D. Zhang, Z. Zhao, H. Li, P. Quarterman, Y. Lv, M. Li, A. Manchon, K. A. Mkhoyan, T. Low, and J.-P. Wang, Nat.

Mater. **17**, 800 (2018).

[125] Y. Ando, T. Hamasaki, T. Kurokawa, K. Ichiba, F. Yang, M. Novak, S. Sasaki, K. Segawa, Y. Ando, and M. Shiraishi, Nano Lett. **14**, 6226 (2014).

[126] C. H. Li, O. M. J. Van 't Erve, J. T. Robinson, Y. Liu, L. Li, and B. T. Jonker, Nat. Nanotechnol. **9**, 218 (2014).

[127] A. Dankert, J. Geurs, M. Venkata Kamalakar, S. Charpentier, and S. P. Dash, Nano Lett **15**, 7976 (2015).

[128] S. Manipatruni, D. E. Nikonov, and I. A. Young, Nat. Phys. **14**, 338 (2018).

[129] S. Manipatruni, D. Nikonov, C. Lin, tanay A. Gosavi, H. Liu, B. Prasad, Y. Huang, E. Bonturim, R. Ramesh, and Ian A. Young, Nature **565**, 35 (2019).

[130] W. Richter and C. Becker, Phys. Status Solidi **84**, 619 (1977).

[131] J. Zhang, Z. Peng, A. Soni, Y. Zhao, Y. Xiong, B. Peng, J. Wang, M. S. Dresselhaus, and Q. Xiong, Nano Lett **11**, 2407 (2011).

[132] K. M. F. Shahil, M. Z. Hossain, V. Goyal, and A. A. Balandin, J. Appl. Phys. **111**, 054305 (2012).

[133] V. B. Nascimento, V. E. De Carvalho, R. Paniago, E. A. Soares, L. O. Ladeira, H. D. Pfannes, and P. Pfannes, J. of Elec. Spec. and Rel. Phen. **104**, 99–107 (1999).

[134] X. Yang, X. Wang, and Z. Zhang, J. Cryst. Growth **276**, 566 (2005).

[135] M. Jamali, A. Klemm, and J.-P. Wang, Appl. Phys. Lett **103**, 252409 (2013).

[136] K. Harii, T. An, Y. Kajiwara, K. Ando, H. Nakayama, T. Yoshino, and E. Saitoh, Cit. J. Appl. Phys. **109**, 116105 (2011).

[137] Y. Shiomi, K. T. Yamamoto, R. Nakanishi, T. Nakamura, S. Ichinokura, R. Akiyama, S.

Hasegawa, and E. Saitoh, Appl. Phys. Lett **113**, 052401 (2018).

[138] K. Kondou, H. Tsai, H. Isshiki, and Y. Otani, APL Mater. **6**, 101105 (2018).

[139] M. Isasa, M. Carmen Martínez-Velarte, E. Villamor, C. Magén, L. Morellón, J. M. De Teresa, M. R. Ibarra, G. Vignale, E. V Chulkov, E. E. Krasovskii, L. E. Hueso, and F. ` Elix Casanova, Phys. Rev. B **93**, 14420 (2016).

[140] M. Dc, T. Liu, J. Chen, T. Peterson, P. Sahu, and H. Li, To Be Publ. (n.d.).

[141] H. L. Wang, C. H. Du, Y. Pu, R. Adur, P. C. Hammel, and F. Y. Yang, Phys. Rev. Lett. **112**, 197201 (2014).

[142] R. R. Hull M Osgood, J. J. Parisi H Warlimont, and H. Julian Goldsmid, Springer Ser. Mater. Sci. (2016).

[143] D. Yue, W. Lin, J. Li, X. Jin, and C. L. Chien, Phys. Rev. Lett. **121**, 037201 (2018).

[144] O. Mosendz, J. E. Pearson, F. Y. Fradin, S. D. Bader, and A. Hoffmann, Appl. Phys. Lett **96**, 022502 (2010).

[145] O. Alves-Santos, E. F. Silva, M. Gamino, R. O. Cunha, J. B. S. Mendes, R. L. Rodríguez-Suárez, S. M. Rezende, and A. Azevedo, Phys. Rev. B **96**, 060408(R) (2017).

[146] S. Shi, A. Wang, Y. Wang, R. Ramaswamy, L. Shen, J. Moon, D. Zhu, J. Yu, S. Oh, Y. Feng, and H. Yang, Phys. Rev. B **97**, 041115(R) (2018).

[147] Y. T. Fanchiang, K. H. M. Chen, C. C. Tseng, C. C. Chen, C. K. Cheng, S. R. Yang, C. N. Wu, S. F. Lee, M. Hong, and J. Kwo, Nat. Commun. **9**, (2018).

[148] X. Tao, Q. Liu, B. Miao, R. Yu, Z. Feng, L. Sun, B. You, J. Du, K. Chen, S. Zhang, L. Zhang, Z. Yuan, D. Wu, and H. Ding, Sci. Adv. **4**, eaat1670 (2018).

[149] Y. Huo, F. L. Zeng, C. Zhou, and Y. Z. Wu, AIP Adv. **7**, 056024 (2017).

[150] C. Zucchetti, M.-T. Dau, F. Bottegoni, C. Vergnaud, T. Guillet, A. Marty, C. Beigné, S. Gambarelli, A. Picone, A. Calloni, G. Bussetti, A. Brambilla, L. Duò, F. Ciccacci, P. K. Das, J. Fujii, I. Vobornik, M. Finazzi, and M. Jamet, Phys. Rev. B **98**, 184418 (2018).

[151] K.-U. Demasius, T. Phung, W. Zhang, B. P. Hughes, S.-H. Yang, A. Kellock, W. Han, A. Pushp, and S. S. P. Parkin, 7 10644 (2016).

[152] A. Brataas, A. D. Kent, and H. Ohno, Nat. Mater. **11**, 372 (2012).

[153] S. Manipatruni, D. E. Nikonov, R. Ramesh, H. Li, and I. A. Young, ArXiv Prepr. 1512.05428 (2015).

[154] C. Hahn, G. De Loubens, O. Klein, M. Viret, V. V Naletov, and J. Ben Youssef, Phys. Rev. B **87**, 174417 (2013).

[155] S. Emori, A. Matyushov, H.-M. Jeon, C. J. Babroski, T. Nan, A. M. Belkessam, J. G. Jones, M. E. Mcconney, G. J. Brown, B. M. Howe, and N. X. Sun, Appl. Phys. Lett **112**, 182406 (2018).

[156] M. Haertinger, C. H. Back, J. Lotze, M. Weiler, S. Geprägs, H. Huebl, S. T. B. Goennenwein, and G. Woltersdorf, Phys. Rev. B **92**, 54437 (2015).

[157] H. Chang, P. A. P. Janantha, J. Ding, T. Liu, K. Cline, J. N. Gelfand, W. Li, M. C. Marconi, and M. Wu, Sci. Adv. **3**, e1601614 (2017).

[158] T. Liu, Y. Li, L. Gu, J. Ding, H. Chang, P. A. P. Janantha, B. Kalinikos, V. Novosad, A. Hoffmann, R. Wu, C. L. Chien, and M. Wu, Phys. Rev. Lett. **120**, 207206 (2018).

[159] M. Harder, Z. X. Cao, Y. S. Gui, X. L. Fan, and C.-M. Hu, Phys. Rev. B **84**, 054423 (2011).

[160] A. J. Berger, E. R. J. Edwards, H. T. Nembach, A. D. Karenowska, M. Weiler, and T. J.

Silva, Phys. Rev. B **97**, 094407 (2018).

[161] M. Caminale, A. Ghosh, † S Auffret, U. Ebels, K. Ollefs, F. Wilhelm, A. Rogalev, and W. E. Bailey, Phys. Rev. B **94**, 014414 (2016).

[162] Y. Sun, H. Chang, M. Kabatek, Y.-Y. Song, Z. Wang, M. Jantz, W. Schneider, M. Wu, E. Montoya, B. Kardasz, B. Heinrich, S. G. E. Te Velthuis, H. Schultheiss, and A. Hoffmann, Phys. Rev. Lett. **111**, 106601 (2013).

[163] R. Bansal, N. Chowdhury, and P. K. Muduli, Appl. Phys. Lett **112**, 262403 (2018).

[164] T. Tashiro, R. Takahashi, Y. Kajiwara, K. Ando, H. Nakayama, T. Yoshino, D. Kikuchi, and E. Saitoh, Proc Spie **8461**, 846106 (2012).

[165] A. Hoffmann, IEEE Trans. Magn. **49**, 5172 (2013).

[166] S. Fukami, C. Zhang, S. DuttaGupta, A. Kurenkov, and H. Ohno, Nat. Mater. **15**, 535 (2016).

[167] Q. Ma, Y. Li, D. B. Gopman, Y. P. Kabanov, R. D. Shull, and C. L. Chien, Phys. Rev. Lett. **120**, 117703 (2018).

[168] S. C. Baek, V. P. Amin, Y.-W. Oh, G. Go, S.-J. Lee, G.-H. Lee, K.-J. Kim, M. D. Stiles, B.-G. Park, and K.-J. Lee, Nat. Mater. **17**, 509 (2018).

Appendix: VITA

Publications

- **Mahendra DC et al.,** Room-temperature high spin–orbit torque due to quantum confinement in sputtered $Bi_xSe_{(1-x)}$ films *Nature Materials*, **17** 800-808 (2018).
- P. Quarterman, Congli Sun, Javier Garcia-Barriocanal, **Mahendra DC**, Yang Lv, Sasikanth Manipatruni, Dmitri E. Nikonov, Ian A. Young, Paul M. Voyles, and Jian-Ping Wang, Demonstration of Ru as the 4th ferromagnetic element at room temperature *Nature Communications*, **9**, 2058 (2018).
- Hickey, Danielle Reifsnyder, Ryan J. Wu, Joon Sue Lee, Javad G. Azadani, Roberto Grassi, **Mahendra DC**, Jian-Ping Wang, Tony Low, Nitin Samarth, and K. Andre Mkhoyan. Large-scale defects hidden inside a topological insulator grown onto a 2D substrate. *arXiv preprint:1808.03719* (2018).
- **Mahendra DC *et al.,*** Observation of high spin-to-charge conversion by sputtered bismuth selenide thin films at room temperature (Under Review in *Nano Letters*).
- Peterson, Thomas J., Protyush Sahu, Delin Zhang, **Mahendra DC**, and Jian-Ping Wang. Annealing temperature effects on spin Hall magnetoresistance in perpendicularly magnetized W/CoFeB Bilayers. *IEEE Transactions on Magnetics* (2018).
- **Mahendra DC *et al.,*** Room-temperature spin-to-charge conversion in sputtered bismuth selenide thin films via spin pumping from yttrium iron garnet (Under Review in *Applied Physics Letters*).
- Arnoud S. Everhardt*, **Mahendra DC***, Xiaoxi Huang, Shehrin Sayed, Tanay Gosavi, Yunlong Tang, Christoph Klewe, Chia-Cing Lin, Sasikanth Manipatruni,

Ian Young, Jian-Ping Wang, Ramamoorthy Ramesh, Rom-temperature spin-orbit torque in oxide spin-orbit coupled iridates (Under prep, * shared first author).

- Jun-Yang Chen, **Mahendra DC**, Delin Zhang, Zhengyang Zhao, Mo Li, and Jian-Ping Wang. Field-free spin-orbit torque switching of composite perpendicular CoFeB/Gd/CoFeB layers utilized for three-terminal magnetic tunnel junctions. *Applied Physics Letters,* **111**, 012402 (2017)**.**
- Mahdi Jamali, Zhengyang Zhao, **Mahendra DC**, Delin Zhang, Hongshi Li, Angeline Klemm Smith, and Jian-Ping Wang. Planar Hall effect based characterization of spin orbital torques in Ta/CoFeB/MgO structures. *Journal of Applied Physics*, **119**, 133902 (2016).
- Meghana Mankale, Zhaoxin Liang, Angeline Klemm Smith, **Mahendra DC**, Mahdi Jamali, Jian-Ping Wang, and Sachin Sapatnekar. A fast magnetoelectric device based on current-driven domain wall propagation. *Device Research Conference (DRC), IEEE 74th Annual* (2016).

Selected Presentations

- Invited: **Mahendra DC**, Roberto Grassi, Jun-Yang Chen , Mahdi Jamali, Danielle Reifsnyder Hickey, Delin Zhang, Zhengyang Zhao, Hongshi Li, P. Quarterman, Yang Lv, Mo Li, Aurelien Manchon, K. Andre Mkhoyan, Tony Low, and Jian-Ping Wang, "Discovery of quantum confinement effect in sputtered topological insultor films and observation of room-temperature high spin–orbit torque", in American Physical Society March Meeting 2019, March 4-8 at Boston, USA.
- Oral: **Mahendra DC et al., "**Observation of High Spin-to-charge Conversion by Sputtered $Bi_xSe_{(1-x)}$ Films at Room Temperature" in Joint MMM-Intermag, Janaury 14-18, 2019 at Washington, DC, USA.

- Oral and Poster: **Mahendra DC et al., "**Observation of High Spin-to-charge Conversion in Sputtered $Bi_xSe_{(1-x)}$ Films at Room Temperature"in TECHCON 2018, September 16-18 2018 at Austin, USA.
- Oral: **Mahendra DC et al.**, "Room-temperature Perpendicular Magnetization Switching through Giant Spin-orbit Torque from Sputtered $Bi_xSe_{(1-x)}$ Topological Insulator Material', in 62nd Annual Conference on Magnetism and Magnetic Materials, November 6-10, 2017 at Pittsburg, USA.
- Invited colloquium: **Mahendra DC**, "Giant Spin-Orbit Torque from Sputtered Bismuth Selenide Thin Films", November 2017 in WIU at Macomb, USA.
- Oral: **Mahendra DC et al**., "Room-temperature Perpendicular Magnetization Switching through Giant Spin-orbit Torque from Sputtered $Bi_xSe_{(1-x)}$ Topological Insulator Material', in Magnetic Frontiers: Topological Insulators, September 18-21 2017 at Nancy, France.
- Oral and Poster: **Mahendra DC et al.**, "Room-temperature Perpendicular Magnetization Switching through Giant Spin-orbit Torque from Sputtered $Bi_xSe_{(1-x)}$ Topological Insulator Material', in TECHCON 2017, September 10-12 2017 at Austin, USA.
- Oral: **Mahendra DC et al.**, "Giant spin Hall angle from topological insulator BixSe(1-x) thin films", in American Physical Society March Meeting 2017, March 13-17 at New Orleans, USA.
- Poster: **Mahendra DC et al.,** "Giant Spin Hall Angle From Bismuth Selenide And Heavy Metal Multilayers" in 61st Annual Conference on Magnetism and Magnetic Materials, October 31-November 4, 2016 at New Orleans, USA.
- Oral: Danielle Reifsnyder Hickey, Ryan Wu, Joon Sue Lee, **Mahendra DC**, Jianping Wang, Nitin Samarth, and Andre Mkhoyan. "Understanding the Atomic Structure of a Topological Insulator–2D Material Heterostructure." in American Physical Society March Meeting 2018, March 5-9 at Los Angeles, USA.

- Oral and Poster: Jun-Yang Chen, **Mahendra DC**, and Jian-Ping Wang, "Field-free spin orbit torque switching of perpendicular antiferromagnet/ferrimagnet structures for SOT-MRAM" in The 29th The Magnetic Recording Conference (TMRC 2018), August 8-10, 2018 at the Western Digital Milpitas Campus Milpitas, USA.
- Oral and Poster: Jian-Ping Wang, Jun-Yang Chen, **Mahendra DC**, Yang Lv, Zhengyang Zhao, Pro Sahu, "MRAM, CRAM and Magnetic Logic – New Physics and Materials" in The 29th The Magnetic Recording Conference (TMRC 2018), August 8-10, 2018 at the Western Digital Milpitas Campus Milpitas, USA.
- Oral: J. Y. Chen, **Mahendra DC**, D. L. Zhang, Z. Y. Zhao, M. Li and J. P. Wang. "Field-free spin-orbit torque switching of composite perpendicular CoFeB/Gd/CoFeB layers utilized for three-terminal magnetic tunnel junctions" 2017 IEEE International Electron Devices Meeting (IEDM), MRAM session, December 2017, San Francisco, USA.
- Oral and Poster: J. Y. Chen, **Mahendra DC**, D. L. Zhang, Z. Y. Zhao, M. Li and J. P. Wang. "Field-free spin-orbit torque switching of composite perpendicular CoFeB/Gd/CoFeB layers utilized for three-terminal magnetic tunnel junctions" in TECHCON 2017, September 10-12 2017 at Austin, USA.
- Invited: J. Wang, T. Low, **DC Mahendra**, R. Grassi, N. Samarth, Y. Lv, J. Chen, M. Jamali, J.C. Kally, D.R. Hickey, D. Zhang, Z. Zhao, H. Li, P. Quarterman, J. Lee, L. Mo, A. Manchon and A. Mkhoyan "Room Temperature Topological Insulator Spintronics: Demonstration of Perpendicular Magnetization Switching and Unidirectional Spin Hall Magnetoresistance" in 62nd Annual Conference on Magnetism and Magnetic Materials, November 6-10, 2017 at Pittsburg, USA